THE UNIVERSITY OF CHICAGO

ENERGY TRANSFER EVENTS IN PHOTOSYNTHESIS OBSERVED *IN VIVO* USING NONLINEAR ULTRAFAST SPECTROSCOPIES

A DISSERTATION SUBMITTED TO
THE FACULTY OF THE DIVISION OF THE PHYSICAL SCIENCES
AND
THE FACULTY OF THE DIVISION OF THE BIOLOGICAL SCIENCES
AND THE PRITZKER SCHOOL OF MEDICINE
IN CANDIDACY FOR THE DEGREE OF
DOCTOR OF PHILOSOPHY

GRADUATE PROGRAM IN BIOPHYSICAL SCIENCES

BY
PETER D. DAHLBERG

CHICAGO, ILLINOIS
DECEMBER 2016

To My Wife, Melissa Beth Dahlberg

If good things lasted forever, would we appreciate how precious they are?

-Bill Watterson, Calvin and Hobbes

Thanks to all of you who made my time at the University of Chicago incredible.

TABLE OF CONTENTS

LIST OF FIGURES

LIST OF TABLES

ACKNOWLEDGMENTS

My time at the university of Chicago was supported by the National Institute of Biomedical Imaging and Bioengineering in the NIH and by the National Science Foundation's Graduate Research Fellowship. The research presented in the thesis was funded by the Department of Energy and grants from Defense Advanced Research Projects Agency.

I would like to thank my collaborator Professor Neil Hunter for the mutant strains of *Rhodobacter sphaeroides* used in the thesis as well as scientific advice. I would like to thank the graduate student and post-doctoral mentors that I have had throughout my time: Andrew Fiddler for introducing me to nonlinear optics and trusting me to work on his experiment as a first year student; Justin Caram and Dugan Hayes for advice and guidance; Phil Long for teaching me how to culture *Rba. sphaeroides* and mentoring me in the graduate program in biophysical sciences; Sasha Kokhan for teaching me Labview and ns spectroscopy techniques; and Sarah Soltau for teaching me how to isolate light harvesting complexes. I would like to thank Adam Hammond, whose lab class gave me the freedom, inspiration, and knowledge to pursue biophysics research questions. I would like to thank all members of the Engel group, the Solar Energy Conversion Group, and the students and staff in the graduate program in the biophysical sciences for all the research you let me be apart of and all the fun we had doing it.

Lastly, I would like to thank my Advisors Greg Engel and Dave Tiede. Thank you both sincerely for giving me the opportunity to make mistakes. I made many throughout my graduate career due to the intellectual freedom you both gave me. Both of you were always there to give expert guidance when I was lost, but neither of you ever ordered me to try something your way. I imagine that the hardest part of great mentoring is knowing your answer, but letting someone else find theirs. Thank you both for everything.

ABSTRACT

Energy transfer in photosynthesis moves energy from where it is absorbed in the photosynthetic antenna to the site of charge separation (the reaction center). This energy transfer is rapid occurring on a picosecond timescale over a complex energetic landscape. The observation of the ultrafast path that absorbed energy takes through this landscape has been limited to isolated antenna and reaction center complexes, but much of the dynamics are lost studying systems in isolation. This thesis presents the first two-dimensional electronic spectroscopy measurements in living systems. These measurements were noninvasive and allowed for the study of ultrafast energy transfer dynamics in an unperturbed living system for the first time. These measurements necessitated improvements to the GRadient Assisted Photon Echo Spectrometer (GRAPES). The improvements made to the instrument decrease the acquisition time by two orders of magnitude while achieving an improved signal to noise ratio, expand the excitation bandwidth, and increased sampling allows for new processing techniques that eliminate scattered light in Fourier spaces. These pioneering measurements have provided new insight into photosynthetic energy transfer. These measurements have shown: that energy transfer within an antenna complex in artificial detergent and native membrane are the same within error; that quantum coherences persist in living systems with similar lifetimes to those measured in isolation; the improved signal to noise and bandwidth reveals higher lying excited states in Light Harvesting Complex 1 similar to the B850* state in Light Harvesting Complex 2; and energy transfer through the complex membrane environment from Light Harvesting complex 2 to Light Harvesting Complex 1 and into the Reaction Center; and this information to determine the functional photosynthetic unit *in vivo*. The ability to observe energy transfer pathways and membrane morphology in living photosynthetic cells in near real time opens new frontiers in photosynthesis. Future experiments are outlined that will move from the model organism of *Rba. sphaeroides* into cyanobacteria, algae, and plants to study the largely unknown molecular mechanisms and photoprotection.

CHAPTER 1

INTRODUCTION

1.1 Overview

Photosynthetic organisms contain some of the most amazing machinery in biology. The proteins responsible for photosynthesis are some of the most abundant on earth and have literally changed the planet, transforming the atmosphere to the oxygen rich composition we have today. [1] Photosynthetic organisms are the primary producers for almost all life on earth, powering us and our machines. Each year photosynthetic organisms harvest ≈100 TW of energy that is stored as biomass, significantly more than human consumption of 15 TW. [2]

Photosynthesis has been defined as *"a process in which light energy is captured and stored by an organism, and the stored energy is used to drive energy-requiring cellular processes"*. [1] The different steps involved in photosynthesis cover many orders of magnitude in time and space. A complete study of photosynthesis encompasses everything from the molecular motions that catalyze water splitting and oxygen evolution on the ms timescale [3] to the seasonal rhythms of a forest. This complexity and diversity of subject matter make the study of photosynthesis fascinating and nearly endless.

The work presented here seeks to understand one step in photosynthesis, the ultrafast energy transfer that occurs after the absorption of a photon. All photosynthetic organisms spatially separate the site of absorption from the site of charge separation and energy must migrate from where it is absorbed to where it can be used to generate free charges. [1, 4] This separation allows the specialization of the pigment-protein complexes (PPCs) responsible for each function. Absorption is accomplished in the PPCs known as the photosynthetic antenna. The antenna complexes are densely packed with chromophores that are strongly coupled to optimize their absorption cross-section and tune their absorption spectrum for different regions of the solar spectrum. Ultimately, energy absorbed in the antenna transfers

to a special pair of chlorophylls or bacteriochlorophylls, which are the site of charge separation and are held in a PPC known as the reaction center, RC. [5] Charge separation takes place on an ultrafast timescale [6, 7] and then a series of rapid electron transfer events separate the electron and hole by approximately 10 nm, preventing recombination. [1, 5] The potential energy of these separated charges drives the production of ATP in downstream biochemical processes.

The process of ultrafast energy transfer through the antenna network has been found to be 80-95% efficient under low light conditions. [1] In order for this process to be efficient, energy transfer and trapping in the RC must avoid spurious traps and compete with fluorescence and non-radiative relaxation processes that occur in several hundred picoseconds. [8] Most of the time however, the organism does not want to be efficient. Most photosynthetic organisms, such as the plants outside, saturate their light harvesting machinery just a few hours after sunrise. They spend the majority of the day dissipating excess excitations, which amount to about 90% of the light that is absorbed. This dissipation occurs via processes broadly labelled as photoprotection. Photoprotection is essential to the fitness of an organism because excited chlorophyll and bacteriochlorophyll can relax to form triplets that couple well with molecular oxygen to produce reactive oxygen species. [1] Many photoprotective processes alter the energy transfer pathways between the antenna and the reaction center. Photoprotective mechanisms can do this in several ways; the antenna itself can be restructured, thus changing its composition or its connectivity; chromophores that have different photophysics can be exchanged to alter the electronic structure; or existing chromophores or PPCs can undergo conformational changes that alter coupling between complexes. [9] All these various processes are part of a complex system of feedback loops that regulate light harvesting. Therefore it is not enough to observe a static picture of energy transfer in an organism. Rather, like most things in biology, the process of energy transfer is dynamic, **alive**, and is always changing to meet the demands of a fluctuating environment.

In order to observe the regulation of the ultrafast energy transfer process, measurements

need to be made in a living system. These measurements present numerous challenges, and as is often the case in biophysics, demand new instrumentation. Measurements must be made quickly to avoid the organism adapting to the laboratory conditions. They must be made at physiological temperature, have sub-picosecond temporal resolution, and cover a broad spectral range in order to observe all the various complexes and chromophores involved. Lastly, they must be made in the presence of intensely scattered light that accompanies measurements of whole cells and organisms.

For more than a century the only non-invasive measurement tool for energy transfer has been fluorescence spectroscopy, but fluorescence spectroscopy has numerous limitations. Fluorescence measurements are only directly sensitive to bright states i.e. those with allowed transitions to the ground state, and fluorescence is limited to picosecond temporal resolution. These limitations obscure many of the most interesting processes in energy transfer. For instance, in low-light conditions, when there are not photoprotective mechanisms activated, the reaction center quenches $\approx$ 80-95 % of absorbed sunlight allowing at most only 5-20 % of the light to decay via fluorescence. Conversely, during high-light, photoprotective mechanisms quench the majority of excitations and again fluorescence spectroscopy is observing only a small percentage of the absorbed light. The temporal resolution limitations associated with fluorescence spectroscopy also obscure many of the dynamical processes. Carotenoid-chlorophyll transfer, exciton relaxation, dynamics within a single antenna complex, quantum coherence, and conical intersections in carotenoids all occur on a sub picosecond timescale, most on a sub 100 fs timescale. Given these limitations it is remarkable what fluorescence has provided the photosynthetic community. This thesis is devoted to the development of an ultrafast spectroscopy technique, GRadient Assisted Photon Echo Spectroscopy (GRAPES), the first new non-invasive spectroscopy technique for measuring energy transfer since fluorescence spectroscopy. The capabilities of the new instrumentation are proven through pioneering ultrafast measurements made in a model organism, *Rhodobacter sphaeroides*.

1.2 *Rhodobacter sphaeroides* Antenna Complexes

Rba. sphaeroides is a model organism for the study of ultrafast energy transfer for two key reasons. First, *Rba. sphaeroides* is metabolically flexible. It can be grown heterotrophically i.e. from sugars or photoautotrophically. This metabolic flexibility allows for mutations to the photosynthetic machinery without the decreased fitness of the organism. [10] Second, *Rba. sphaeroides* has spectrally distinct antenna complexes that make it easier to follow the flow of energy through the network. Decades of work have led to in-depth knowledge of its photosynthetic machinery. [4]

Rba. sphaeroides has two different types of antenna complexes, Light Harvesting complex II (LH2) and Light Harvesting complex I (LH1). LH2 is a peripheral antenna complex, meaning that it does not transfer energy into the RC; rather, it transfers absorbed energy into LH1. LH1 is a core complex that surrounds the RC. The absorption spectrum of LH2, and LH1 along with their crystal structures can be seen in Figure 1.1. [11, 12] LH2 has two separate rings of bacteriochlorophyll *a* (Bchl *a*) that absorb predominately at 800 nm and 850 nm leading to their names, the B800 and B850 bands. LH1 has a single band of Bchl *a* that absorbs strongly at 875 nm and is known as the B875 band. The absorption features arising from the chromophores in the RC are not visible underneath the significant absorption from the antenna, but the special pair of bacteriochlorophyll A absorbs at 870 nm.

The crystal structures in Figure 1.1 are essential in our understanding of the electronic structure of LH2 and LH1. LH2 has C_9 symmetry and is composed of alternating α- and β-polypeptides that act as a scaffold for the Bchl *a* in B800 and B850. The B850 band in LH2 is composed of 18 strongly coupled Bchl *a*, $\approx$300 cm^{-1}, resulting in their red-shifted absorption to 850 nm in contrast to the 9 weakly coupled, $\approx$20 cm^{-1}, B800 Bchl *a* that absorb at 800 nm. [13] The B800 and B850 rings are weakly coupled to each other, $\approx$20-50 cm^{-1}. [13, 14] LH1 is also composed of repeating α- and β- polypeptides that hold the Bchl *a* of the B875 band rigidly in place. The Bchl*a* in the B875 band share many characteristics with the B850

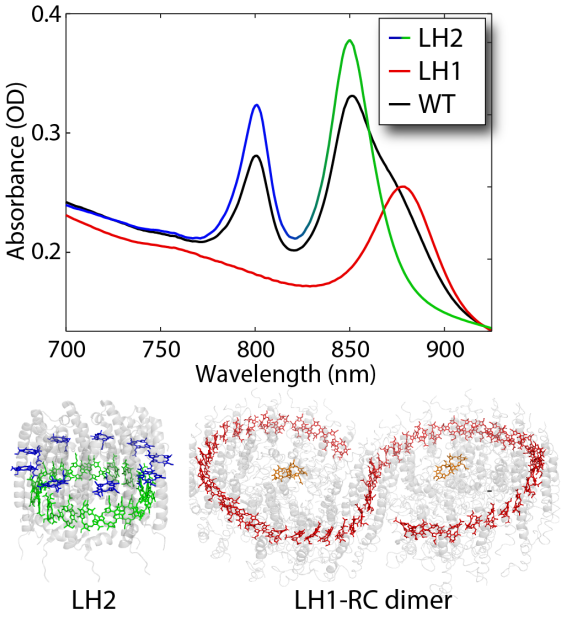

Figure 1.1: Absorption spectra taken in a 200 μm quartz cuvette of LH2-only cells, LH1-only cells, and wild type (WT) cells. The large offset from zero optical density is due to the significant amount of scatter present. The colors of the lines in the LH2-only and LH1-only absorption spectra correspond to the different bands of chromophores shown in the crystal structures below. LH2 contains two bands of chromophores, the B800 and the B850 shown in blue and green respectively. Energy transfer from LH2's B850 band to LH1's B875 band of chromophores shown in red that transfers energy to the special pair of the RC shown in orange.

ring of BChl *a* in LH2. The RC-LH1 complex exists in *Rba. sphaeroides* as both a monomer and a dimer, but the dimer is the dominant structure *in vivo*. Each monomer in the dimer contains 28 BChl *a*. The electronic coupling between BChl *a* in LH1 is well approximated by dipolar coupling except in the case of nearest neighbors where the Mg-Mg distance is on the order of 1 nm. [11] As in B850, the coupling strength of nearest neighbors is estimated to be a $\approx$300 cm^{-1}. [15, 16] The strong coupling in B850 and B875 leads to the delocalization of excitations across BChl *a* and the existence of higher-lying excited states. In B850 this strong coupling leads to the well established higher energy B850* states that absorb weakly at 770-815 nm. Similar electronic states in LH1 are explored in more detail in Chapter 6.

Much of what is known about energy transfer through *Rba. sphaeroides'* network of antenna complexes is determined by ultrafast spectroscopy studies performed on isolated complexes or membrane fragments [4, 17–20] along with AFM images of photosynthetic membranes [21, 22] and crystal structures of the various antenna complexes. [23] This data has allowed for detailed modeling and an estimation of what energy transfer pathways might exist in a living organism. [24] These data and models show that energy transfer through

the antenna is largely downhill. Energy transfers from B800 to B850 on a 0.7 ps time scale and between B850s on a few picosecond timescale. Similarly, energy transfers from B850 to B875 also occurs on a few picosecond timescale and into the RC on a tens of ps timescale. This final step of transfer from LH1 to the RC is slightly uphill in energy and is believed to be the rate limiting step in energy transfer. At this point it is worth reviewing the different mechanisms of energy transfer to understand the process more completely.

1.3 Mechanisms of Energy Transfer In Photosynthesis

Energy transfer between electronic excited states in photosynthetic antenna can be classified as three different types based on the strength of the coupling between the chromophores. [25] When the energy of the coupling between chromophores is much less than the reorganization energy, the transfer can be well approximated as incoherent hopping between localized states mediated by dipolar coupling. This method of energy transfer is described by Förster Resonance Energy Tranfser or FRET. When the coupling between chromophores is greater than the reorganization energy the excitations can no longer be treated as localized and instead energy transfer is viewed more as a relaxation process between delocalized states that is mediated by coupling to an external bath. This type of energy transfer is described by Redfield theory. Lastly, there is an intermediate coupling regime, in which photosynthetic organisms often function. In this regime coherent evolution of the system needs to be taken into consideration and the system can be treated as a quantum mechanical wavepacket. While the phase of this wavepacket is maintained quantum interference effects can influence the relaxation dynamics. The following sections go into more detail on energy transfer in these three regimes.

1.3.1 Förster Resonance Energy Transfer

* The lifetimes of energy transfer from some donor state to some acceptor state in Förster theory given by Equation 1.1,

$$k_e = k_f \left(\frac{R_0}{R} \right)^6 \tag{1.1}$$

k_e is the first-order rate constant for energy transfer from the donor to the acceptor. k_f is the fluorescence rate of the donor, R is the distance between the donor and acceptor and R_0 is the distance at which the transfer efficiency if 50%. The value of R_0 varies from system to system and is calculated in units of Ångstroms following Equation 1.2

$$R_0^6 = 8.79 \times 10^{-5} J \kappa^2 n^{-4} \tag{1.2}$$

n is the refractive index, and J is the overlap of the donor's fluorescence spectrum with the acceptor's absorption spectrum as can be seen in Figure 1.2. J often leads to the confusion that Förster resonance energy transfer is mediated by a photon being emitted by the donor and absorbed by the acceptor. This is not the case though, as Förster resonance energy transfer is a nonradiative process. The simplest way to show this experimentally is to show that when Förster resonance energy transfer is the dominant decay pathway for a donor state, the lifetime of the donor state is dramatically shortened. This would not be the case if the donor were simply fluorescing. Lastly, κ^2 is an orientational factor defined in Equation 1.3

$$\kappa^2 = (cos(\alpha) - 3cos(\beta_1)cos(\beta_2))^2 \tag{1.3}$$

where α is the angle between the two transition dipoles and the βs are the angle between the dipoles and the vector joining the donor and acceptor. Often one assumes a random orientation of the dipoles, in which case κ takes on a value of 2/3. This is often a coarse

∗. Material from this section relies heavily on the discussion from [1].

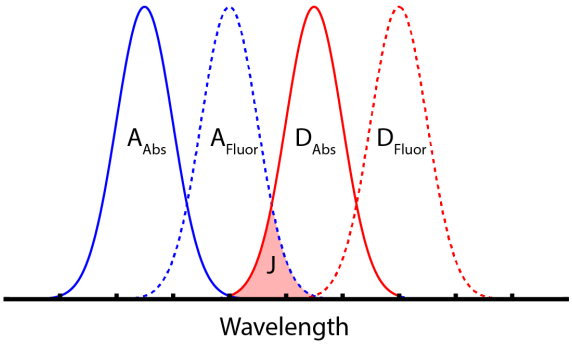

Figure 1.2: Diagram of the overlap integral that defines J in Equation 1.2 As the overlap between the donor's fluorescence spectrum and the acceptor's absorption spectrum is increased the coupling between them increases resulting in more efficient energy transfer.

approximation that can be misleading.

Much of the energy transfer processes in photosynthesis are well described by Förster theory. For instance, in *Rba. sphaeroides*, energy transfer from B800 to B850 in LH2, energy transfer between LH2 and LH1, energy transfer between LH2s and between LH1s as well as energy transfer from LH1 into the RC, are all well described by Förster theory. In all of these cases the coupling is weak, tens of wavenumbers, compared to the reorganization energy.

1.3.2 Redfield Theory

†While Förster theory describes energy transfer between complexes and between bands of chromophores within complexes, it is not applicable to the relaxation processes within strongly coupled bands of chromophores, such as B850 and B875 in LH2 and LH1. For a description of these systems we need to turn to Redfield theory and the concept of an exciton.

†. Material from this section relies heavily on the discussion from [26].

Redfield theory operates in a regime where the coupling energy between chromophores is large, greater than the reorganization energy. In this regime, the first step in understanding energy transfer is to understand what the donor and acceptor states actually are. This is not at all intuitive. When the coupling between chromophores is large, it is no longer appropriate to think of excitations as localized and one must stop thinking in the "site basis" and begin thinking in the "exciton basis".

To move from the intuitive, site basis, where excitations are localized to individual chromophores, to the exciton basis one begins with the Hamiltonian in the site basis.

$$H = \begin{bmatrix} E_{11} & v_{12} & v_{13} & \dots & v_{1n} \\ v_{21} & E_{22} & v_{23} & \dots & v_{2n} \\ \vdots & \vdots & \vdots & \ddots & \vdots \\ v_{n1} & v_{n2} & v_{n3} & \dots & E_{nn} \end{bmatrix} \tag{1.4}$$

Here E_{ii} is the site energy of the ith chromophore and v_{ij} is the coupling between chromophore i and j. These coupling terms are a large part of why the crystal structures of these complexes are so crucial to our understanding of their electronic structure. The coupling terms v_{ij} are often determined from dipolar or multipolar coupling; in order to do this, knowing the structure is essential. As we saw above in Equation 1.1, 1.2, and 1.3, the orientation and distance between chromophores is essential to understanding their coupling. Diagonalization of the Hamiltonian in the site basis produces the excitonic states and their energies, where the energies are the Eigenvalues and the delocalized states are described by the Eigenvectors.

All of the electronic coupling necessary for energy transfer has been encompassed in Equation 1.4 and indeed, if the Hamiltonian encompassed everything, the excitations would be stuck in their eigenstates forever and never transfer, relax, or even decohere (a concept that will be covered in the next section). Thus energy transfer in Redfield theory must be driven by something besides electronic coupling. The clues to what drives energy transfer in

Redfield theory come up as soon as one thinks about transfering from a high energy state to a low energy state. Energy must be conserved and the way to conserve energy is to let some dissipate into the bath as phonons. This system-bath coupling is at the center of Redfield theory. It is not described in 1.4 and so the Hamiltonian there can be thought of as only the Hamiltonian of the system and the true time evolution needs to encompass the bath as well.

The coupling between the system and bath depends on the available vibrational modes of the bath, called the spectral density $J(\omega)$ (different from the overlap J in Equation 1.2 above) and the strength with which the system couples to those modes is given by the Huang-Rhys factor, S. The spectral density is often normalized to the Huang-Rhys factor in the following way

$$S = \int_0^\infty J(\omega) d\omega \tag{1.5}$$

The spectral density then directly gives the Fourier-transformed correlation function, $C^{\tilde{Re}}(\omega)$

$$C^{\tilde{Re}}(\omega) = \pi\omega^2[(1 + n(\omega))J(\omega) + n(\omega)J(\omega)] \tag{1.6}$$

for chromophores n and m. The rate constants for energy transfer between excitons M and K are given by

$$k_{MK} = 2\gamma_{MK} C^{\tilde{Re}}(\omega_{MK}) \tag{1.7}$$

Where γ_{MK} describes the spatial overlap of excitons M and K given by

$$\gamma_{MK} = \sum_{n,m} c_m^{(M)} c_m^{(K)} c_n^{(M)} c_n^{(K)} e^{-R_{mn}/R_c} \tag{1.8}$$

where $c_i^{(M)}$ is the contribution from the ith chromophore to the M exciton, R_{ij} is the distance between the i and j chromophores, and R_c is the distance over which the chromophores

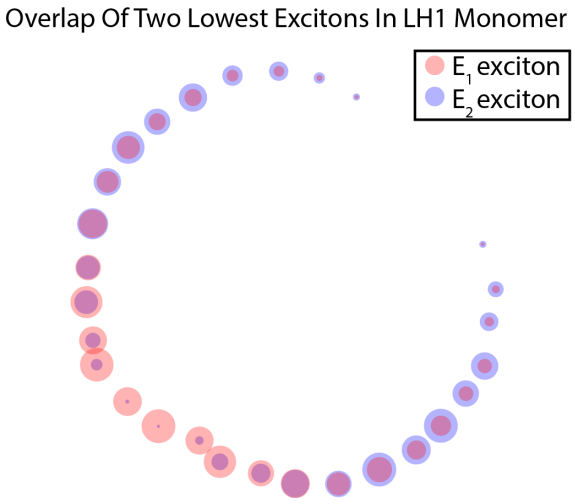

Figure 1.3: The two lowest energy exciton states represented in the site basis. The contribution from each chromophore to the two excitons is indicated by the size of the circle. The significant spatial overlap between these states and their coupling to the bath leads to energy transfer between the two excitons.

are assumed to share the same bath, usually on the order of a few Ångstroms. The overlap of the the excitons in the site basis and their coupling to the bath drives energy transfer in Redfield theory. A demonstration of this can be seen in Figure 1.3 which shows the overlap of the two lowest exciton states in LH1. More details on the excitonic structure of LH1 can be found in Chapter 6 and the digital supplement provides matlab code for performing these operations.

1.3.3 Quantum Coherence

Both descriptions of energy transfer above have neglected some quantum mechanical aspects of the excitations. The excitations are actually wave functions that are not at all classical objects. This can have interesting consequences for energy transfer. [27] In analogy to the double slit experiment where even single photons passed through the slits produces an interferogram, single excitations in photosynthesis can sample multiple relaxation pathways and produce constructive and destructive interference which impact the ultimate trajectory taken by the excitation. The duration of time the excitation spends sampling multiple pathways

simultaneously depends on how long the wave functions maintains its quantum mechanical phase, which is what leads to the interference. During this time the excitation is not in a well defined state; in fact, in the lens of quantum mechanics the question is ill defined. Instead, the excitation possesses a probability amplitude of being in any one of many different states and is in a "superposition" of states. The probability amplitude squared gives the probability of the excitation being in a certain state and the wavefunction only collapses onto one state after measurement, which can come from the experiment or the excitation interacting with the bath. The fact that we can only say probabilistically what state the excitation is in does not reflect a lack of information; rather, it is fundamental to the excitation itself.

In our spectroscopy, which is detailed in Section 1.4 and Chapter 2, the lifetime of these superposition states can be observed as oscillations in a time domain signal, known as a quantum coherence. [18] The oscillations occur at a frequency related to the energy gap between the two states. There is much speculation about the nature of these coherences. For instance, the superposition state could be between an electronic state with and without a vibrational quantum of energy. This type of coherence is a vibrational coherence and is not likely to impact photosynthetic energy transfer efficiencies. Another type of coherence is between two different electronic excited states. This type of coherence, called an electronic coherence, would be likely to impact energy transfer efficiency because it would allow the excitation to sample multiple energy transfer pathways and avoid trap states. Lastly, there are coherences that are a mixture of electronic and vibrational coherences. All coherences are vibronic to some extent and research is ongoing to quantify the amount of vibrational and electronic character in these coherences. [28] There is a large debate surrounding the biological significance of these coherences that has been in the field since the first measurements of these coherences by Engel et al. in 2007. [18] Chapter 5 presents the first measurements of these coherences in living systems showing that their presence is not an artifact of measuring systems in isolation.

1.4 Theory Of Nonlinear Spectroscopy

To observe energy transfer in photosynthesis we turn to time resolved optical spectroscopies. The text that follows is a brief summary of the essential theoretical aspects of optical spectroscopy needed to understand the experiments discussed in the thesis. Details can be found in references [29, 30].

1.4.1 Light-Matter Interactions

We begin the discussion of optical spectroscopy with a discussion of how light and matter interact. Classically, light is an oscillating electromagnetic wave. This oscillating wave interacts with the electrons of a molecule or atom. Typically the wavelength of light used is significantly larger than the molecule and therefore the electronic configuration of the molecule interacts in the far field approximation only via its dipolar term in a multipole expansion of its charge distribution. Mathematically this interaction, $\hat{W}(t)$ is summarized as

$$\hat{W}(t) = -\hat{\mu}E(t) \tag{1.9}$$

Here, $E(t)$ is the electric field, and $\hat{\mu}$ is the molecular dipole. We can include this interaction into our system Hamiltonian, H_{sys}, described in Equation 1.4 so that our new Hamiltonian becomes

$$H = H_{sys} + \hat{W}(t) \tag{1.10}$$

The time evolution of the states is given by the time-dependent Schrödinger Equation

$$i\hbar\frac{\partial}{\partial t}|\psi\rangle = \hat{H}|\psi\rangle \tag{1.11}$$

the wave function, $|\psi\rangle$ is expressed as a linear composition of the eigenstates of the system

Hamiltonian

$$|\psi\rangle = \sum_n c_n e^{-iE_n t/\hbar}|n\rangle \tag{1.12}$$

and the time evolution can be written by the substitution of Equation 1.12 into 1.11 giving

$$\frac{\partial}{\partial t}c_{m(t)} = -\frac{i}{\hbar}\sum_n c_n(t)e^{-i(E_n-E_m)t/\hbar}\langle m|\hat{W}(t)|n\rangle \tag{1.13}$$

Substituting Equation 1.9 above we see the time evolution depends on the electric field and the transition dipole between states $|m\rangle$ and $|n\rangle$, called μ_{mn}

$$\frac{\partial}{\partial t}c_{m(t)} = -\frac{i}{\hbar}\sum_n c_n(t)e^{-i(E_n-E_m)t/\hbar}\langle m|\hat{\mu}(t)|n\rangle E(t) \tag{1.14}$$

Equation 1.14 describes a large set of coupled differential equations that describes the time evolution of the superposition states after interaction with an electric field. This works well if we only have two states. Equation 1.14 for a two state system simply becomes

$$\frac{\partial}{\partial t}c_{1(t)} = +\frac{i}{\hbar}c_0(t)e^{-i(E_0-E_1)t/\hbar}\langle 1|\hat{\mu}(t)|0\rangle E(t) \tag{1.15}$$

$$\frac{\partial}{\partial t}c_{0(t)} = +\frac{i}{\hbar}c_1(t)e^{-i(E_1-E_0)t/\hbar}\langle 0|\hat{\mu}(t)|1\rangle E(t) \tag{1.16}$$

If we let $|0\rangle$ be the ground state and we assume we interact with an ultrafast pulse i.e. $E(t)$ is zero for $t > 0$ then we have

$$|\psi(t)\rangle = c_0 e^{-iE_0 t/\hbar}|0\rangle + ic_1 e^{-iE_1 t/\hbar}|1\rangle \tag{1.17}$$

We find that after the interaction with the laser pulse the system is put into a superposition state of $|0\rangle$, where it started, and $|1\rangle$. The second term in Equation 1.17 shows that

the probability amplitude of being in state $|0\rangle$ or $|1\rangle$ has a complex phase associated with it that is defined by the interaction with the laser pulse. In an ensemble measurement, like the ones defined later in Chapter 2, if all the molecules in the ensemble have the same phase and time evolution, the laser has created a macroscopic polarization, $P^{(1)}(t)$ that evolves with the same time dependence as in Equation 1.17. This oscillating macroscopic polarization describes the motion of the charges due to the light matter interaction. By Maxwell's Equations, the oscillating charges that $P(t)$ describes emit an oscillating electric field that we can detect. The strength of that field is just the expectation value of the transition dipole

$$P(t) = \langle \mu \rangle \tag{1.18}$$

$$= \langle \psi(t) | \hat{\mu} | \psi(t) \rangle \tag{1.19}$$

$$= (c_0 e^{iE_0 t/\hbar} \langle 0| - ic_1 e^{iE_1 t/\hbar} \langle 1|) \hat{\mu} (c_0 e^{-iE_0 t/\hbar} |0\rangle + ic_1 e^{-iE_1 t/\hbar} |1\rangle) \tag{1.20}$$

$$= c_0 c_1 \langle 0|\hat{\mu}|1\rangle sin((E_1 - E_0)t/\hbar) + c_0^2 \langle 0|\hat{\mu}|0\rangle + c_1^2 \langle 1|\hat{\mu}|1\rangle \tag{1.21}$$

The last two terms in Equation 1.25 are the permanent dipoles and have no time dependence and therefore do not contribute to the emitted signal field. The first term does have a time dependence that is related to the transition dipole between the two states. This results in a situation described in Figure 1.4. Classically, the oscillating charges emit the signal field; quantum mechanically it is the superposition that creates a macroscopic polarization.

1.4.2 Density Matrix Formalism

The section above outlines the theoretical formalism for a single light matter interaction and explicitly details the first order polarization induced in a two state system. When a real multilevel system is considered, the coupled system of Equations in 1.16 becomes unmanageable and this leads to the density matrix formalism. The density matrix describes a statistical mixture of wavefunctions and is defined as the sum over the outer product of

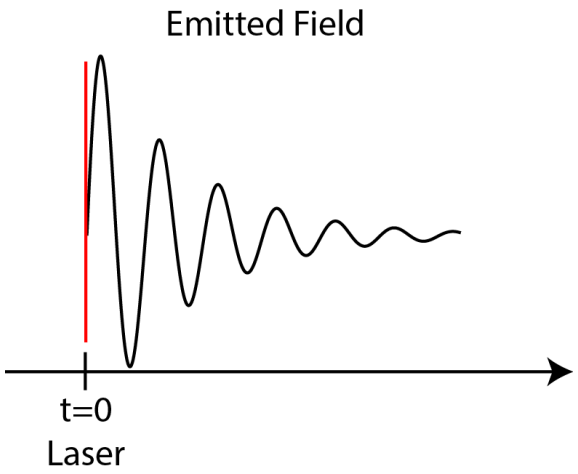

Figure 1.4: Diagram of a single light-matter interaction that occurs at t=0. This interaction induces an oscillating macroscopic polarization that emits an electric field field that decays as interactions with the bath cause the macroscopic polarization to dephase.

the wavefunctions,

$$\rho = \sum_k p_k |\psi_k(t)\rangle\langle\psi_k(t)|, \tag{1.22}$$

where p_k is the statistical weight of finding a system in the ensemble in the quantum state with wavefunction $|\psi_k\rangle$. If we choose to expand $|\psi_k\rangle$ in the exciton basis of Equation 1.14 we can write the density matrix as a matrix

$$\rho = \begin{bmatrix} \rho_{00} & \rho_{01} & \rho_{02} & \cdots & \rho_{0n} \\ \rho_{10} & \rho_{11} & \rho_{12} & \cdots & \rho_{1n} \\ \vdots & \vdots & \vdots & \ddots & \vdots \\ \rho_{n0} & \rho_{n1} & \rho_{n2} & \cdots & \rho_{nn} \end{bmatrix} \tag{1.23}$$

The diagonal elements ρ_{nn} give the probability amplitude of finding a state within the ensemble with energy E_n and the off diagonal elements ρ_{nm} indicate a superposition between states with energies E_n and E_m. The time evolution of the density matrix follows from the time-dependent Schrödinger Equation and is known as the Liouville-von Neumann Equation

$$\frac{\partial}{\partial t} = \frac{-i}{\hbar}[H, \rho] \tag{1.24}$$

The expectation value of an observable, for instance the expectation of the dipole operator in Equation 1.19, can also be calculated from the density matrix

$$P(t) = \langle \hat{\mu} \rangle = \sum_k p_k \langle \psi_k(t) | \hat{\mu} | \psi_k(t) \rangle = Tr[\hat{\mu}\rho(t)] \tag{1.25}$$

Thus, the density matrix formalism is a powerful way to describe an ensemble of quantum systems, both their time evolution and the macroscopic observables that they would generate. This formalism is applied to nonlinear spectroscopy in the next section.

1.4.3 Third-Order Polarization Spectroscopy

As shown in Equation 1.25, the macroscopic polarization induced by a light matter interaction on an ensemble of quantum states can be described as a trace over the dipole operator acting on the density matrix. The applied electric field used in spectroscopy can often be considered a weak perturbative field. This becomes clear when we compare typical values for applied fields to the electric fields generated by the electron and proton in a hydrogen atom. The electric field in a hydrogen atom is $E_{hydrogen} = \frac{e}{4\pi\epsilon_0}\frac{1}{a_0^2} \approx 5 \times 10^{11}$ V/m and the electric field produced using a typical excitation power of 20 μJ/cm^2 is $E_{exp} \approx 2 \times 10^6$ V/m, or about 5 orders of magnitude weaker than the intrinsic electric field. The amplitude of the applied field motivates a perturbative expansion approach. We can expand $P(t)$ in order of the number of light matter interactions

$$P(t) = \langle \hat{\mu} \rangle = \langle \hat{\mu}\rho^{(0)}(t) \rangle + \langle \hat{\mu}\rho^{(1)}(t) \rangle + \langle \hat{\mu}\rho^{(2)}(t) \rangle + \langle \hat{\mu}\rho^{(3)}(t) \rangle + ... \tag{1.26}$$

The first term corresponds to the permanent dipoles. The second term we have encountered in Section 1.4.1 and describes dispersion and absorption events. The third term represents

three interactions with the dipole operator and in all isotropic (randomly oriented) samples this term vanishes. The fourth term describes four interactions with the dipole operator and is the primary term measured in the nonlinear spectroscopies in this thesis. The four light matter interactions come from three externally applied fields that come in the form of laser pulses and one comes from the field being emitted by the sample. The three interactions with the applied fields perturb the system based on its third-order polarization and material response function. The third order polarization is

$$P^{(3)}(t) = \int_0^\infty dt_3 \int_0^\infty dt_2 \int_0^\infty dt_1 R^{(3)}(t_3, t_2, t_1) E(t - t_3) E(t - t_3 - t_2) E(t - t_3 - t_2 - t_1) \tag{1.27}$$

Here, t_1, t_2, and t_3 represent the time of the interactions with the electric field and $R^{(3)}$ is the material response function, which can be related back to the density matrix and the dipole operator in the following way,

$$R^{(3)}(t) = (\frac{i}{h})^3 \theta(t_1)\theta(t_2)\theta(t_3)\langle[[[\hat{\mu}(t_3 + t_2 + t_1), \hat{\mu}(t_2 + t_1)], \hat{\mu}(t_1)]\hat{\mu}(0)]\rho_{00}\rangle, \tag{1.28}$$

where the θs are Heaviside functions that ensure causality, i.e. that interactions with the field cannot occur before the field is present. Expansion of the response function's commutators show the four interactions with the dipole operator. These interactions can occur with the dipole operator as either bra or ket vectors and are known as the Liouville space pathways. Keeping track of the different interactions in this manner is quite cumbersome, instead, a more graphical representation of these pathways is presented in Figure 1.5 as a double sided Feynman diagram.

In Figure 1.5 interactions with light are indicated by the red arrows and time moves forward vertically from the bottom of the diagram. These interactions produce transitions in the density matrix that evolve with time. The first three interactions are with the external

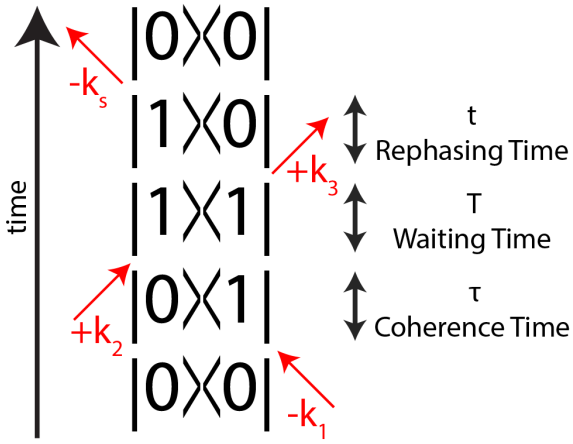

Figure 1.5: Feynman diagram used to understand the different interaction pathways taken during a third order polarization experiment. The red arrows represent interactions with an excitation field. These interactions produce transitions in the density matrix that evolve phase and undergo dynamics.

applied fields. The timing for these interactions are experimentally controlled in various ways, see Chapter 2 for more details. The last interaction is generated from the oscillating macroscopic polarization induced in the sample emitting a signal field, similar to the one described in Section 1.4.1. There are several rules for the interactions that can be written with a Feynman diagram. First, interactions that are drawn in towards the diagram represent absorption events and serve to increase the energy of the bra or ket from its previous state. Conversely arrows that are drawn away from the diagram correspond to emission events and decrease the energy of the bra or ket. Second, arrows pointing to the right by convention are associated with a positive wave vector while arrows to the left have a negative wave vector. Third, the final state must be a population state and result from an outgoing arrow. In an experiment all Feynman diagrams that follow these rules will contribute to the emitted signal. For a three level system there are only six possible pathways and their mirror images shown in Figure 1.6. The signals are broken up into the six different types. Rephasing versus non-rephasing signals can be thought of in terms of their phase evolution. For a rephasing signal, the phase evolution that occurs after the third interaction is in the opposite direction as the phase evolution induced by the first interaction. For a nonrephasing signal the phase evolution is in the same direction. Stimulated emission and ground state bleach pathways give rise to signal fields that are in phase with the final excitation field and will add constructively giving them a positive sign by convention. Excited state absorption

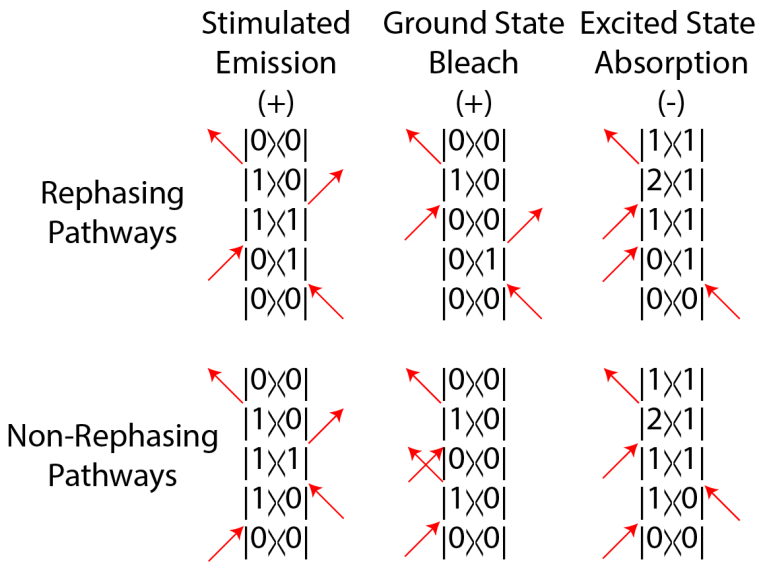

Figure 1.6: Feynman diagram used to understand the different interaction pathways taken during a third order polarization experiment. The red arrows represent interactions with an excitation field. These interactions produce transitions in the density matrix that evolve phase and undergo dynamics.

will have an emitted signal that is 180 degrees out of phase with the final excitation field and will destructively interfere giving it a negative sign.

In addition to these straightforward pathways, internal dynamics can also happen. Consider the excited state absorption pathway in Figure 1.7. The Figure on the left is the excited state absorption pathway drawn in Figure 1.6. The figure on the right has all the same interactions but during the waiting time the system has relaxed to the ground state. We can use the third-order spectroscopies to monitor the excited state lifetime through a decay in the magnitude of the negative signal resulting from excited state absorption. It is important to keep in mind that all possible pathways will contribute to the emitted signal, though the signals are emitted in several unique directions defined by the addition of the wave vectors of the interacting fields. Typically, the signal is only detected in one direction during the experiment and this is known as the phase-matched direction. There are still numerous Liouville pathways contributing in any given phase-matched direction and the contribution from all pathways must be considered. For instance, the decay of excited state absorption and ground state bleach are intricately linked. As the excited state absorption

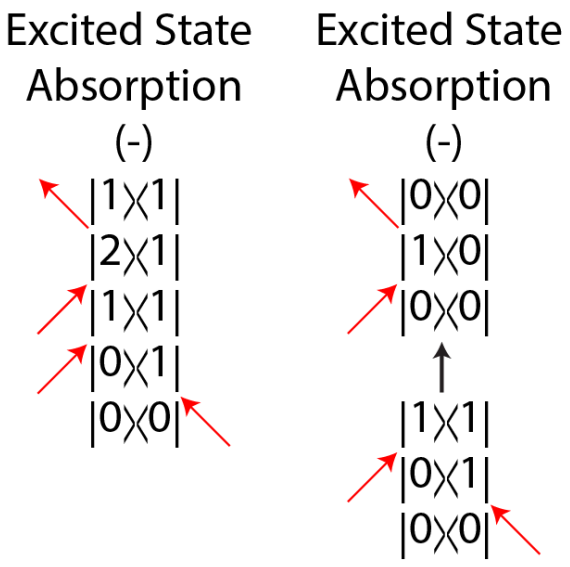

Figure 1.7: Two excited state absorption pathways. The pathway on the left contains no waiting time dynamics while the pathway on the right indicates energy transfer to the ground state during the waiting time through the vertical arrow.

pathway on the left of Figure 1.7 decays to be the pathway on the right, this emitted field overlaps spectrally with the ground state bleach signal in Figure 1.6. Thus the true decay of the excited state absorption feature is actually a shift in its spectrum that causes it to overlap with an equally strong positive signal from ground state bleach thus resulting in a decay of both a positive and negative feature that allows us to monitor the lifetime of the excited state and its electronic structure.

In addition to the population dynamics in the waiting time, one can also observe coherent dynamics like those discussed in Section 1.3.3 when the system is in a superposition state during the waiting time, see Figure 1.8. The superposition is observable in the waiting time domain as oscillations in the signal amplitude at certain spectral locations. The states 1 and 1' could be an electronic state and an electronic state plus vibrational quanta of energy, or they could be two electronic excited states or a mixture of vibrational and electronic states. The frequency of the oscillation in any case will be given by the energy difference between the two states.

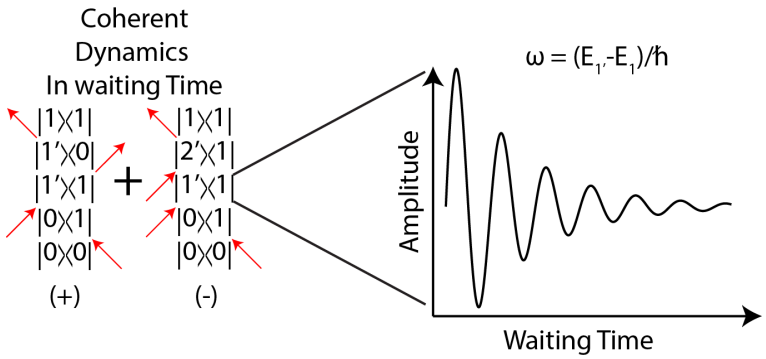

Figure 1.8: Oscillation in waiting time domain arising from superposition of states 1 and 1'. The damping of the sine wave is due to interactions with the bath causing a dephasing of the superposition state.

REFERENCES

[1] R. E. Blankenship. *Molecular mechanisms of photosynthesis*. Blackwell Science, Malden, Massachusetts, 2002.

[2] R. E. Blankenship, D. M. Tiede, J. Barber, G. W. Brudvig, G. Fleming, M. Ghirardi, M. R. Gunner, W. Junge, D. M. Kramer, A. Melis, T. A. Moore, C. C. Moser, D. G. Nocera, A. J. Nozik, D. R. Ort, W. W. Parson, R. C. Prince, and R. T. Sayre. Comparing photosynthetic and photovoltaic efficiencies and recognizing the potential for improvement. *Science*, 332(6031):805–809, 2011.

[3] C. W. Cady, R. H. Crabtree, and G. W. Brudvig. Functional models for the oxygen-evolving complex of photosystem ii. *Coordination Chemistry Reviews*, 252(3-4):444–455, 2008.

[4] H. van Amerongen, L. Valkunas, and R. van Grondelle. *Photosynthetic excitons*. World Scientific, River Edge, N.J., 2000.

[5] J. Deisenhofer and J. R. Norris. *The Photosynthetic reaction center*. Academic Press, San Diego, California, 1993.

[6] F. D. Fuller, J. Pan, A. Gelzinis, V. Butkus, S. S. Senlik, D. E. Wilcox, C. F. Yocum, L. Valkunas, D. Abramavicius, and J. P. Ogilvie. Vibronic coherence in oxygenic photosynthesis. *Nature Chemistry*, 6(8):706–711, 2014.

[7] E. Romero, R. Augulis, V. I. Novoderezhkin, M. Ferretti, J. Thieme, D. Zigmantas, and R. van Grondelle. Quantum coherence in photosynthesis for efficient solar-energy conversion. *Nature Physics*, 10(9):677–683, 2014.

[8] J. R. Lakowicz. *Principles of fluorescence spectroscopy*. Springer, New York, New York, 2006.

[9] R. Goss and B. Lepetit. Biodiversity of npq. *Journal of Plant Physiology*, 172:13–32, 2015.

[10] D. J. Mothersole, P. J. Jackson, C. Vasilev, J. D. Tucker, A. A. Brindley, M. J. Dickman, and C. N. Hunter. Pucc and lhaa direct efficient assembly of the light-harvesting complexes in *Rhodobacter sphaeroides*. *Molecular Microbiology*, 99(2):307–327, 2016.

[11] P. Qian, M. Z. Papiz, P. J. Jackson, A. A. Brindley, I. W. Ng, J. D. Olsen, M. J. Dickman, P. A. Bullough, and C. N. Hunter. Three-dimensional structure of the *Rhodobacter sphaeroides* rc-lh1-pufx complex: Dimerization and quinone channels promoted by pufx. *Biochemistry*, 52(43):7575–7585, 2013.

[12] R. J. Cogdell, N. W. Isaacs, A. A. Freer, J. B. Arellano, T. D. Howard, M. Z. Papiz, A. M. Hawthornthwaite-Lawless, and S. Prince. The structure and function of the lh2 (b800-850) complex from the purple photosynthetic bacterium *Rhodopseudomonas acidophila* strain 10050. *Progress in Biophysics and Molecular Biology*, 68(1):1–27, 1997.

[13] V. Sundström, T. Pullerits, and R. van Grondelle. Photosynthetic light-harvesting: Reconciling dynamics and structure of purple bacterial lh2 reveals function of photosynthetic unit. *Journal of Physical Chemistry B*, 103(13):2327–2346, 1999.

[14] R. Hildner, D. Brinks, J. B. Nieder, R. J. Cogdell, and N. F. van Hulst. Quantum coherent energy transfer over varying pathways in single light-harvesting complexes. *Science*, 340(6139):1448–1451, 2013.

[15] M. Şener, J. Hsin, L. G. Trabuco, E. Villa, P. Qian, C. N. Hunter, and K. Schulten. Structural model and excitonic properties of the dimeric rclh1pufx complex from *Rhodobacter sphaeroides*. *Chemical Physics*, 357(1-3):188–197, 2009.

[16] A. Damjanovic, T. Ritz, and K. Schulten. Excitation energy trapping by the reaction center of *Rhodobacter sphaeroides*. *International Journal of Quantum Chemistry*, 77(1):139–151, 2000.

[17] A. F. Fidler, V. P. Singh, P. D. Long, P. D. Dahlberg, and G. S. Engel. Probing energy transfer events in the light harvesting complex 2 (lh2) of *Rhodobacter sphaeroides* with two-dimensional spectroscopy. *Journal of Chemical Physics*, 139(15):155101, 2013.

[18] G. S. Engel, T. R. Calhoun, E. L. Read, T. K. Ahn, T. Mancal, Y. C. Cheng, R. E. Blankenship, and G. R. Fleming. Evidence for wavelike energy transfer through quantum coherence in photosynthetic systems. *Nature*, 446(7137):782–786, 2007.

[19] R. van Grondelle and V. I. Novoderezhkin. Energy transfer in photosynthesis: experimental insights and quantitative models. *Physical Chemistry Chemical Physics*, 8(7):793–807, 2006.

[20] V. Novoderezhkin, M. Wendling, and R. van Grondelle. Intra- and interband transfers in the b800-b850 antenna of *Rhodospirillum molischianum*: Redfield theory modeling of polarized pump-probe kinetics. *Journal of Physical Chemistry B*, 107(41):11534–11548, 2003.

[21] S. Scheuring and J. N. Sturgis. Atomic force microscopy of the bacterial photosynthetic apparatus: plain pictures of an elaborate machinery. *Photosynthesis Research*, 102(2-3):197–211, 2009.

[22] S. Scheuring, T. Boudier, and J. N. Sturgis. From high-resolution afm topographs to atomic models of supramolecular assemblies. *Journal of Structural Biology*, 159(2):268–276, 2007.

[23] G. Mcdermott, S. M. Prince, A. A. Freer, A. M. Hawthornthwaitelawless, M. Z. Papiz, R. J. Cogdell, and N. W. Isaacs. Crystal-structure of an integral membrane light-harvesting complex from photosynthetic bacteria. *Nature*, 374(6522):517–521, 1995.

[24] D. E. Chandler, J. Strumpfer, M. Sener, S. Scheuring, and K. Schulten. Light harvesting by lamellar chromatophores in *Rhodospirillum photometricum*. *Biophysical Journal*, 106(11):2503–2510, 2014.

[25] A. Chenu and G. D. Scholes. Coherence in energy transfer and photosynthesis. *Annual Review of Physical Chemistry*, 66:69–96, 2015.

[26] M. Reppert. Modeling of resonant hole-burning spectra in excitonically coupled systems: The effects of energy-transfer broadening. *Journal of Physical Chemistry Letters*, 2(21):2716–2721, 2011.

[27] P. Rebentrost, M. Mohseni, I. Kassal, S. Lloyd, and A. Aspuru-Guzik. Environment-assisted quantum transport. *New Journal of Physics*, 11(3):033003, 2009.

[28] V. P. Singh, M. Westberg, C. Wang, P. D. Dahlberg, T. Gellen, A. T. Gardiner, R. J. Cogdell, and G. S. Engel. Towards quantification of vibronic coupling in photosynthetic antenna complexes. *Journal of Chemical Physics*, 142(21):212446, 2015.

[29] P. Hamm and M. T. Zanni. *Concepts and methods of 2D infrared spectroscopy.* Cambridge University Press, New York, New York, 2011.

[30] S. Mukamel. *Principles of nonlinear optical spectroscopy.* Oxford University Press, New York, New York, 1995.

CHAPTER 2

DESIGN AND OPERATION OF SELECT NONLINEAR SPECTROSCOPY INSTRUMENTS

The previous chapter outlined the system of study, *Rba. sphaeroides*, as well as the theoretical formalism for the optical spectroscopies. This chapter is devoted to the practical aspects of measurement and analysis of third-order spectroscopies. When building a spectrometer for time domain spectroscopy there are many things to consider, beginning with the excitation source. These sources can be everything from microsecond duration flash lamps discussed in Section 2.1 to femtosecond mode-locked lasers discussed in Section 2.3.2. [1–4] The type of excitation source greatly affects the method used to control the timing between excitation pulses. Often the first two light matter interactions discussed in the previous chapter occur from one excitation source while the third interaction comes from a separate source. The timing is controlled between the two and encodes the waiting time dynamics. This is the case for any experiment operating on the tens of nanoseconds and beyond. For ultrafast experiments, i.e. those with time delays below a few nanoseconds, a single excitation source is used and split into several paths and the length of each path is modulated to achieve the desired timing between pulses. The timing in ultrafast experiments comes from the speed of light, 300 nm/fs. For example, a delay of 3 nanoseconds can be achieved by increasing the path length of one path by 900 mm. After interactions with the sample the emitted signal field is generated and needs to be detected. The field can be spectrally resolved or not depending on the application. Often much better signal to noise on time dynamics can be achieved when the signal is not spectrally resolved, but this can also lead to significant confusion if the field is not homogeneous. [5] For instance, if the signal is positive for some wavelengths and negative for others there could be cancellation. The following sections outline several instruments constructed during the thesis and in no way encompass all the different time resolved apparatus possible. Rather the aim of this chapter is to aid future students who

want to construct new equipment, modify equipment, or simply use the existing apparatus. All the code to run the instruments as well as the analysis software is included in a digital supplement to the thesis.

The final section in this chapter discusses an instrument that is at the frontier of nonlinear spectroscopy. This instrument has exquisite sensitivity on the fs-ps timescales, but it is important to remember that there are many dynamics beyond these timescales that this instrument cannot capture. Without knowledge of the dynamics occurring on long timescales the context for the ultrafast dynamics can be lost. An example of this comes from my lab notebook at the start of my second year, see Figure 2.1. We were struggling to understand a signal arising at negative times in a transient absorption experiment. Signals at negative times often result from sample bleaching and long-lived states. After several failed attempts to understand what was going I performed a relatively simple flash photolysis experiment, explained in Section 2.1, that revealed a long-lived charge separated state in the RC sample being measured. While the ultrafast experiment was attempting to understand ultrafast energy transfer dynamics in the RC the signal was in fact dominated by this long-lived state. This understanding led to a revision of the sample preparation and a successful experiment, but provides a cautionary tale to always understand the temporal extent of the transient signal.

2.1 Flash Photolysis

Flash photolysis is a simple time resolved experiment, but the instrumentation required introduces many of the concepts for more advanced time resolved spectroscopies, making it well suited to begin a discussion on time resolved instrumentation. [4] In a flash photolysis experiment, the first two interactions with the sample come from a flash lamp very similar to a camera flash. The flash lamp in the case of the instrument described here is a xenon flash lamp with a pulse duration of ≈ 1.5 μs as measured by a silicon photodiode and a digital oscilloscope shown in Figure 2.2. The duration of the flash limits the temporal resolution

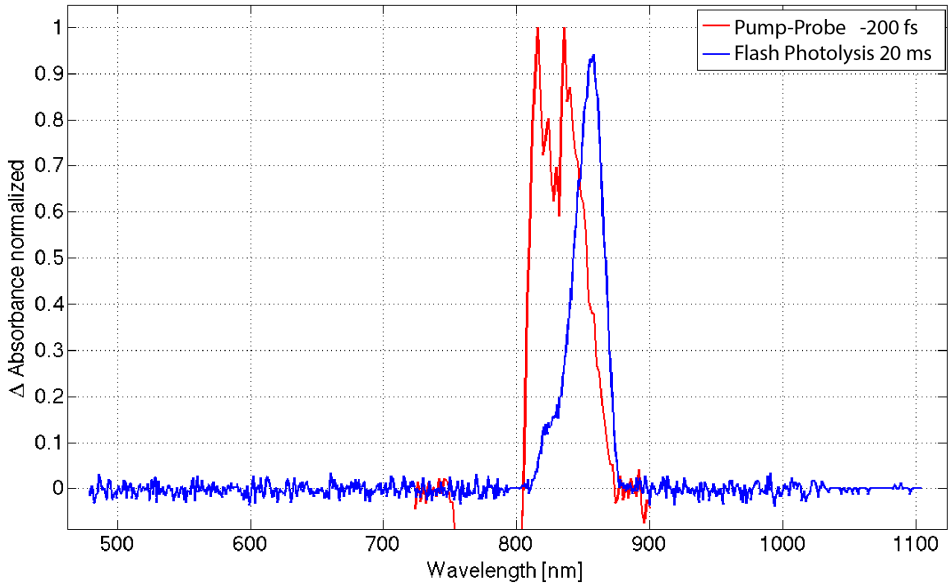

Figure 2.1: Femtosecond transient absorption measurement and millisecond transient absorption measurement of RC from *Rba. sphaeroides*. The long time experiment was conducted on a much simpler experiment, but provides important context for the femtosecond dynamics and reveals that the femtosecond experiment had significant contamination from a long-lived charge separated state.

for this type of instrument. Figure 2.3 shows a diagram of the apparatus. The spectrum produced by the flash lamp is quite broad, covering much of the visible and UV. Often a more narrow band excitation is desired because a narrow band excitation can selectively excite a given state. This narrowband excitation can be achieved with absorptive glass filters placed in front of the flash lamp. The light from the flash has significant dispersion and in order to get sufficient flux to the sample a cylindrical lens is used to focus the light to a line on a 1 cm cuvette. After optical excitation, the excited states generated by the flash can now be probed. This can be achieved several ways, but typically for experiments on the microsecond timescale or longer the probe light is a steady state source, such as the LED used in this apparatus.* The data displayed in Figure 2.3 comes from a NIR LED and the sample is bacterial reaction centers. † The experiment is monitoring the oxidized special pair and its recovery which shows a ground state bleach signal in the NIR spectrum. The ground state bleach signal is detected as the change in transmitted light when the flash is present versus when the flash is absent. This difference can be spectrally resolved using a spectrometer and a linear array detector (top of Figure 2.3) or detected on a single photodiode to give superior signal to noise in the time domain, but no spectral information.

To accurately control the timing on the μs to ms timescales there are two options. The best option is an electrical signal sent to both the detector and the flash lamp simultaneously that triggers the flash and begins acquisition. This TTL signal can come from an Arduino or Labjack (similar to an older version of an Arduino) that is triggered by software. The second option is to synchronize the excitation and detection directly using software, but this leads to substantial timing jitter. Most flash lamps will have a port for a TTL signal to trigger a flash. The timing jitter between the arrival of the TTL signal and the flash output should be

∗. Thorlabs Inc. sells a wide variety of high power mounted LEDs that are great for this application because they can be broadband or narrow band depending on the application.

†. In the reaction center, charge separation occurs rapidly on the order of picoseconds on the special pair of Bchl*a*. The charges are then separated as an electron is transferred to one of two quinones called Q_A and Q_B leaving behind a hole on the special pair. In the isolated sample of reaction centers there is no cytochrome to re-reduce the special pair and the only possible decay pathway is recombination which occurs on roughly a 100 ms timescale from Q_A and a 500 ms timescale from Q_B. [6, 7]

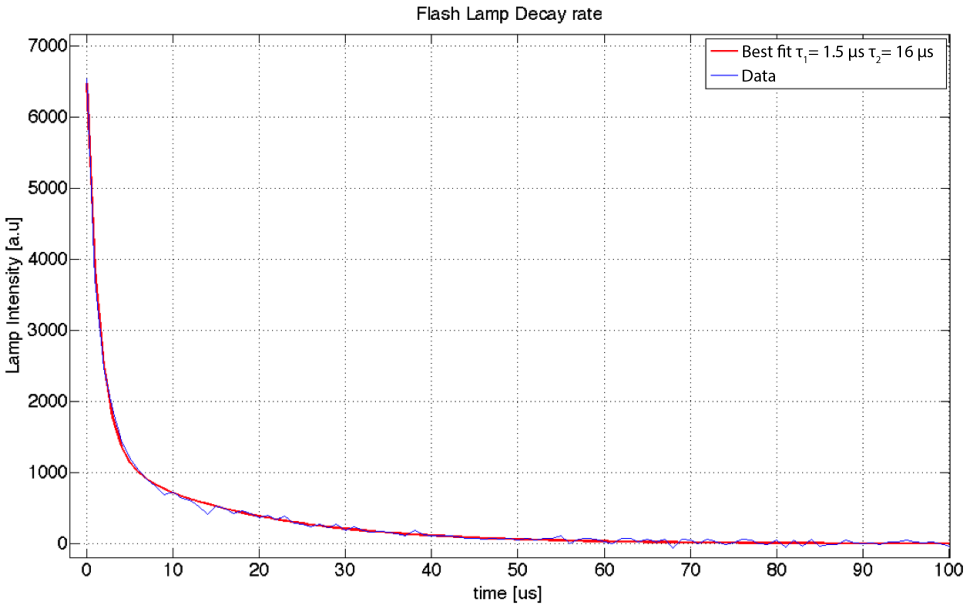

Figure 2.2: Duration of the xenon flash lamp used for flash photolysis. The lamp shows a bi-exponential decay with a strong 1.5 μs feature and a weak 16 μs feature. The duration of the flash limits the temporal resolution of the instrument to microseconds or longer.

sub microseconds. Instead, problems arise when triggering the detection. In the case of the single photodiode, triggering detection is not too difficult. The voltage at the diode is being amplified and transmitted to a digital oscilloscope. Picotech sells robust, high signal to noise, and cheap oscilloscopes called Picoscopes that interface well with control software, such as Labview. The Picoscope 4262 used here has two channels with a sampling rate of 10 MS/s at 16 bits, and a digital storage of 16 MS. One channel is connected to the photodiode and the other is connected to the TTL signal. The Picoscope can then be programmed to save the several million samples before the arrival of the TTL signal as well as the many millions of samples after the TTL signal. This sampling will give a time series of the dynamics after excitation with the flash that can be compared to the intensity of the LED before the arrival of the flash. The jitter in the timing in this case is less than the duration of the flash lamp pulse. In the case of the spectrally resolved signal there is no way to trigger acquisition from a TTL signal. At the time of writing this, this is true for both Ocean Optics spectrometers as well as Thorlabs spectrometers. The lack of TTL trigger forces the use of a software trigger

that has several ms of timing jitter and limits the temporal resolution of the instrument by 3-4 orders of magnitude. For the bacterial reaction center studied here this does not present a significant problem as the dynamics are occurring on the ms timescale and longer, but is an unfortunate problem for most other applications.

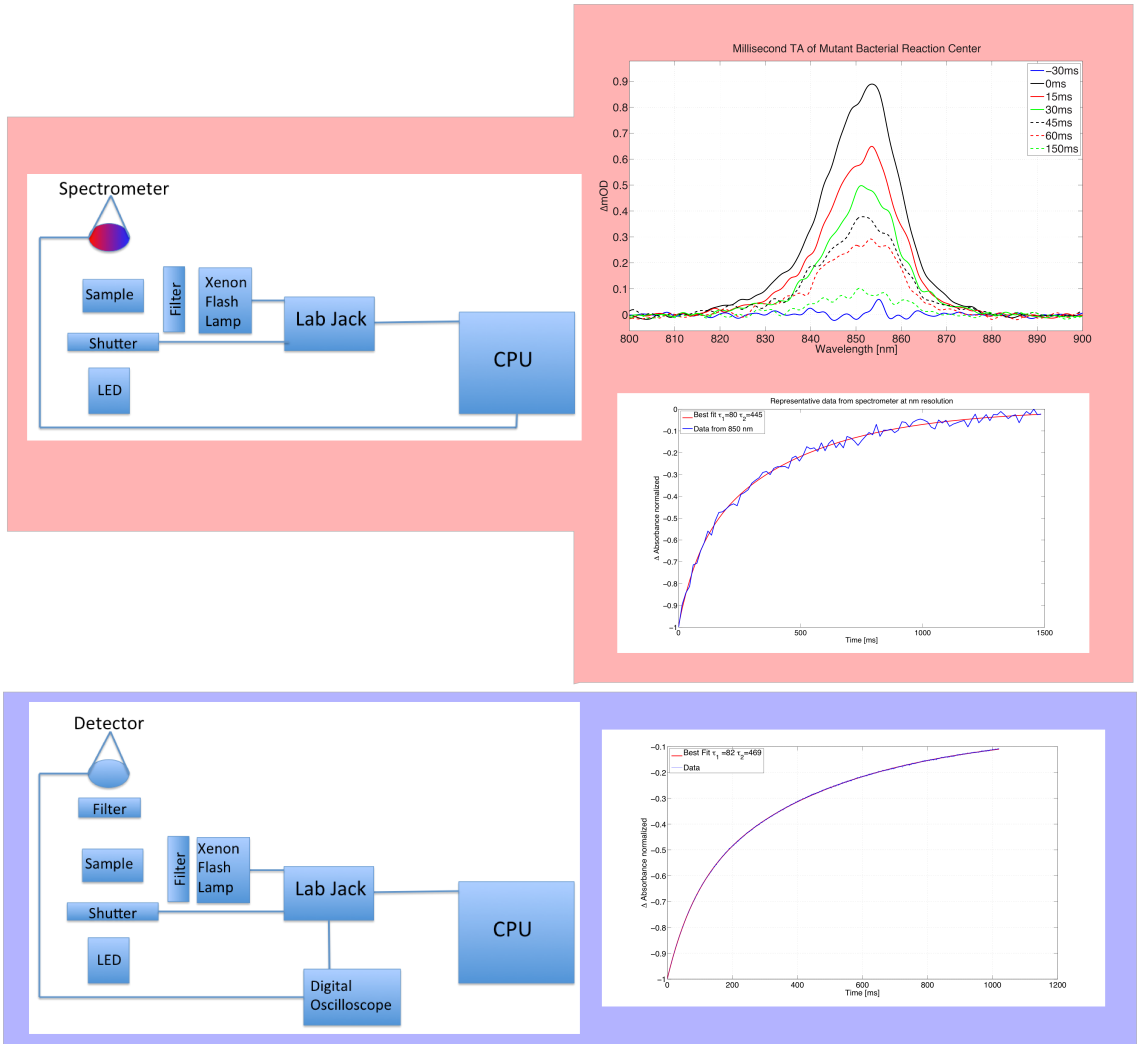

Figure 2.3: The two figures on the left are the diagrammatic representation of the flash photolysis apparatus with a USB fiber optic coupled spectrometer *(top)* and a fast silicon photodiode *(bottom)* for detection. The data to the right shows the difference spectra after excitation with the flash lamp and the trace from this decay at 850 nm. The trace at 850 nm from the spectrally resolved signal can be compared to the signal below from the fast photodiode that is not spectrally resolved. The significant improvement to signal to noise comes from many sources, but the dominant sources are the improved electronic amplifiers for a single photodiode as well as the superior bit depth of the oscilloscope that digitizes the signal.

2.2 Transient Absorption

The nanosecond to microsecond timescales are the relevant timescales for many interesting types of dynamics. For instance, singlet excited states often have a lifetime of a few ns, triplets can be tens of nanoseconds to ms, and charge separated states are often hundreds of nanoseconds to ms. [8] The lifetimes and dynamics of these states are crucial to understanding most systems including photosynthetic light harvesting systems.

The instrument shown in Figure 2.4 uses two different lasers to interact with the sample. The first two interactions come from a narrow band picosecond Nd:YAG laser that is tripled and then pumps an OPO that produces $\approx$ 25 picosecond pulses (Ekspla PL2210 and Ekspla PG403). The OPO can easily be tuned throughout the visible region of the electromagnetic spectrum. Because this laser produces the population states after the first two interactions it is often called the "pump" beam. The third interaction is performed by a supercontinuum generation fiber laser that has a broad spectrum from 350 nm - 1 μm and a pulse duration of $\approx$600 ps (Leukos-STM). This laser is often called the "probe" laser and the experiment is called a pump-probe experiment. A conceptual picture that many have in mind for a pump-probe experiment is that a photon of light is absorbed by the sample from pump laser, producing excited states, and then that state is probed by a photon from the probe laser. This probe photon can be absorbed giving excited state absorption, stimulated emission, or be transmitted when it would have otherwise been absorbed due to ground state bleach. This manner of thinking about the experiment gives rise to all the same signals and even the same dynamics as the formalism laid out in Section 1.4. However, this description breaks down for more complex experiments, such as the one described in Section 2.3.2.

A diagram of the pump-probe apparatus can be seen in Figure 2.4. The optics after the generation of the two laser pulses are quite simple. The only requirements are that the beams overlap in the sample and that sometime after the sample the pump light is blocked in order to avoid saturation or damage of the detection optics. One thing to consider is the overlap of the two beams in the sample and their relative flux. It is beneficial to make the spot size

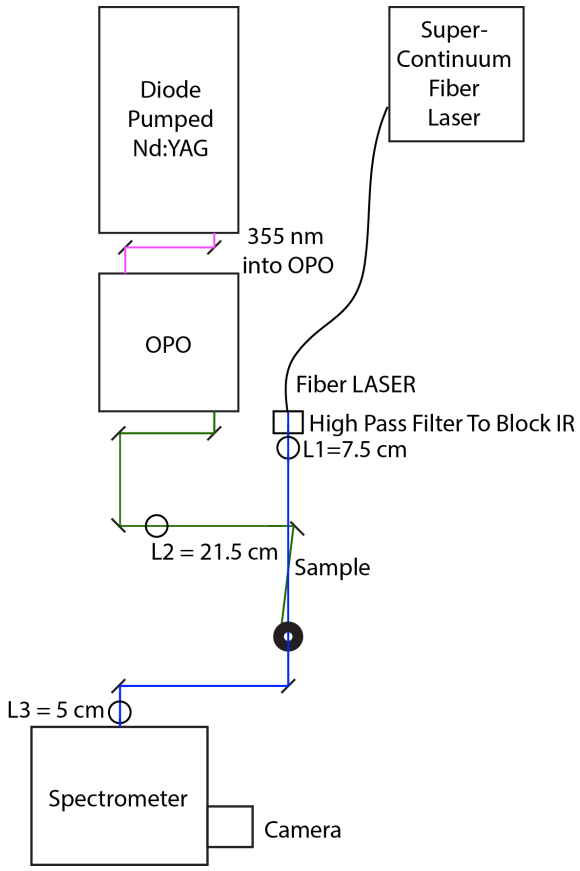

Figure 2.4: Optical layout for the nanosecond transient absorption apparatus. The assembly is quite simple, the only restrictions are to overlap the pump and probe lasers temporally and spatially at the sample and to get just the probe laser into the spectrometer and onto the camera.

of the pump laser larger at the sample than the probe laser, hence the use of a slow-focusing lens for the pump (21.5 cm) and a faster focusing lens for the probe (7.5 cm). A large pump beam allows for some amount of spatial drift between the two lasers without greatly impacting the signal strength. The relative flux between the two lasers is also important. Because two light-matter interactions have to occur with the pump laser it should be more intense. In theory the relative intensity is related to the transition dipole strength of the absorbers, but in practice the powers are set to optimize signal to noise. The probe light is increased until it is close to saturating the readout electronics and the pump intensity is increased until a change in dynamics (due to bleaching, heating, multi-exciton effects, etc.) is observed and then the intensity is reduced just below this threshold. Typically, this results in the pump laser being 1-20 nJ in a 100 μm diameter spot, or about 1-2 orders of magnitude more intense than the probe laser .

An essential part of this instrument is the precise timing and synchronization between

the two lasers. Figure 2.5 shows the timing electronics in detail. The synchronization is achieved by using a common 1 kHz clock that arises from the pump laser, making the probe laser the slave. This common clock produces timing jitter between the two instruments that is less than the pulse duration of the fiber laser making the fiber laser the limiting factor for the instrument response function, which is shown in Figure 2.6. The timing between the pump and probe lasers is achieved with a delay generator, SRS 535, that is controlled with labview. The emitted field is then spectrally resolved in spectrometer and imaged on a linescan camera (Teldyne Dalsa Spyder3 2k).‡ Linescan cameras are typically a linear array of CCD or photodiode pixels. They usually contain a power of 2 pixels in width i.e. 1024 or 2048 and are 1-4 pixels in height. They have two different types of triggers, a line trigger and a frame trigger. The line trigger, as the name implies, triggers one acquisition of the sensor. The camera then builds up a frame by acquiring many lines and putting them into one image. The frame trigger defines when to start an acquisition. Both triggers are used when applying linescan cameras to transient absorption measurements. Similarly to Section 2.1 where the measurement was a difference of the intensity of the probe light when the flash was present and when it was absent, here we will measure a difference in the spectrum of the probe laser that is passed through the sample with and without the pump laser. The frame trigger is used to synchronize the camera frame to start with a spectrum of the probe laser when the pump is present and the line trigger is used to synchronize the camera to the probe laser so that every time the probe fires a spectrum is acquired. Often, the pump laser

‡. Linescan cameras were originally designed for industrial use in factories where they would be used to scan barcodes of products in an assembly line. This application meant that the cameras needed to be fast and externally triggered, making them well suited for transient absorption measurments. It has been my experience that products designed for broad applications that have large commercial markets are far more robust, affordable, and have superior specifications when compared to products designed specifically for the rather small scientific market. This is important to keep in mind when building instruments as it might impact the equipment used. For example the USB fiber optic spectrometer from the flash photolysis described in Section 2.1 could have been used in this instrument, however, the linear photodiode array, readout electronics, and user interface in the USB spectrometer (a product designed for the scientific community) are vastly inferior to their counterparts in the linescan camera. For instance, both are 12 bit detectors, but the line rate for the spectrometer is 75 Hz and the camera is 36 kHz despite both products being of comparable cost.

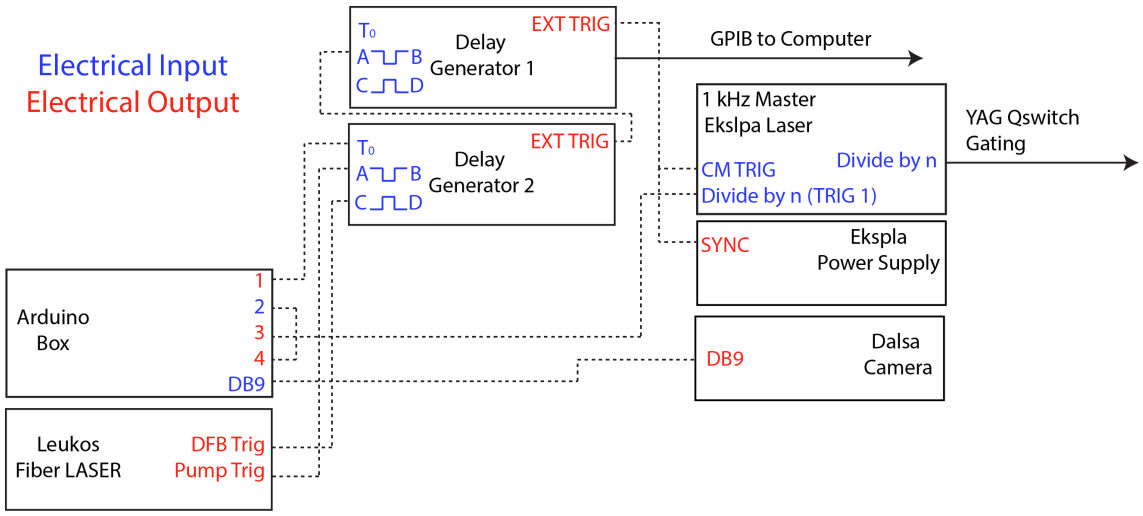

Figure 2.5: Diagram of the electronics that control the timing in the apparatus. The 1 kHz master clock is given as an output from the Ekspla (pump) laser and is given as both the line trigger for the camera and the external synchronization trigger for DG1. DG1 is then used to generate the delay between the pump and probe laser by sending a delay trigger to DG2 that in turn sends the necessary Qswitch triggers to fire the probe laser. The Ekspla also provides the frame trigger with the output of the 1 kHz signal divided by an integer used to reduce the repetition rate of the pump laser relative to the probe laser. The frame and line trigger are connected to a 9 pin connector that triggers the acquisition of the probe spectrum on the linescan camera.

is set to have a repetition rate one half that of the probe laser. In this case, that is 500 Hz for the pump and 1000 Hz for the probe. This leads to a frame that alternates between the probe spectrum absent the pump and the probe spectrum with the pump. The difference between the even and odd frames gives an average of the transient spectrum for a given waiting time. For long lived charge separated states 1 ms might not be enough time for the state to recover back to its ground state. If this is the case signals will appear at negative times, as discussed at the beginning of the chapter. In order to acquire accurate data in this situation, the pump laser repetition rate can be reduced to as little as 0.1 Hz allowing for the acquisition of dynamics for much longer lived species. Figure 2.7 gives an example of a long waiting time scan where the pump had a repetition rate of 10 Hz. We see the decay of an excited state absorption feature that arises due to a charge separated state.

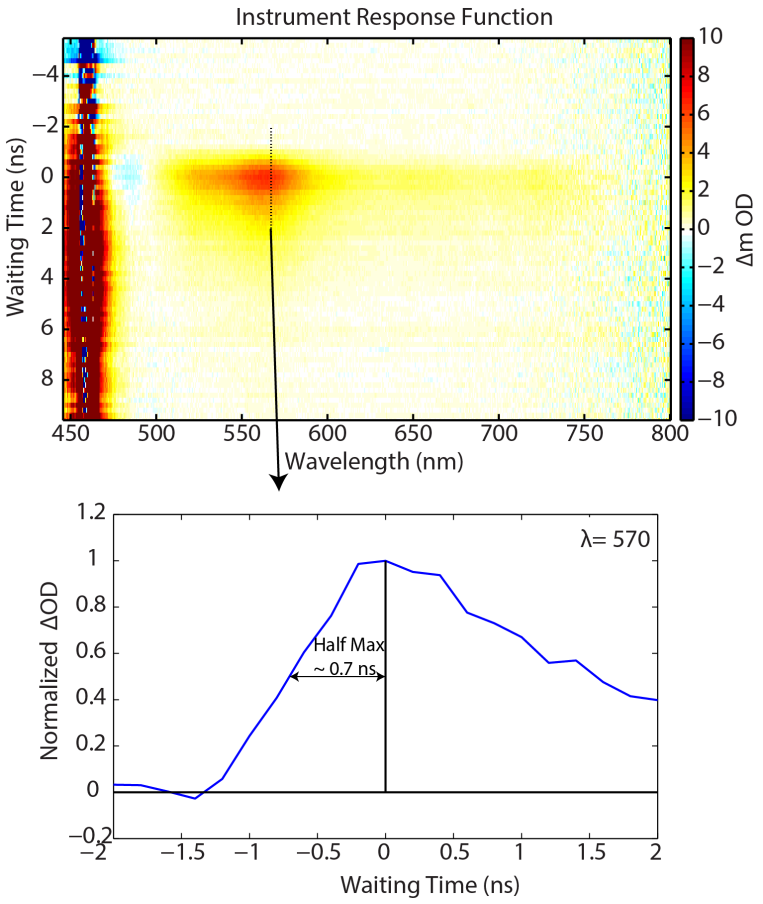

Figure 2.6: Instrument response function measured through the rise time of an excited state absorption feature. The instrument response is dominated by the duration of the probe laser, which is $\approx$ 600 ps

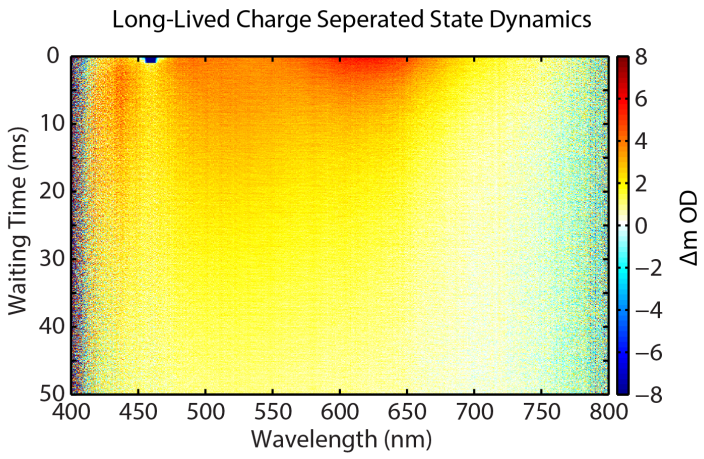

Figure 2.7: Waiting time scan to a time delay of 50 ms showing the recovery of a long-lived charge separated state. This figure highlights the instrument's ability to recover dynamics over 9 orders of magnitude in time

2.3 Ultrafast Spectroscopy

Much of the instrumentation described in sections 2.1 and 2.2 has to do with the electronics that control the timings between different laser pulses. For ultrafast lasers, those with pulse durations less than one picosecond, electronic timing circuits are insufficient and would limit the instrument response function. Instead, timing in ultrafast spectroscopy measurements is achieved through optical delay lines that alter the path length that beams of light travel. [2, 9] Another consideration is the temporal pulse compression. [10] In ultrafast lasers a transform limited pulse, i.e. a pulse whose Fourier transform in the frequency domain is equivalent to the pulse in the time domain, requires all wavelengths of light that make up the pulse to be in phase with each other. As the pulse propagates through material, for instance a glass lens, each wavelength is delayed differently since the index of refraction is dependent on the frequency of light. [11] The frequency dependence of the index of refraction disrupts the phase relationship between the different wavelengths and can lead to a broadening of the pulse in the time domain. For this reason, transmissive optics in ultrafast apparatus are kept to a minimum, and when used, must be identically path lengths must used in all beam paths in the experiment. An additional difference when working with ultrafast pulses and

picosecond delays is the presence of interferograms. This is discussed in great detail in the following sections as well as in chapter 4.

2.3.1 Ultrafast Transient Absorption

Figure 2.8 shows a diagram of the ultrafast transient absorption apparatus. The setup has been constructed on a breadboard so that it can easily be moved to the different two-dimensional electronic spectrometers in the Engel Group. An input beam is separated into two beams using a glass wedge. This gives a fresnel reflection for the probe beam while the transmitted light is the pump. The wedge is important because it ensures that the back reflection does not co-propagate with the probe beam. The timing between the pump and probe pulses is controlled using a motorized translation stage (Aerotech ANT130) that varies the path length the pump takes to the sample. After separation, the probe passes through compensating glass to ensure equal compression of the pump and probe pulses and down a delay line to optimize the delays achievable by the motorized stage. A chopper is used to modulate the pump beam at 1/2 the repetition rate of the probe beam. In this apparatus the probe is at 5 kHz and the pump is at 2.5 kHz. The beams then propagate to the sample where they cross and the pump is blocked at an iris shortly following the sample and a 90 degree turn. Both the turn and the iris help to eliminate scattered light from the pump contaminating the emitted signal field. I found that this suppression of scatter was insufficient and an additional iris was placed before the spectrometer. The probe and the emitted signal field are spectrally resolved and imaged on the ccd camera.

It is worth discussing in detail the actual signal that is recovered on the camera in terms of the electric fields. Much of the analysis software is understandable once an understanding of the fields present is obtained. The camera measures the intensity of the light, which goes as the electric field squared, not the electric field directly. When the pump is present the

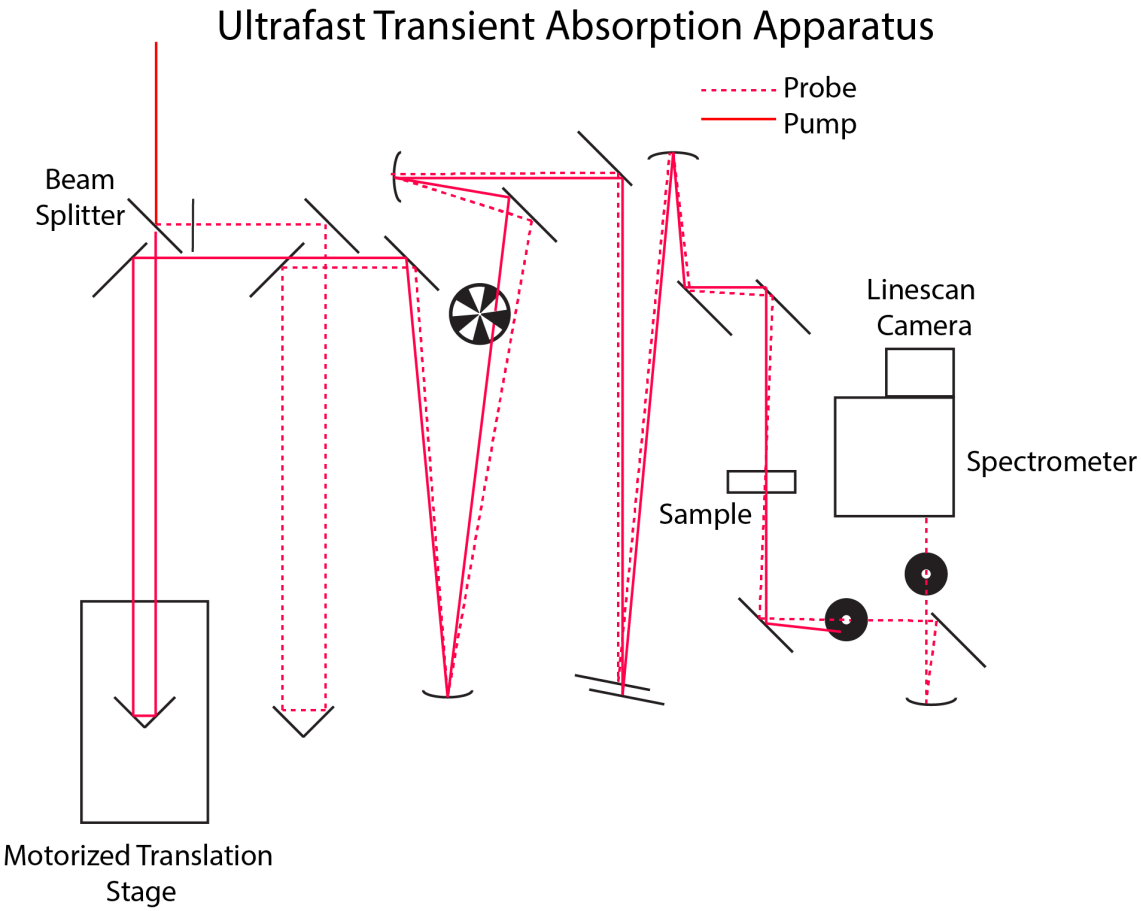

Figure 2.8: Optical layout for the ultrafast transient absorption apparatus showing the path traversed by the pump and probe beams. The pump is moved in time relative to the probe using an Aerotech delay stage and is modulated at 1/2 the repetition rate of the laser (5 kHz laser) with an optical chopper (Thorlabs MCL2000). The signal is field is heterodyne detected with the probe field and is spectrally resolved on a linescan camera.

light on the detector is proportional to

$$I_{cam} \propto |E_{pump} + E_{probe} + E_{sig}|^2 \tag{2.1}$$

$$= E_{pump}^2 + E_{probe}^2 + E_{sig}^2 + E_{pump}^* E_{probe} + E_{pump}^* E_{sig} + E_{probe}^* E_{sig} + c.c. \tag{2.2}$$

The first three terms are called the homodyne because the fields are interfering with themselves. The last three as well as their complex conjugates are the heterodyne components. Ideally, no light from the pump would be present because it would be blocked by the irises shown in Figure 2.8. In practice this is impossible to achieve and often the scattered light from the pump is significantly larger than the the signal we want to detect, E_{sig}. We detect E_{sig} not through its homodyne, as this is incredibly weak, but rather through its interference with the probe light in the term $E_{probe}E_{sig}$. The question is how to go from the large interferogram presented in the equation above to just a measure of $E_{probe}E_{sig}$. To begin with we take a spectrum when the pump is blocked by the chopper. This leads to a measure of only the probe intensity.

$$I_{cam} \propto |E_{probe}|^2 \tag{2.3}$$

$$= E_{probe}^2 \tag{2.4}$$

the subtraction of Equation 7.2 from Equation 7.1 and neglecting the weak signal homodyne yields

$$I_{cam} \propto E_{pump}^* E_{probe} + E_{pump}^* E_{sig} + E_{probe}^* E_{sig} + c.c. \tag{2.5}$$

A scan of the waiting time delay causes the electric fields of the pump and probe to oscillate between constructive and destructive interference at each wavelength. The top of Figure 2.9 shows data collected on a mutant of LH2 that lacks the B800 ring of chromophores

after subtraction of the probe only spectra, giving the fields present in Equation 7.3. The interference of $E_{pump}E_{probe}$ and the much weaker interference of $E_{pump}E_{sig}$ shows up as ripples that converge at $T = 0$ in the camera frequency versus waiting time plot because all wavelengths in the spectrum (if well compressed) are in phase at $T = 0$ and constructively interfere. On the bottom of Figure 2.9 a Fourier transform has been computed over the waiting time domain to produce a frequency-frequency spectrum. Here the interference shows up as a clear line due to the fact that at each wavelength the fields are oscillating between constructive and destructive interference at their optical period. The signal of interest, $E_{probe}E_{sig}$, has slow dynamics causing it to primarily show up near a waiting time frequency of zero. The separation of the scatter and the signal of interest in this domain allows for apodization (windowing) around zero frequency to isolate the signal of interest. This technique works best when the waiting time can be sampled more finely than the optical period of light. For 800 nm light the optical period is 2.67 fs and we typically sample in 1 fs steps. Under sampling the signal for example in 5 fs steps can be done with careful consideration of where the optical frequency is being aliased, but it is best to sample finely if possible.

After apodization we are left with

$$I_{cam} \propto E_{pump}^2 + E_{probe}^* E_{sig} + c.c. \tag{2.6}$$

The only remaining term other than the signal is the homodyne of the pump field. After this analysis the only field that should be present at negative waiting time delays is in fact the pump homodyne because there is no signal field at these delays. Thus the final step to isolate the signal of interest is to subtract the average spectrum at negative times. As can be seen in Figure 2.9 this homodyne component should be weak and this step is often not performed. If there is substantial signal at negative times it is likely not due to the homodyne scatter but long-lived states, and the repetition rate of the pump beam should be reduced to allow the system to recover to its ground state, or if possible the flow rate of the

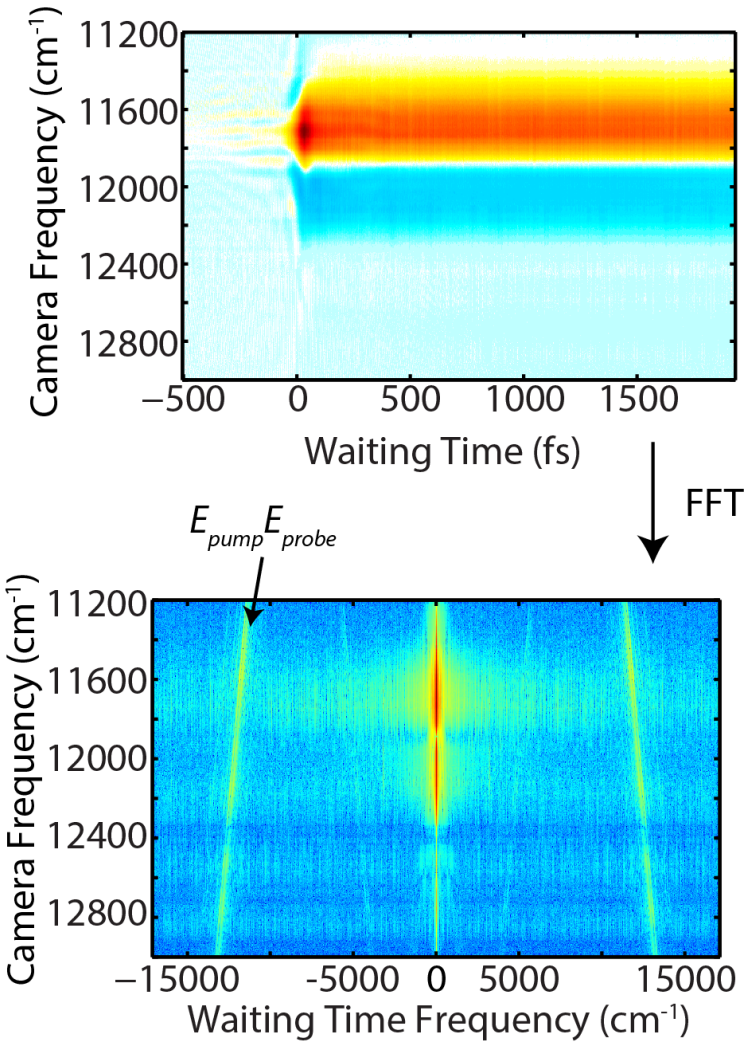

Figure 2.9: Ultrafast transient absorption data of the B850 feature from LH2. The interference between $E_{pump}E_{probe}$ shows up as ripples in the frequency-time domain and as a line that is separable from the signal of interest in the frequency-frequency domain.

sample should be increased to clear the sample between pump excitations.

2.3.2 Developments In Gradient Assisted Photon Echo Spectroscopy

A significant component of this thesis has been the improvement of the GRadient Assisted Photon Echo Spectrometer (GRAPES). The original GRAPES instrument has been reviewed elsewhere. [12, 13] This section will discuss the improvements made to the instrument since its initial construction. These improvements include new analysis and acquisition techniques that eliminate significant scatter contributions, an additional reduction in experiment time by three orders of magnitude, and new analysis techniques that provide absorptive lineshapes. The application of these improvements to the study of photosynthetic energy transfer in living *Rba. sphaeroides* is the focus of chapters 4, 5 , 6, and 7.

In two-dimensional electronic spectroscopy, 2DES, three ultrafast pulses interact with the sample at time intervals controlled using optical delay stages discussed in Section 2.3.1. The resulting signal on the camera in a 2DES experiment is similar, but slightly more complex than in a pump-probe experiment because the two interactions that occur with the pump beam are separated into interactions with two different beams. In addition the signal field is emitted in a unique phase matched direction, discussed in Section 1.4 and is mixed with a reference pulse called the local oscillator (L.O.). The signal on the camera is

$$\begin{aligned} I_{cam} \propto |E_1 + E_2 + E_3 + E_{L.O.} + E_{sig}|^2 & \\ = |E_1 + E_2|^2 + |E_3 + E_{L.O.}|^2 + E_{sig}^2 & \\ + E_1^* E_3 + E_2^* E_3 + E_1^* E_{L.O.} + E_2^* E_{L.O.} + E_3^* E_{sig} + E_{L.O.}^* E_{sig} + c.c. & \quad (2.7) \end{aligned}$$

The signal of interest is, as before, not the homodyne of E_{sig}, but rather the interference of the signal field with the reference pulse $E_{L.O.}$ in the term $E_{L.O.}E_{sig}$. The timing of the local oscillator relative to the signal field can be experimentally controlled and is usually

set to a delay of several picoseconds. This a key distinction from pump-probe spectroscopy where the emitted signal is heterodyne detected with the probe field. In pump-probe, the two fields, E_{probe} and E_{sig} have no time delay between them leading to an interference pattern on the camera that is not oscillatory across frequency. The oscillatory signal of interest in 2DES can be used to isolate the signal of interest from scatter in ways that are not accessible in pump-probe experiments, making 2DES well suited for experiments with significant scatter contributions.

The scatter contributions can be divided into two types, "dynamic scatter" and "static scatter". Dynamic scatter is scatter coming from any surface that is changing rapidly during the experiment time, for example cells flowing through the focus of the laser. Static scatter sources remain constant during the experiment time and arise from things like cracks in a cryogenic glass. Dynamic scatter produces an interferogram that has a random phase on the camera. If enough of these interferograms are acquired then the dynamically scattered light becomes smoothly varying across the camera. The signal, however, maintains a constant phase even as the sample is flowing because this phase is set by the phase of the interacting light fields. Figure 2.10 shows two raw images from the camera both of the same sample of mutant *Rba. sphaeroides* cells that contain only LH1 and LH2 complexes. The image on the left is produced when the sample is flowing and producing significant dynamic scatter. The image on the right is when the sample is not flowing and produces only "static" scatter that adds on the camera with a constant phase.

The blurring out of dynamic scatter cannot be utilized in a pump-probe experiment because the desired interferogram $E_{probe}E_{sig}$ is itself slowly varying across the camera. Instead scatter in pump-probe is removed in the manner describe above in Section 2.3.1 and relies on rapid sampling of the waiting time domain and static scatter. In GRAPES, and indeed all 2DES, the removal of dynamic scatter is easily accomplished through the integration of many spectra on the camera, but the static scatter must be removed through similar apodization procedures described in Section 2.3.1 and also relies on fine sampling of the waiting time.

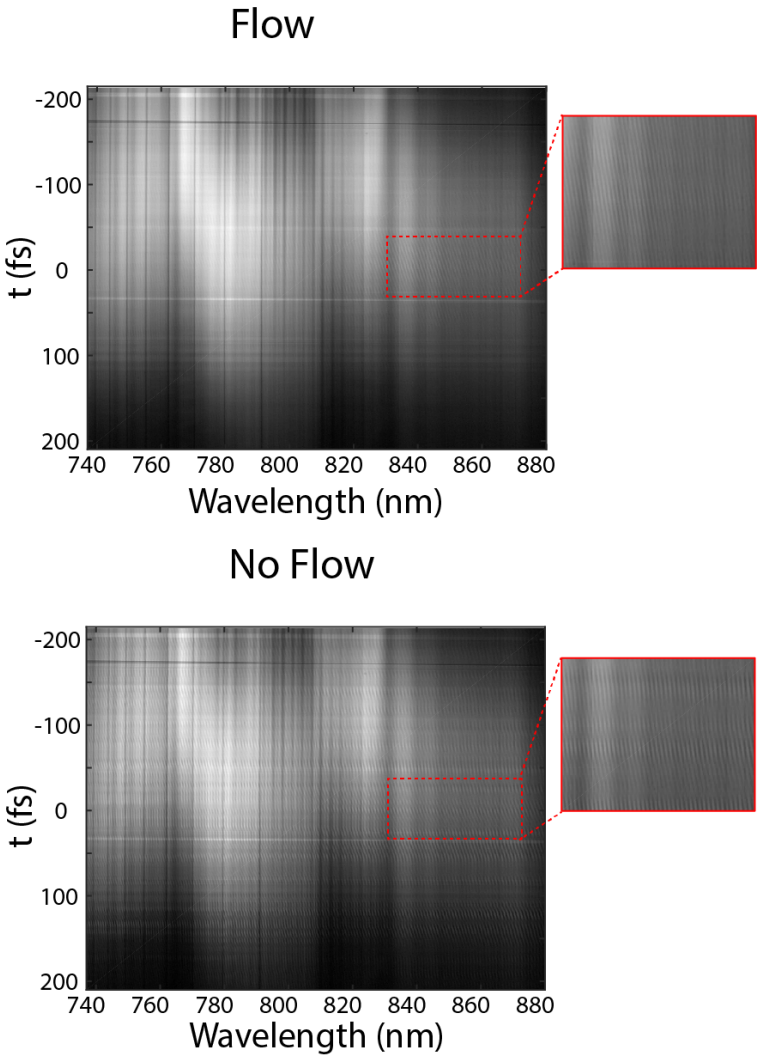

Figure 2.10: Two raw data images collected with GRAPES on mutant *Rba. sphaeroides* cells that contain only LH1 and LH2. The image on the left is when the sample is flowing rapidly that prouduces highly dynamic scatter. The zoomed region shows a faint interferogram that encompasses the signal of interest. The image on the right is when the sample is not flowing and produces static scatter. The zoom region shows a strong interferogram that is largely the result of scatter and not the signal of interest.

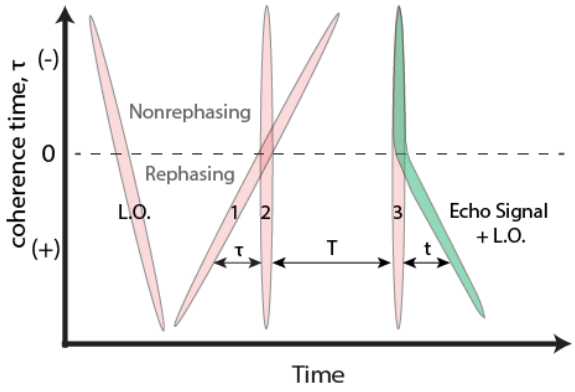

Figure 2.11: Pulse sequence in GRAPES showing the gradient between pulses one and two that is used to spatially encode the coherence time delay.

Fine sampling of the waiting time is typically hard or impossible to achieve in 2DES because this sampling leads to prohibitively long experiment times. The GRAPES instrument cleverly encodes the coherence time, the time between the first two interactions, spatially at the sample rather than using an optical delay stage, see Figure 2.11. By encoding one time delay spatially, the waiting time delay can be sampled much more quickly. To achieve this rapid sampling, the original cooled CCD camera used in GRAPES has been replaced with a high speed camera with a frame rate up to 5 kHz (Phantom Miro M310). This high speed camera leads to the large reduction in experiment time and makes possible a more finely sampled waiting time delay. This fine sampling allows for the removal of scatter in a similar fashion to that outlined in Section 2.3.1. The details of this scatter removal are outlined in the first experiment conducted in living cells in chapter 4.

The initial experiments conducted with the fast camera were acquired with a frame rate of 5 kHz in order to follow the scatter removal techniques described in the more established field of pump-probe spectroscopy. The realization that dynamic scatter can be removed through simple integration led to a reduction of the frame rate to 50 Hz. An improvement in signal to noise that roughly scaled with the square root of the number of laser pulses collected i.e. from 5 kHz $\rightarrow$ 50 Hz each frame contained 100 times the laser shots and an order of magnitude improvement in signal to noise was achieved.

A significant limitation of GRAPES is its inability to collect non-rephasing spectra. In

nonrephasing spectra the coherence generated between the first two light matter interactions evolves phase in the same direction as the coherence after the third interaction. The nonrephasing spectra are detected in the same phase matched direction as the rephasing signal if the order of beams 1 and 2 are reversed. This occurs in GRAPES, as can be seen in Figure 2.12, but negative coherence times do not have a uniform waiting time. The fine sampling of the waiting time makes it possible to restructure the data. If the waiting time steps are taken at the same intervals as the coherence time steps (the gradient between pulses 1 and 2 results in $\approx$ 0.9 fs steps in τ) then the frames can be interpolated to give negative coherence time values with uniform waiting times. The recovery of nonrephasing data allows GRAPES to produce completely absorptive lineshapes. Absorptive lineshapes are calculated from the sum of the rephasing and the nonrephasing spectra and accurately measure both the homogenous and inhomogenous lineshapes, unlike rephasing and nonrephasing spectra on their own, which suffer from twisted lineshapes. Figure 2.13 shows the rephasing-only lineshape that has a twist towards the diagonal versus the absorptive lineshape, which is more stacked.

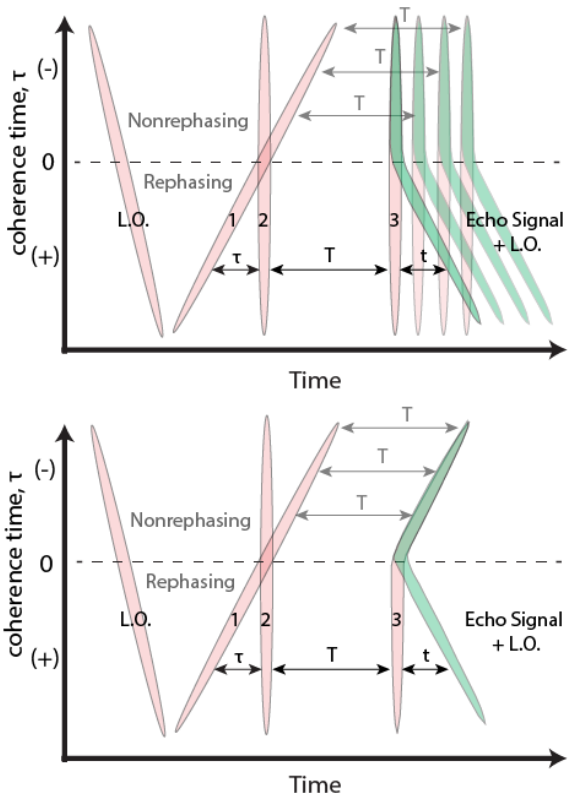

Figure 2.12: Pulse sequence in GRAPES with fine waiting time sampling that allows for the restructuring of the data to recover nonrephasing spectra.

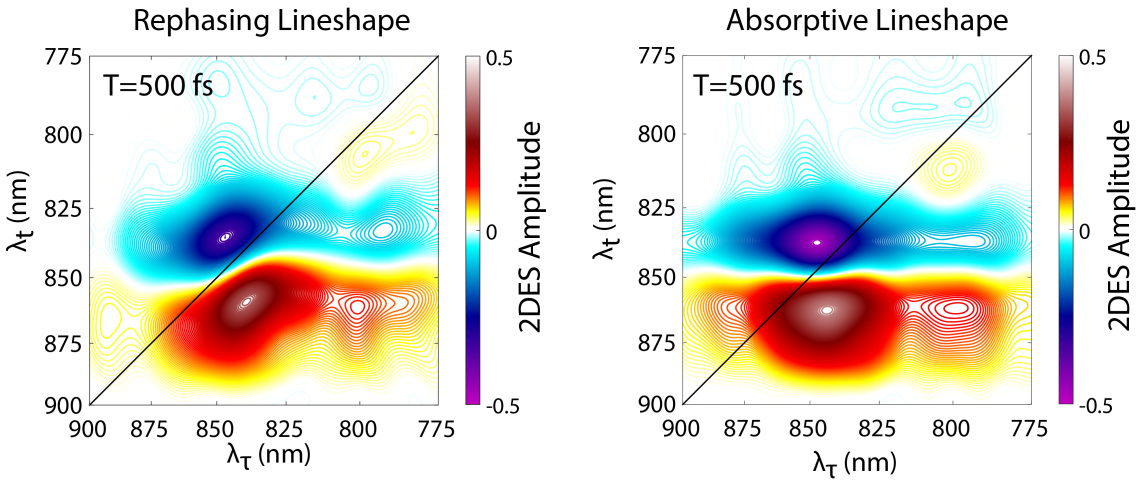

Figure 2.13: Rephasing spectrum on the left versus the absorptive spectrum on the right for LH2 only containing cells at a waiting time of 500 fs

REFERENCES

[1] G. S. Schlau-Cohen, A. Ishizaki, and G. R. Fleming. Two-dimensional electronic spectroscopy and photosynthesis: Fundamentals and applications to photosynthetic light-harvesting. *Chemical Physics*, 386(1-3):1–22, 2011.

[2] P. Hamm and M. T. Zanni. *Concepts and methods of 2D infrared spectroscopy.* Cambridge University Press, New York, New York, 2011.

[3] R. Berera, R. van Grondelle, and J. T. M. Kennis. Ultrafast transient absorption spectroscopy: principles and application to photosynthetic systems. *Photosynthesis Research*, 101(1-3):105–118, 2009.

[4] R. G. Norrish and B. A. Thrush. Flash photolysis and kinetic spectroscopy. *Quarterly Reviews of the Chemical Society*, 10(2):149–168, 1956.

[5] D. Polli, L. Luer, and G. Cerullo. High-time-resolution pump-probe system with broadband detection for the study of time-domain vibrational dynamics. *Review of Scientific Instruments*, 78(10):103108, 2007.

[6] R. E. Blankenship. *Molecular mechanisms of photosynthesis.* Blackwell Science, Malden, Massachusetts, 2002.

[7] J. Deisenhofer and J. R. Norris. *The Photosynthetic reaction centery.* Academic Press, San Diego, California, 1993.

[8] J. R. Lakowicz. *Principles of fluorescence spectroscopy.* Springer, New York, New York, 2006.

[9] T. Brixner, T. Mancal, I. V. Stiopkin, and G. R. Fleming. Phase-stabilized two-dimensional electronic spectroscopy. *Journal of Chemical Physics*, 121(9):4221–4236, 2004.

[10] J. A. Myers, K. L. Lewis, P. F. Tekavec, and J. P. Ogilvie. Two-color two-dimensional fourier transform electronic spectroscopy with a pulse-shaper. *Optics Express*, 16(22):17420–17428, 2008.

[11] E. Hecht. *Optics*. Addison-Wesley, Reading, Massachusetts, 2002.

[12] E. Harel, P. D. Long, and G. S. Engel. Single-shot gradient-assisted photon echo electronic spectroscopy. *Journal of Physical Chemistry A*, 115(16):3787–3796, 2011.

[13] E. Harel, P. D. Long, and G. S. Engel. Single-shot ultrabroadband two-dimensional electronic spectroscopy of the light-harvesting complex lh2. *Optics Letters*, 36(9):1665–1667, 2011.

CHAPTER 3

RHODOBACTER SPHAEROIDES PROTOCOLS

Rhodobacter sphaeroides has been a model organism for many decades. This thesis does not claim to have developed any of the techniques in this chapter. Instead, this chapter is intended to summarize the protocols currently used in the lab from the many protocols that can be found in the literature. The protocols described here are largely adapted from references [1, 2].

3.1 Growth Of *Rhodobacter sphaeroides*

As discussed in chapter 1 *Rba. sphaeroides* is metabolically diverse and can be grown photoautotrophically and heterotrophically. The growth conditions used in the two cases are quite different.

3.1.1 Photoautotrophic Growth Protocol

Rba. sphaeroides grows more slowly under photosynthetic conditions taking about 1-1.5 weeks to mature from seeding, but if contamination is a problem these growth conditions are very robust without the use of any antibiotic. There are few other organisms in the lab that can co-culture with *Rba. sphaeroides* in minimal media and anaeroibic conditions. For each liter of media, add 20 mL of solutions, A, B, and C and 10 mL of solution D to 1 gram of casamino acids see Tabels 3.1.1, 3.1.1, 3.1.1 and 3.1.1. Adjust the pH to 6.85-6.90 using HCl or NaOH before autoclaving.

Solution A: 1M Potassium Phosphate Buffer	
Reagent	amount
K_2HPO_4	115 g/L
KH_2PO_4	44.9 g/L

Table 3.1: Adjust pH to 6.8 using KOH or H_3PO_4

Solution B: 1M Ammonium Succinate	
Reagent	amount
Succinic acid	118 g/L
NH_4OH	155 mL/L

Table 3.2: Add 118 grams of succinic acid to 500 mL of water. Slowly add around 155 mL of NH_4OH to adjust the pH to 6.8. Fill to a final volume of 1 liter.

Solution C: Concentrated Base	
Reagent	amount
EDTA-Na_2	11.16 g/L
$(NH_4)_6Mo_7O_24$-$4H_2O$	9.3 mg/L
$FeSO_4$-$7H_2O$	100 mg/L
Metals 44 solution	50 mL/L
$MgSO_4$	14.5 g/L ($MgSO_4$-$7H_2O$= 26.9 g/L)
$CaCl_2$	2.5 g/L
Metals 44	
$FeSO_4$-$7H_2O$	5 g/L
EDTA-Na_2	6.5 g/L
$ZnSO_4$-$7H_2O$	10.9 g/L
$MnCl_2$-$4H_2O$	1.3 g/L
$CuSO_4$-$5H_2O$	0.392 g/L
$CoCl_2$-$6H_2O$	0.2 g/L
H_3BO_3	0.114 g/L

Table 3.3: Add the following in order to 750 mL of H_2O. When everything is dissolved (can take awhile, some heat can help too) adjust pH with NH_4OH the add H_2O to a final volume of 1 liter.

Solution D: 500 mL of Vitamin Stock	
Reagent	amount
Nicotinic acid	3.25 g/500 mL
Thiamine	1.25 g/500 mL
Biotin	0.05 g/500 mL

Table 3.4: Add the following in order to 500 mL of H_2O

Making anaerobic cultures is relatively straight forward but you have to remember that your final culture flask must be filled to the brim to make it anaerobic. Make sure you autoclave enough media and a glass stopper for the top of the bottle to accomplish this. **Do not autoclave the media with the glass stopper on**, instead wrap the stopper in aluminum foil and use a foam stopper covered with aluminum foil for the media. When seeding a new culture make sure to work in a biohood and follow all standard cell culture protocols. Typically, when seeding or scaling up, I use a ratio of around 1:10 culture to new media.

Once the cultures are sealed they should be taken out of the biohood and placed in the dark over night. This allows the cells to use up all disolved oxygen and become truly anaerobic, though in my experience this has not made a significant difference. After a day of being in the dark, the cultures are placed in the incubator under incandescent light. These cells, unlike plant, algae, and cyanobacteria, grow much better under incandescents because their light harvesting machinery absorbs light predominantly in the NIR region of the solar spectrum and fluorescent lights do not produce light in this region. Make sure that the temperature of the incubator stays near 32° Celsius. Temperature control is currently maintained with a simple reptile enclosure temperature controller. Figure 3.1 shows cells being cultured photosynthetically. The incorporation of the carotenoid spheroidene under anaerobic growth conditions gives the cells the brown color.

Figure 3.1: Anaerobic cultures of *Rba. sphaeroides*

3.1.2 Heterotrophic Growth Protocol

While *Rba. sphaeroides* grows faster under heterotrophic conditions than photosynthetic conditions, it grows slower than competing bacteria making contamination a real problem under heterotrophic conditions. The "wild type" strain currently cultured in the lab has antibiotic resistance to tetracycline and I strongly suggest using this antibiotic for best growth. Any mutant strains lacking the RC must also be grown under these conditions. [3] The cultures reach the stationary phase after three days at which point they should be split or scaled up. The procedure for splitting and seeding is very similar to the case of anaerobic photosynthetic growth provided above. One difference is the flasks will only be about 1/2 full and should be capped with a foam stopper and covered in aluminum foil. The bacteria are semi-aerobic under these conditions and will incorporate the carotenoid spheroidenone, giving them a purple hue, see Figure 3.2. Additionally, the cells should be placed into a dark incubator at 32° Celsius.

Figure 3.2: Heterotrophic pilot cultures of *Rba. sphaeroides* on the left and large 1.5 Liter cultures on the right. The lights for illumination are only for the photographs and are off during growth.

1 L of Media for Heterotrophic Growth	
Solution	Amount
Distilled H_2O	885 mL/L
10% $(NH_4)_2$ SO_4	10 mL
10 % DL-Malic Acid, pH 6.8	40 mL
Super Salts	50 mL
0.64M Potassium Phosphate Buffer, pH 6.8	15 mL
Bacto Yeast Extract	2 g
Bacto Peptone	2 g

Table 3.5: Add the following together and be sure to pH at the end. The media should be pH 6.8.

500 mL of Antibiotic Stock Solution	
Reagent	Amount
Tetracycline (store in freezer)	625 mg/500 mL
Ethyl Alcohol 180 proof	400 mL/500 mL
Distilled H_2O	100 mL/500 mL

Table 3.6: Antibiotic stock

10% $(NH_4)_2$ SO_4 pH 6.8 using HCl	
Reagent	Amount
$(NH_4)_2$ SO_4	100 g/L

Table 3.7: Ammonium sulfate solution

10 % DL-Malic Acid, pH 6.8	
Reagent	Amount
DL-Malic acid	100 g/L
NaOH	60 g/L

Table 3.8: Malic acid solution

Super Salts	
Reagent	Amount
Distilled H_2O	980 mL/L
EDTA Na_2	0.4 g/L
$MgSO_4$-$7H_2O$	4 g/L
$CaCl_2$-$2H_2O$	1.5 g/L
Trace Elements	20 mL/L
$FeSO_4$-$7H_2O$	0.24 g/L
Thiamine	20 mg/L

Table 3.9: Super salt solution. I have found that over the course of several months bacteria can culture in the super salts. Dispose of the solution every 2 months to avoid growth problems.

250 mL of Trace Elements	
Reagent	Amount
$MnSO_4$-H_2O	397 mg/250 mL
H_3BO_3	700 mg/250 mL
$Cu(NO_3)_2$-$2H_2O$	8.7 mg/250 mL
$ZnSO_4$-$7H_2O$	60 mg/250 mL
Na_2MoO_4-$2H_2O$	187 mg/250 mL

Table 3.10: Trace elements

0.64M Potassium Phosphate Buffer	
Reagent	amount
K_2HPO_4	73.6 g/L
KH_2PO_4	28.8 g/L

Table 3.11: Potassium Phosphate Buffer

3.2 Isolation Of RC And LH2

The isolation procedure for LH2 and Histidine tagged RC's is quite laborious and takes around 3-4 days from start to finish.

3.2.1 Day 1

1. Start with roughly 30 grams of pelleted cells either photosynthetically or heterotrophically grown
2. Homogenize in 100 ml of 10 mM Tris PH 7.5
3. Sonicate on ice while stirring
    - Sonicator settings: 30% duty cycle output control level 8
    - When sonicating immerse tip until it is just above the stir bar
    - Sonicate for 5 min, wait for 5 min
    - Sonicate for 5 min, wait for 5 min
    - Sonicate for 5 min, wait for 5 min
4. French press at 14000 PSI three times through for highest yield
5. Centrifuge at 12000 rpm using JA 30.STI at 4 degrees Celsius for 20 min to remove unlysed cell debris
6. Ultra centrifuge the supernatant for 90 min at 50000 rpm at 4 degrees Celsius
7. Make sucrose gradient 0.6-1.2 molar with .04% LDAO+ 10mM Tris pH 7.5
    - 100 ml at 0.6 M and 100 ml of 1.2 M
    - 0.6 M 20.52 grams of sucrose for 100 ml
    - 1.2 M 41.04 grams of sucrose for 100 ml

8. Save the pellet from ultra centrifuge. The supernatant is largely cytochromes

9. At this point, the supernatent contains all the light harvesting machinery either as chromatophores for wild type cells or as membrane fragments for mutant cells. These can be used for analysis if the native membrane enviornment is desired.

10. Solubilize the pellet to OD 50 cm^{-1} at 850 nm in 0.6% LDAO+10 mM tris for 30 min, see Figure 3.3.

11. Spin at 12000 RPM JA 30.STI for 10 min. Save the supernatant

12. Load supernatant onto sucrose gradient

13. Run sucrose overnight at 50000 RPM 4 degrees

14. Make dialysis buffer

    - 10 mMolar tris
    - 0.06 % LDAO
    - pH 7.5

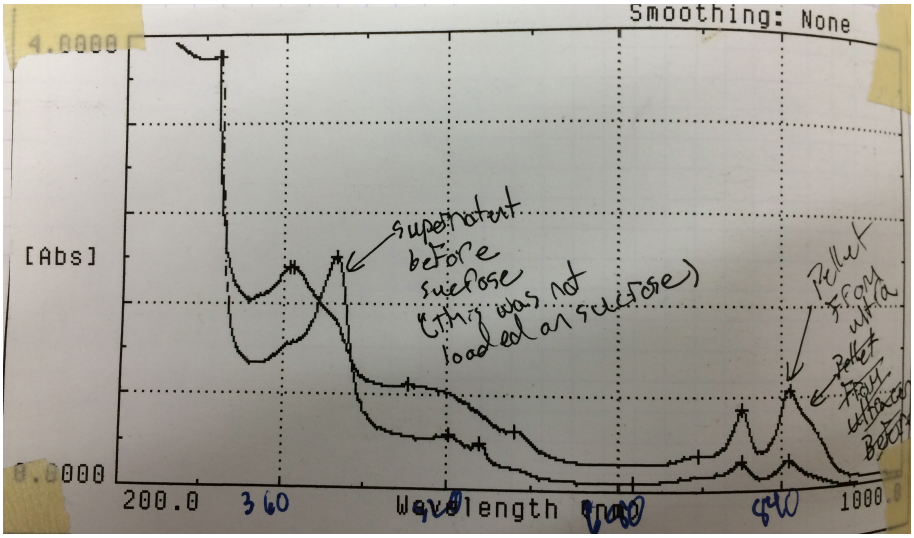

Figure 3.3: Lysed cell pellet and supernatant after ultracentrifugation for 90 minutes

3.2.2 Day 2

1. The sucrose gradient may not yield distinct bands, but it does eliminate significant amounts of protein in the pellet at the bottom. There should be a broad dark band still suspended in the sucrose gradient. This should contain the majority of the light harvesting machinery.

2. Load dialysis bags with dark band. LH2 is 43 KDa, the dialysis bags can have a molecular weight cutoff of 10-30 kDa. Suspend tubing over night.

3. Make flow through buffers

    - 5 mM imidazole 10 mM Tris 0.06% LDAO ph 7.5
    - 250 mM imidazole 10 mM Tris 0.06% LDAO ph 7.5

4. If isolating RCs, prepare the Ni-NTA columns according to manufactures protocols [4]

3.2.3 Day 3

1. Remove the dialysis bags and add LDAO to achieve concentration of 0.1 % LDAO. Stir for 20 minutes. This will help break up the LH1, LH2, and RC before running Ni-NTA.

2. Run the sample through the nickel-NTA column. The LH2 and fragmented LH1 should flow through, see Figure 3.4 and the RC should leave a dark band at the top.

3. Flow the 5 mM imidazole 10 mM Tris 0.06% LDAO solution through the column until the flow through is colorless by UV-VIS including 280 nm peak. Be sure to collect the fractions containing LH2

4. Elute the RC fraction off of the column using the 250 mM imidazole 10 mM Tris 0.06% buffer.

5. Perform buffer exchange on the roughly 5 ml of RC that you acquire from the column using centrifuge filter units with molecular cutoff of 10-30 kDa. End with 20 mM Tris .06% LDAO pH 7.5

6. Make buffers for anion exchange column

   - 200ml 20 mM Tris 0.1% LDAO pH 8.0 (equilibration buffer)
   - 200 ml 20 mM Tris 0.1% LDAO 160 mM NaCl pH 8.0 (wash buffer)
   - 500 ml 20mM Tris 0.1% LDAO 320 mM NaCl pH 8.0 (elution buffer)

7. Concentrate the LH2 fractions using a centrifuge filter (MW cutoff 10-30 kDa) to a volume of 10-15 mL and buffer exchange either through dialysis or during concentration into 20 mM Tris 0.06% LDAO pH 7.5

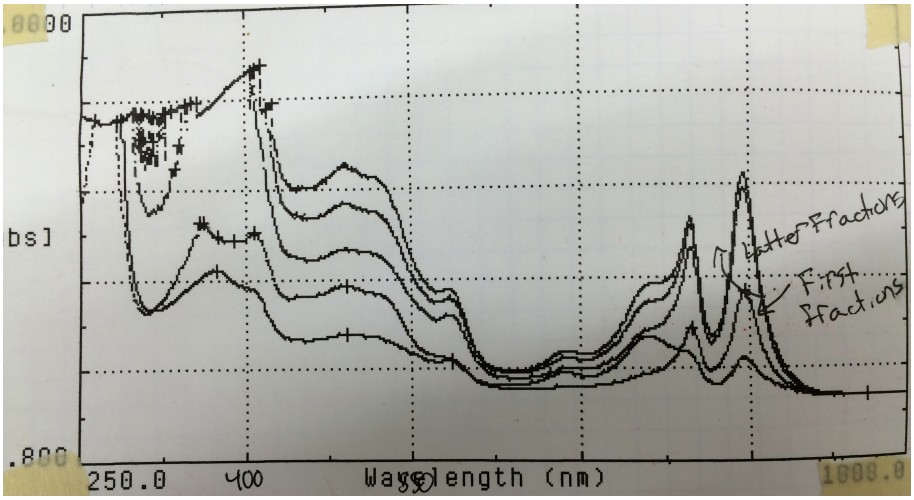

Figure 3.4: Fractions from Ni-NTA column before the elution buffer is flowed. These fractions contain LH2 as well as LH1 that falls apart after the removal of the RC

3.2.4 Day 4

1. Pack anion exchange column (DEAE Sephacel column) using a few PSI of air pressure

2. Flow equilibration buffer (20 mM Tris 0.1% LDAO pH 8.0) through the column using a few PSI of pressure from peristaltic pump

3. Load the column with the LH2 fractions by pipetting it on top of the column. Be careful not to disturb the top of the column.

4. Wash the column with 20 mM Tris 0.1% LDAO 160 mM NaCl pH 8.0. Check the fractions. When they are running clean i.e. no peak at 280 nm switch to elution buffer. You may have to make more than 200 mL of the wash buffer.

5. Flow the elution buffer and collect LH2 fractions

6. Using centrifuge filters or dialysis, buffer exchange LH2 into 20 mM Tris 0.06% LDAO pH 7.5, see Figure 3.5

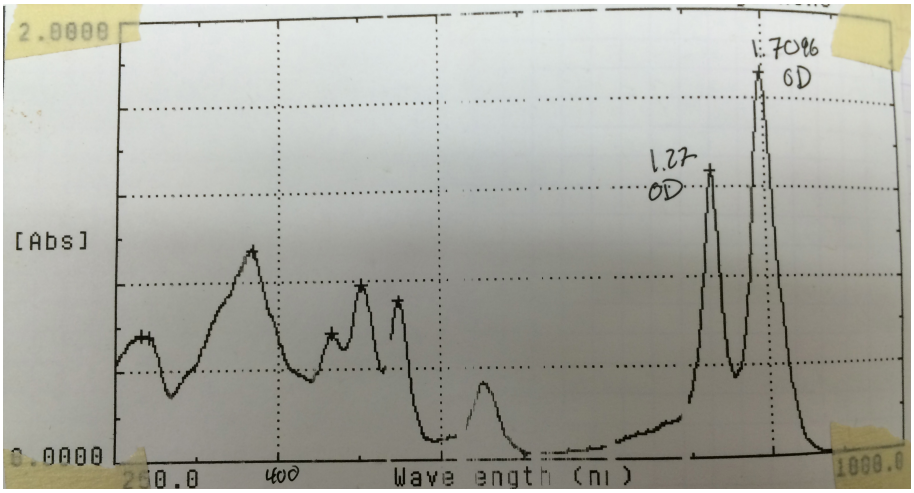

Figure 3.5: Final absorption spectrum in 1 mm achieved after isolation for LH2. Note the ratio between 280 nm and 850 nm. This ratio of ≈1:2 is indicative that the LH2 is quite pure.

REFERENCES

[1] L. N. Liu, T. J. Aartsma, and R. N. Frese. Dimers of light-harvesting complex 2 from *Rhodobacter sphaeroides* characterized in reconstituted 2d crystals with atomic force microscopy. *The FEBS Journal*, 275(12):3157–3166, 2008.

[2] H. A. Frank, B. W. Chadwick, J. Jin Oh, D. Gust, T. A. Moore, P. A. Liddell, A. L. Moore, L. R. Makings, and R. J. Cogdell. Triplet-triplet energy transfer in b800850 light-harvesting complexes of photosynthetic bacteria and synthetic carotenoporphyrin molecules investigated by electron spin resonance. *Biochimica et Biophysica Acta (BBA) - Bioenergetics*, 892(3):253–263, 1987.

[3] D. J. Mothersole, P. J. Jackson, C. Vasilev, J. D. Tucker, A. A. Brindley, M. J. Dickman, and C. N. Hunter. Pucc and lhaa direct efficient assembly of the light-harvesting complexes in *Rhodobacter sphaeroides*. *Molecular Microbiology*, 99(2):307–327, 2016.

[4] J. O. Goldsmith and S. G. Boxer. Rapid isolation of bacterial photosynthetic reaction centers with an engineered poly-histidine tag. *Biochimica et Biophysica Acta (BBA)-Bioenergetics*, 1276(3):171–175, 1996.

CHAPTER 4

ENERGY TRANSFER OBSERVED IN LIVE CELLS USING TWO-DIMENSIONAL ELECTRONIC SPECTROSCOPY

4.1 UVAGRAPES

*Dynamics in photosynthesis span many orders of magnitude in time and space. Following absorption of a photon, energy migrates from the antennae complex, where the majority of solar photons are absorbed, to the reaction center, where charge separation ensues. These initial energy transfer events occur on time scales ranging from hundreds of femtoseconds to several picoseconds and occur with near unity quantum efficiency under low light conditions. [2–4] Two-dimensional electronic spectroscopy (2DES) can interrogate these initial events in photosynthesis. 2DES produces two-dimensional maps that reveal energetic coupling, energy transfer, and solute-solvent dynamics on a femtosecond time scale. [5–7] A 2DES experiment demands stability in the laser and laboratory conditions throughout data acquisition, which often takes minutes or hours to complete. 2DES also requires a robust sample that produces little scatter and will not degrade during the course of the experiment. However, recently developed lock-in detection schemes for 2DES have mitigated the low scatter restriction. [8, 9] Previous work has produced the gradient assisted photon echo spectroscopy (GRAPES) apparatus, which is capable of taking a complete 2DES spectrum on each shot of the laser. [10–12] Coupling this capability with advances in CMOS detectors, we have built an Ultrafast Video Acquisition GRAPES (UVA GRAPES) apparatus, which can acquire 8192 complete 2DES spectra in less than 3.5 s, limited only by the 5 kHz repetition rate of the laser. By filtering in conjugate Fourier domains and fast background subtraction, the technique is relatively immune to scattered light. Thus, UVA GRAPES reduces two experimental difficulties associated with 2DES: long-term stability and signal contamination from scattered photons. These advances allow us to conduct a 2DES experiment in living cells of the purple

∗. This work is adapted from reference [1]

bacterium *Rhodobacter sphaeroides*. We use this technique to monitor energy transfer in the light harvesting complex two (LH2), the dominant antennae complex of *Rhodobacter sphaeroides*. [13, 14]

The GRAPES apparatus encodes the coherence time delay spatially across the sample allowing acquisition of an entire two- dimensional spectrum in a single laser pulse, as shown in Figure 4.1. [10–12] Here, we present 2DES experiments, each completed in 3.27 s, with 8192 waiting times spaced roughly 0.2 fs apart. The GRAPE apparatus only permits the collection of rephasing or non-rephasing signals for a specific scan and all data collected for this manuscript was rephasing only. [15] The supercontinuum pulse used in these experiments was produced via filament generation in argon gas. The output of a 5 kHz Coherent Legend Elite USP regenerative amplifier seeded by a Coherent Micra Ti:Sapphire oscillator was focused into 2.25 m of argon gas held at 1.3 atm. Filament generation produced a broad spectrum (center = 808 nm fwhm = 70 nm). The resulting spectrum was compressed using Multiphoton Intrapulse Interference Phase Scan (MIIPS) compressor (Biophotonics Solutions Inc.) to ≈15 fs fwhm. [16] Spectra were acquired using a Phantom Miro M high-speed camera from Vision Research. The camera trigger was synchronized to the output of the regenerative amplifier firing at 5 kHz. An optical chopper modulates pulses 1 and 2 at 2.5 kHz resulting in every other laser shot producing either a complete two-dimensional spectrum or a reference spectrum consisting of only pulses 3 and the LO. The reference spectrum is subtracted from the previous complete two-dimensional spectrum, which was acquired only 200 μs earlier. This fast scatter subtraction minimizes the effect of slow drift in the laser system and improves scatter subtraction capabilities from the conventional scatter subtraction methods outlined by Brixner et al. [17] The waiting time was scanned by moving a motorized linear stage (Aerotech ANT130-L) throughout the duration of the experiment at a constant velocity of 75 μm/s. Incident pulse powers for pulses 1-3 were 420 nJ each at the sample. These powers are significantly higher than conventional 2DES experiments because we encode the coherence time delay by focusing to a line (≈6 mm by

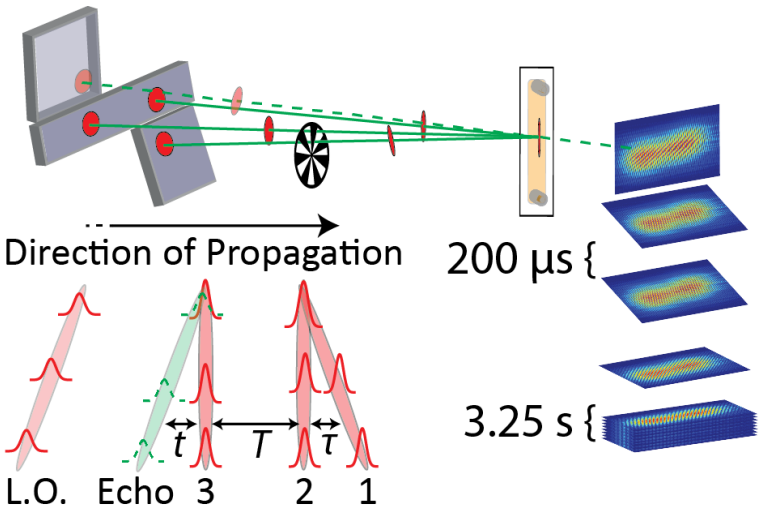

Figure 4.1: The GRAPE mirror produces a slight angle between the wavefronts of pulses 1 and 2 at the focus, which spatially encodes the coherence time and allows for single shot acquisition of a 2DES spectrum. The inset shows the pulse train at the sample. In the extension of GRAPE presented here, pulses 1 and 2 are modulated together at 2.5 kHz to produce either a reference composed of pulse 3 and the LO only or a complete 2DES interferogram on every other laser shot. Each laser shot is acquired separately at 5 kHz, while the waiting time stage is moving at a constant velocity of 75 μm/s. The data is saved to the camera flash and is capable of storing 8192 distinct spectra.

$\approx$60 μm) at the sample rather than to a spot. The resulting energy flux of 115 μJ/cm^2 per pulse is comparable to numerous studies that report similar dynamics and 2DES spectra for LH2; effects due to multiexciton generation in a single complex are negligible in this regime. [12, 18–20] The LO was attenuated by an additional 3 orders of magnitude relative to the other pulses.

4.2 Sample Preparation

LH2 complexes were purified from cultures of *Rhodobacter sphaeroides* in the manner outlined by Frank et al. [21] Samples adequate for spectroscopic analysis required two sequential filtrations through a DEAE-Sephacel column followed by elutions with 500-600 mM NaCl. Samples were subsequently concentrated to produce an optical density of roughly 0.3 at 800 nm in a quartz flow cell (Starna Cells, Inc.) with a path length of 200 μm. Whole cells were

first spun down and frozen and then thawed and diluted with their growth media to achieve an optical density also of 0.3 at 800 nm in the same 200 μm fused quartz flow cell.

4.3 Scatter Removal

The possible contributions from scattered light in the phase matched direction as outlined by Brixner et al. are shown in Figure 4.2*A*. [17] We isolate the scatter contributions from the signal first by subtraction of the pulse 3 and LO only reference spectrum. Once the reference scatter is removed, we filter in the t domain and the ω_T domain to remove the remaining scatter. The *in vivo* data for all the waiting and rephasing times at τ equal to zero after subtraction of the reference are shown in Figure 4.2*B*. The signal, the interferogram between the signal field and the LO field spaced $\approx$3 ps apart, is well separated in the t domain from the scattered light produced by pulses spaced 0 to $\approx$1 ps apart. Specifically, the interferograms from pulses 1 and 2 interfering with the signal, pulses 1 and 2 interfering with pulse 3, pulses 1 and 2 interfering with themselves, and the signal homodyne are separable from the signal in this domain. [17] However, the signal cannot be isolated from the scatter contributions arising from pulses 1 and 2 interfering with the LO or pulses 1 and 2 interfering with the signal in the t domain. To filter these scatter contributions from the signal we transform to the ω_T domain shown in Figure 4.2*C*. These scatter contributions can be removed in this domain because the time difference between interfering electric fields is dependent on T. As the T delay stage moves, pulses 1 and 2 are delayed relative to pulse 3 and the LO. This change in delay causes the electric fields of pulses 1 and 2 to evolve phase relative to pulse 3 and the LO at the optical frequency. This phase evolution is not present in the signal or the scatter contributions, and any dynamics in the signal as a function of T are of a time scale significantly longer than the optical period, 2.67 fs for 800 nm light. The signal is therefore low-pass filtered in the ω_T domain at 1/2 the optical frequency and then apodized with a Welch window. Filtering in ω_T would not be practical without the single shot capability of UVA GRAPES as T must be finely sampled to obtain sufficient separation of the optical

frequency from the homodyne signals leading to prohibitively long experiments. Waiting times can be recovered for samples with sufficient scatter from pulses 1 and 2, which was the case for all samples discussed in this publication. The waiting time difference between spectra is determined by the slope of $(E_1 + E_2)E_{LO}*$ at τ equal to zero, shown in Figure 4.2*B*. The zero of waiting time is located at the intercept of $(E_1 + E_2)E_{LO}$ and the $E_s{E_{LO}}^*$ scatter. We found good agreement with the expected values of the waiting time given the stage settings. Recovered timing data gave a waiting time spacing of 0.198 ± 0.005 fs for a stage setting expected to yield 0.2 fs between spectra.

4.4 2DES Spectral Comparison

Two-dimensional spectra of isolated LH2 complexes (left) and whole cells (right) each at a waiting time of 200 fs are shown in Figure 4.4, and a larger sampling of 2D spectra from assorted waiting times are shown in Figures 4.5 and 4.6. The spectra are normalized to the maximum signal intensity of each experiment separately. The two spectra appear qualitatively very similar despite the fact that the whole cell sample produced significant scatter during acquisition (Supporting Information Figure 4.7). The two peaks along the diagonal indicate absorption by the B850 and B800 rings from left to right. The cross peaks indicate electronic coupling as well as energy transfer between the two rings in the case of the lower cross peak. The intensity of the B800 band is significantly greater than that of the B850 band, which is the opposite of what would be expected given the linear absorption spectra. This inflated B800 intensity arises from our excitation spectrum only exciting the blue edge of the B850 band while exciting the entirety of the B800 band.

Waiting time traces through the top diagonal (B800) peak for isolated LH2 and whole cells are shown in Figure 4.4. Energy transfer from B800 to B850 dominates the decay of the B800 diagonal peak and the lifetime corresponds to the energy transfer rate. The decays are analyzed starting at 70 fs to avoid the instrument response function, measured using a solvent blank to be ≈35 fs fwhm. The decay of isolated LH2 follows a monoexponential

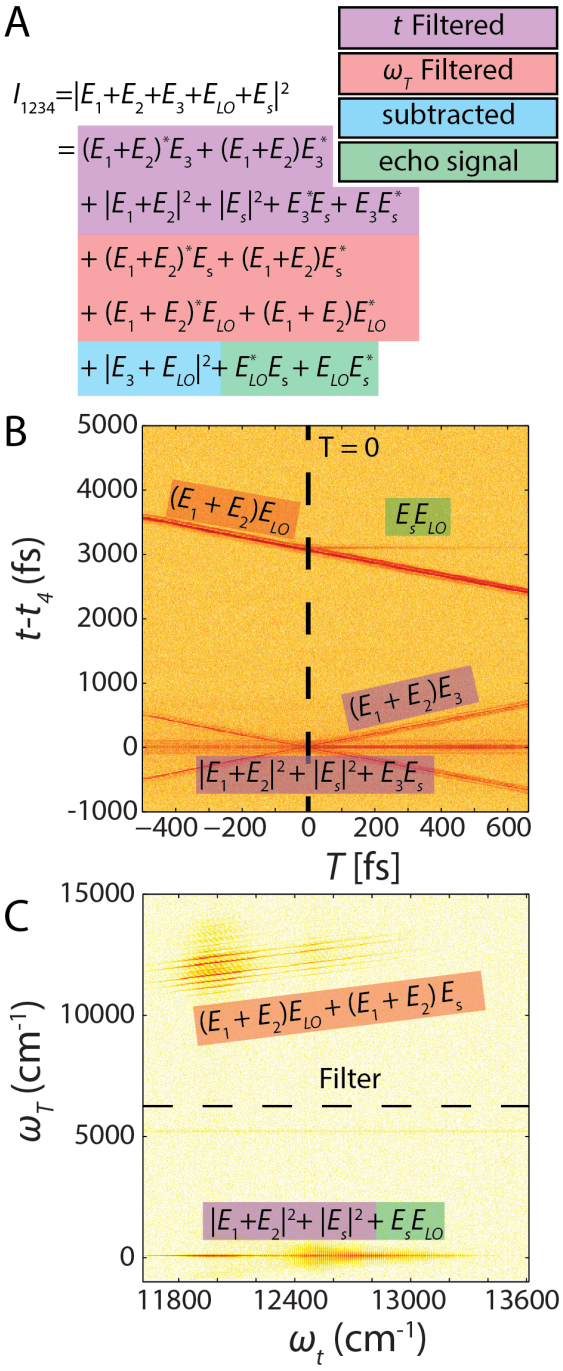

Figure 4.2: *(A)* Scatter contributions in addition to the desired signal recorded on the camera in a two-dimensional dimensional electronic spectroscopy experiment. The contributions are color coded to reveal how they are eliminated either by subtraction of a reference signal (blue) or filtering in the t (purple) or ω_T (red) domains. *(B)* A slice at coherence time equal to zero through a waiting time series of 2DES spectra of whole cells. The arcsinh of the data has been computed for display purposes. One can clearly see the separation of the signal from the $|E_1 + E_2|^2 + |E_s|^2 + E_3E_s + (E_1 + E_2)E_s + c.c.$ *(C)* Arcsinh of the data presented in panel B, except a Fourier transform and magnitude have been computed over both domains. The magnitude was computed for display purposes only and is not performed during actual data analysis. The $(E_1+E_2)E_LO + (E_1 + E_2)E_s$ scatter contributions oscillate at the optical frequency in T allowing their separation from the signal, which varies slowly in T.

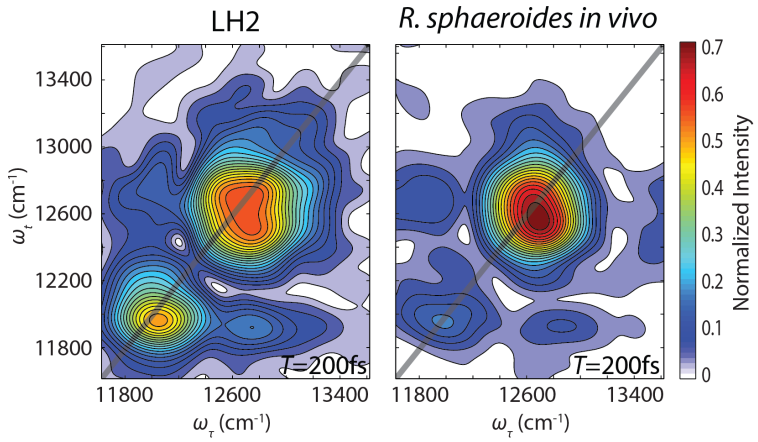

Figure 4.3: Two-dimensional spectra of isolated LH2 *(left)* and whole cells *(right)* both acquired at $T = 200$ fs. The qualitative similarity in structure and signal-to-noise ratio indicate the ability to remove scatter contributions from the highly scattering cells. The two diagonal peaks correspond to the B850 and B800 absorption features from left to right. The cross peaks indicate energetic coupling and transfer between B800 and B850

function with a lifetime of 661 ± 21 fs. The whole cell sample shows a similar decay with a lifetime of 692 ± 72 fs; however, the whole cell sample shows an additional rapid decay with a lifetime of 87 ± 58 fs. Complete regression parameters are shown in the Table 4.1. The fast decay is likely caused by internal relaxation within the B800 chromophores and may be related to the solvation environment within the lipid membrane. [22] We attribute the long lifetime component to energy transfer from B800 to B850. Our values agree well with known values for the energy transfer rate from B800-B850 of 700 fs. [3, 18, 19, 23–26] This result shows that energy transfer between rings in LH2 is either insensitive to the surrounding lipid environment or that detergent micelles provide a similar enough environment to the true lipid bilayer that effects on energy transfer between rings are negligible. We also observe significant reduction in intensity of the B850 diagonal peak in the whole cell data as shown in Table 4.2. We expect this peak to be diminished in whole cells due to energy transfer from B850 to LH1; however, we would not expect to observe such an effect within 200 fs. The diminished intensity could be indicative of additional intraband relaxation not present in the detergent micelles, but is likely due to slight errors in the sample positioning between samples. Additional studies are needed to produce definitive conclusions regarding the source

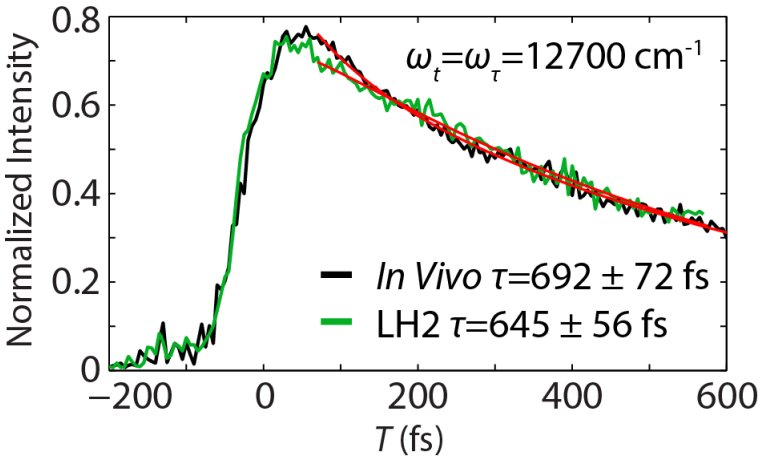

Figure 4.4: . Waiting time traces extracted from the diagonal peak at $\omega_\tau = \omega_t = 12700$ cm^{-1}. The traces were analyzed beginning at $T = 70$ fs to avoid artifacts from the instrument response function measured to be 35 fs. The *in vivo* trace follows a biexponential decay while the isolated LH2 follows a monoexponential decay. The large amplitude, long lifetime component of the regression parameters is given in the figure and agrees with previous measurements of energy transfer from B800 to B850, ≈700 fs.

of differences in the dynamics of the B850 diagonal peak.

UVA GRAPE permits 2DES experiments in whole cells of Rhodobacter sphaeroides and shows that energy transfer time scales for LH2 *in vivo* are comparable to time scales for isolated LH2. The technique is largely immune to scatter through fast scatter subtraction and filtering in the ω_T domain. Our approach reduces the demands on excitation spectral stability, environmental stability, and sample stability. The ability to achieve high signal-to-noise 2DES spectra of scattering samples such as whole cells in a matter of seconds will enable energy transfer events and photoprotection to be studied in real time and in living organisms.

4.A Fit Parameters And Supporting Figures

Sample	A_1	τ_1	A_2	τ_2
In Vivo	0.75 ±0.05	692 ±72 fs	0.2 ±0.06	87 ±58 fs
Isolated LH2	0.78 ±0.01	661 ±21 fs	N/A	N/A

Table 4.1: Regression parameters for decay of B800. The waiting time decay *in vivo* followed a bi-exponential function of the form $y = A_1 e^{-\frac{t}{t_1}} + A_2 e^{-\frac{t}{t_2}}$ while the isolated LH2 followed a mono-exponential function of the form $y = A_1 e^{-\frac{t}{t_1}}$

Sample	A_1	τ_1	C
In Vivo	0.12 ±0.01	323 ±106 fs	0.04 ±0.02
Isolated LH2	0.44 ±0.02	225 ±35 fs	0.22 ±0.02

Table 4.2: Regression parameters for decay of B850. The waiting time decays followed a mono-exponential function with a non-decaying component of the form $y = A_1 e^{-\frac{t}{t_1}} + C$

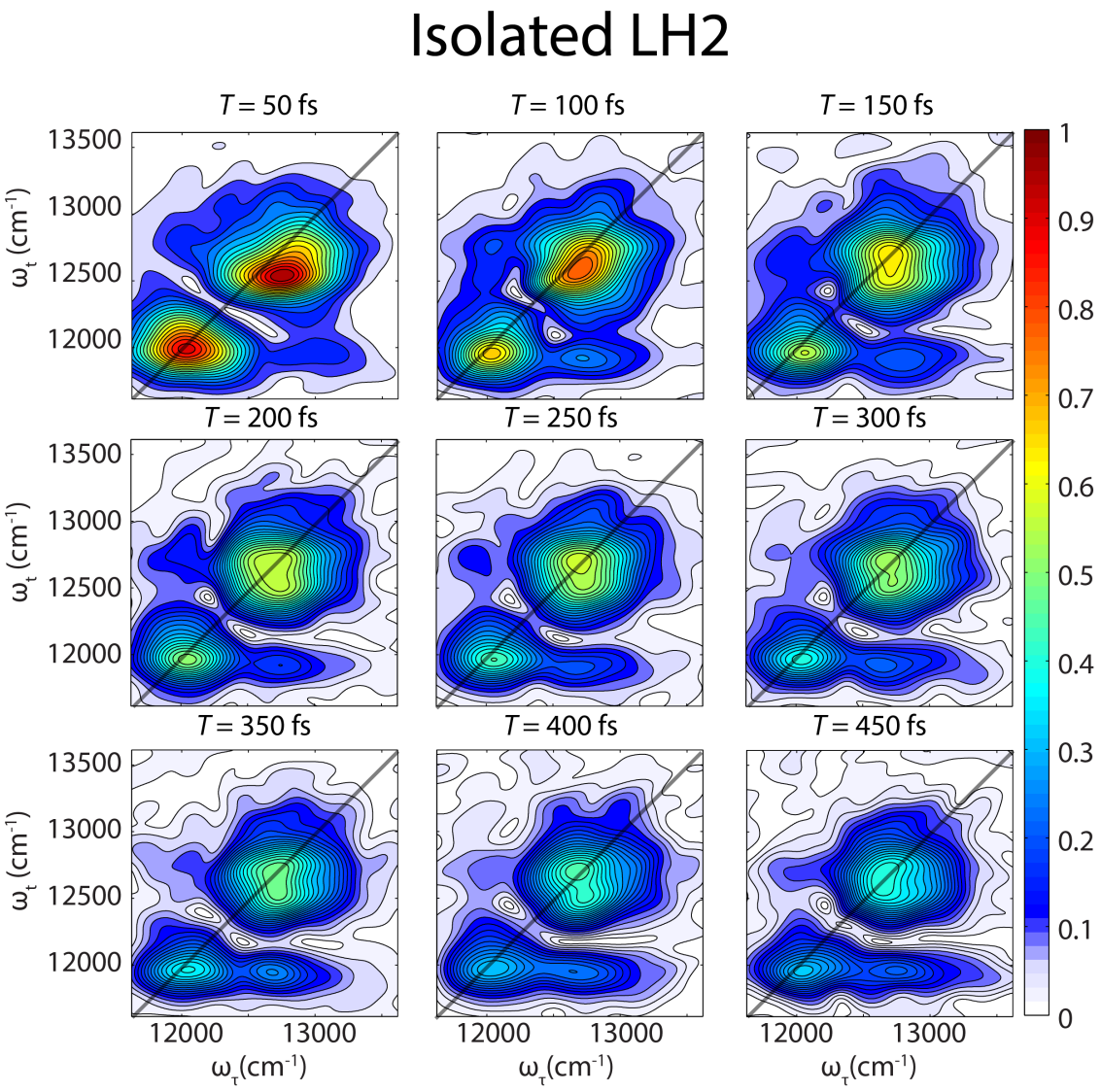

Figure 4.5: A waiting time series of 2D spectra acquired with UVA-GRAPES on isolated LH2 of *Rba. sphaeroides* in detergent micelles.

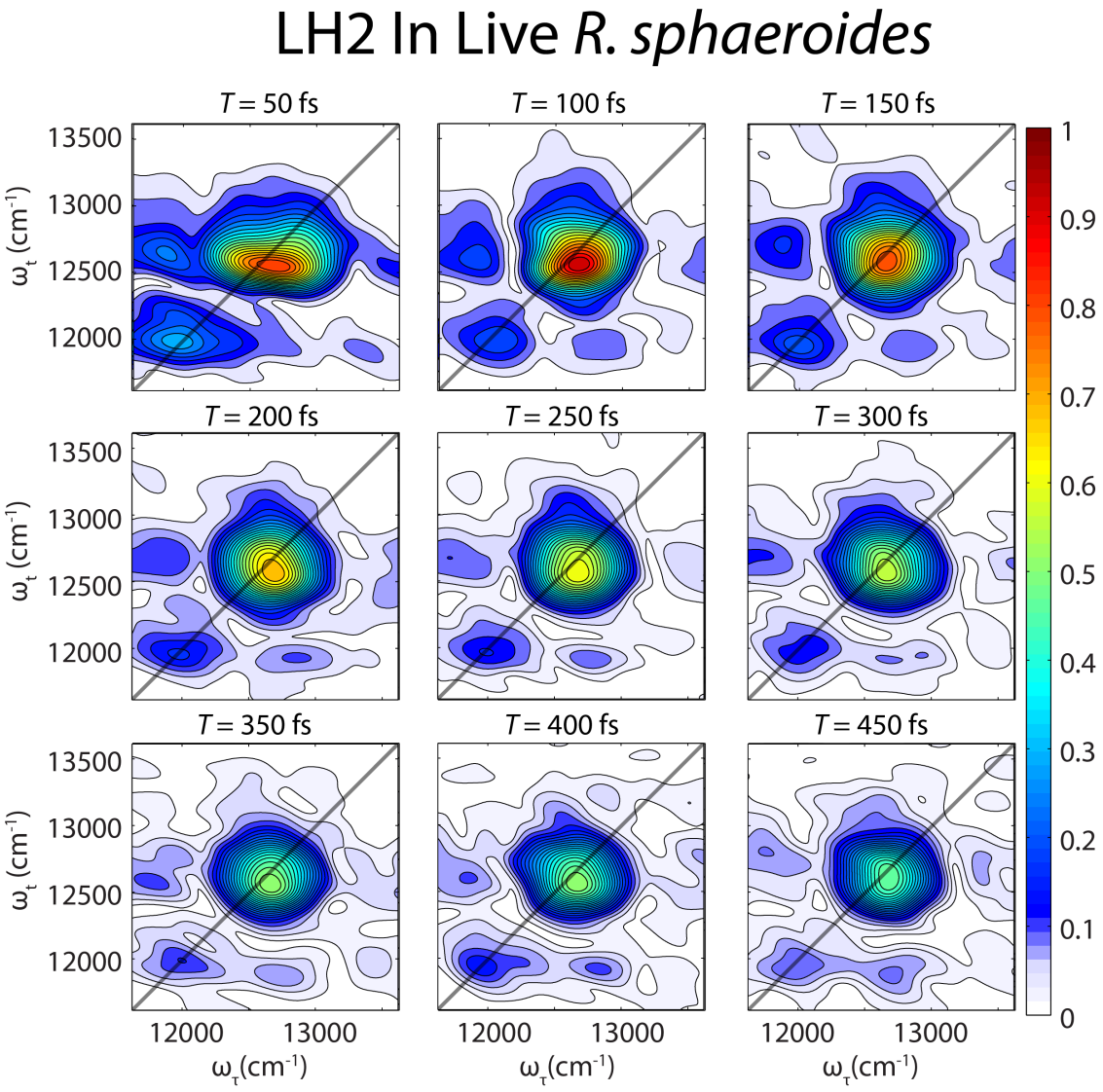

Figure 4.6: A waiting time series of 2D spectra acquired with UVA-GRAPES on live cells of *Rba. sphaeroides*

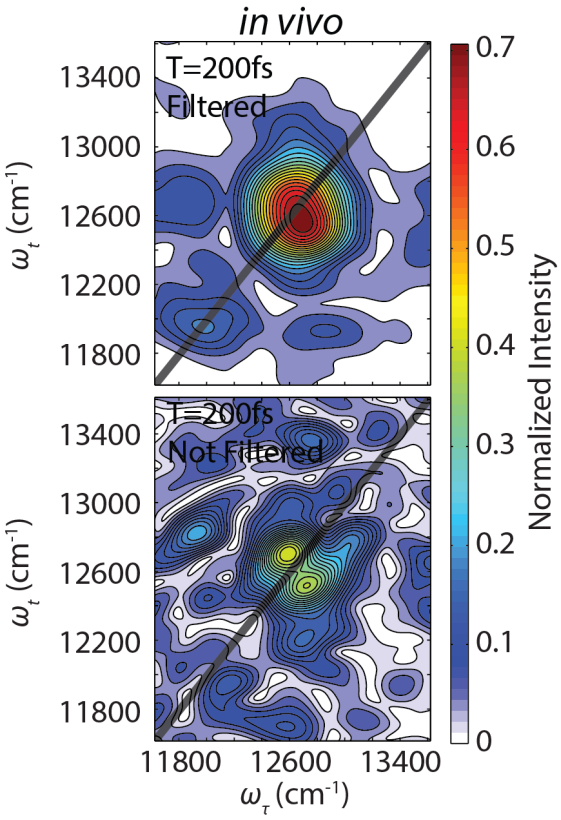

Figure 4.7: 2DES spectra of whole cells taken at T=200 fs with filtering in the ω_T domain (top) and without filtering in the ω_T domain (bottom). Without filtering the signal is dominated by scatter artifacts that obscure the nature of the energetic coupling within LH2

REFERENCES

[1] P. D. Dahlberg, A. F. Fidler, J. R. Caram, P. D. Long, and G. S. Engel. Energy transfer observed in live cells using two-dimensional electronic spectroscopy. *Journal Of Physical Chemistry Letters*, 4(21):3636–3640, 2013.

[2] R. E. Blankenship. *Molecular mechanisms of photosynthesis*. Blackwell Science, Malden, Massachusetts, 2002.

[3] G. R. Fleming and R. van Grondelle. Femtosecond spectroscopy of photosynthetic light-harvesting systems. *Current Opinion in Structural Biology*, 7(5):738–748, 1997.

[4] C. A. Wraight and R. K. Clayton. Absolute quantum efficiency of bacteriochlorophyll photooxidation in reaction centers of *Rhodopseudomonas spheroides*. *Biochimica Et Biophysica Acta*, 333(2):246–260, 1974.

[5] G. S. Schlau-Cohen, A. Ishizaki, and G. R. Fleming. Two-dimensional electronic spectroscopy and photosynthesis: Fundamentals and applications to photosynthetic light-harvesting. *Chemical Physics*, 386(1-3):1–22, 2011.

[6] M. Cho. Coherent two-dimensional optical spectroscopy. *Chemical Reviews*, 108(4):1331–1418, 2008.

[7] D. M. Jonas. Two-dimensional femtosecond spectroscopy. *Annual Review of Physical Chemistry*, 54:425–463, 2003.

[8] J. Dostal, T. Mancal, R. Augulis, F. Vacha, J. Psencik, and D. Zigmantas. Two-dimensional electronic spectroscopy reveals ultrafast energy diffusion in chlorosomes. *Journal of American Chemical Socieity*, 134(28):11611–11617, 2012.

[9] R. Augulis and D. Zigmantas. Two-dimensional electronic spectroscopy with double modulation lock-in detection: enhancement of sensitivity and noise resistance. *Optics Express*, 19(14):13126–13133, 2011.

[10] E. Harel, A. F. Fidler, and G. S. Engel. Real-time mapping of electronic structure with single-shot two-dimensional electronic spectroscopy. *Proceedings of the National Academy of Sciences*, 107(38):16444–16447, 2010.

[11] E. Harel, P. D. Long, and G. S. Engel. Single-shot gradient-assisted photon echo electronic spectroscopy. *Journal of Physical Chemistry A*, 115(16):3787–3796, 2011.

[12] E. Harel, P. D. Long, and G. S. Engel. Single-shot ultrabroadband two-dimensional electronic spectroscopy of the light-harvesting complex lh2. *Optics Letters*, 36(9):1665–1667, 2011.

[13] R. J. Cogdell, A. Gall, and Kohler J. The architecture and function of the light-harvesting apparatus of purple bacteria: from single molecules to in vivo membranes. *Quarterly Reviews of Biophysics*, 39(03):227–324, 2006.

[14] T. Pullerits, M. Chachisvilis, M. R. Jones, C. N. Hunter, and V. Sundström. Exciton dynamics in the light-harvesting complexes of *Rhodobacter sphaeroides*. *Chemical Physics Letters*, 224(3-4):355–365, 1994.

[15] V. P. Singh, A. F. Fidler, B. S. Rolczynski, and G. S. Engel. Independent phasing of rephasing and non-rephasing 2d electronic spectra. *Journal of Chemical Physics*, 139(8):084201, 2013.

[16] V. V. Lozovoy, I. Pastirk, and M. Dantus. Multiphoton intrapulse interference. iv.ultrashort laserpulse spectral phase characterization and compensation. *Optics Letters*, 29(7):775–777, 2004.

[17] T. Brixner, T. Mancal, I. V. Stiopkin, and G. R. Fleming. Phase-stabilized two-dimensional electronic spectroscopy. *Journal of Chemical Physics*, 121(9):4221–4236, 2004.

[18] T. H. Joo, Y. W. Jia, J. Y. Yu, D. M. Jonas, and G. R. Fleming. Dynamics in isolated bacterial light harvesting antenna (lh2) of *Rhodobacter sphaeroides* at room temperature. *Journal of Physical Chemistry*, 100(6):2399–2409, 1996.

[19] R. Monshouwer, I. O. Dezarate, F. van Mourik, and R. van Grondelle. Low-intensity pump-probe spectroscopy on the b800 to b850 transfer in the light-harvesting 2 complex of *Rhodobacter sphaeroides*. *Chemical Physics Letters*, 246(3):341–346, 1995.

[20] A. F. Fidler, V. P. Singh, P. D. Long, P. D. Dahlberg, and G. S. Engel. Timescales of coherent dynamics in the light harvesting complex 2 (lh2) of *Rhodobacter sphaeroides*. *Journal of Physical Chemistry Letters*, 4(9):1404–1409, 2013.

[21] H. A. Frank, B. W. Chadwick, J. Jin Oh, D. Gust, T. A. Moore, P. A. Liddell, A. L. Moore, L. R. Makings, and R. J. Cogdell. Triplet-triplet energy transfer in b800850 light-harvesting complexes of photosynthetic bacteria and synthetic carotenoporphyrin molecules investigated by electron spin resonance. *Biochimica et Biophysica Acta (BBA) - Bioenergetics*, 892(3):253–263, 1987.

[22] R. van Grondelle and V. I. Novoderezhkin. Energy transfer in photosynthesis: experimental insights and quantitative models. *Physical Chemistry Chemical Physics*, 8(7):793–807, 2006.

[23] J. L. Herek, N. J. Fraser, T. Pullerits, P. Martinsson, T. Polívka, H. Scheer, R. J. Cogdell, and V. Sundström. B800→b850 energy transfer mechanism in bacterial lh2 complexes investigated by b800 pigment exchange. *Biophysical Journal*, 78(5):2590–2596, 2000.

[24] S. Hess, E. Akesson, R. J. Cogdell, T. Pullerits, and V. Sundström. Energy transfer in spectrally inhomogeneous light-harvesting pigment-protein complexes of purple bacteria. *Biophysical Journal*, 69(6):2211–2225, 1995.

[25] H. van der Laan, Th Schmidt, R. W. Visschers, K. J. Visscher, R. van Grondelle, and S. Völker. Energy transfer in the b800850 antenna complex of purple bacteria *Rhodobacter sphaeroides*: A study by spectral hole-burning. *Chemical Physics Letters*, 170(2-3):231–238, 1990.

[26] J. K. Trautman, A. P. Shreve, C. A. Violette, H. A. Frank, T. G. Owens, and A. C. Albrecht. Femtosecond dynamics of energy transfer in b800-850 light-harvesting complexes of *Rhodobacter sphaeroides*. *Proceedings of the National Academy of Sciences*, 87(1):215–219, 1990.

CHAPTER 5

OBSERVATION OF VIBRONIC COHERENCES *IN VIVO*

5.1 Vibronic Coherence In Photosynthesis

*Photosynthetic organisms utilize large arrays of light harvesting antenna to maximize their absorption cross section and to improve their solar harvesting capabilities. The very first events after absorption of a photon in photosynthesis involve the transfer of excitation through these large antenna networks to the reaction center where the bound electron-hole pair is separated. The energy transfer process through the antenna network can be nearly 100% quantum efficient. [1, 2] Given the noisy, disordered environment within membranes of living cells, this high quantum efficiency is surprising. Many theories and experiments have been developed and performed to understand how photosynthetic organisms obtain such quantum-efficient energy transfer. [3, 4] In 2007, two-dimensional electronic spectroscopy (2DES) showed long-lived coherences within the Fenna-Mathews-Olson (FMO) complex, a pigment- protein complex found in green sulfur bacteria; these coherences were attributed to excited states. [5] Similar work was conducted on other pigment-protein complexes, finding that they too exhibited long-lived coherences. [6–11] Several models have suggested that long-lived electronic coherences may help to explain the high quantum efficiencies observed in photosynthesis. [3, 4, 12] Further experiments show that these long- lived coherences persist at room temperature, but with reduced lifetimes. [9, 13] Currently, the nature of these coherences, either vibrational, electronic, or some mixture of vibrational and electronic (vibronic), is under debate. [14–16] Recent works have classified many of these coherences as vibronic, with several recent publications providing experimental evidence for vibronic coherences as well as several models outlining their importance in energy transfer and possibly charge separation. [10, 11, 17–20] It is not the aim of this work to assign the nature of these coherences or to provide evidence for a given model, rather this work addresses the

∗. This work is adapted from reference [**?**]

debate of the biological significance of these coherences by observing them *in vivo*a necessary prerequisite for biological significance.

In the discussion surrounding the biological significance of these coherences, it has always been assumed that the coherences observed *in vitro* also occur *in vivo*. While it would be surprising if these coherences did not occur *in vivo*, it is necessary to confirm this assumption. Beyond mere existence, there are numerous reasons why the coherences may be different *in vivo* and *in vitro*. The coherences could differ in spectral location due to coupling to the intact photosynthetic unit as well as the presence of a large electric field ($\approx 10^7$ V/m) spanning the photosynthetic membrane known to cause electrochromic shifts. [21] The coherences may also differ in lifetime due to inhomogeneity of the biological environment. Coherence lifetime measurements in two-dimensional spectroscopy experiments are sensitive to both single molecule decoherence and ensemble dephasing. [22] Both effects are due to system-bath interactions and it is unclear how the complex and crowded environment *in vivo* will affect observed lifetimes in these complexes. Crowding *in vivo* could lead to increased disorder in system bath interactions and therefore shorter lifetimes, or it could be that the higher viscosity of the lipid bilayer reduces stochastic system-bath interactions and would increase coherent lifetimes *in vivo*. It is also possible that the environments are similar enough to produce no appreciable changes. These competing effects of unknown magnitudes make it difficult to predict changes to the lifetimes of coherences between *in vitro* and *in vivo* preparations, and it is also likely that different systems will respond differently to the changes in environment.

The technique of 2DES is well suited for the observation of coherences in biological systems. However, the interferometry can be frustrated by highly scattering systems like whole cells. Recent developments have focused both on overcoming scatter and decreasing experiment time to allow for triplicated results. [23–26] Here, we surmount both issuesintense scattered light and the quantification of errorsusing Ultrafast Video-Acquisition Gradient-Assisted Photon-Echo Spectroscopy (UVA-GRAPES) to observe coherences in the pigment-

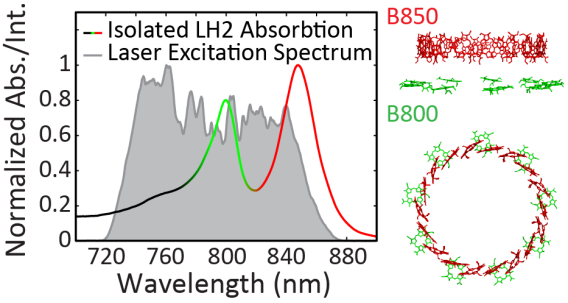

Figure 5.1: The normalized absorption spectrum of isolated LH2 is plotted (black-green-red solid gradient line) to emphasize the correlation between the absorption features and the two rings of bacteriochlorophyll *a* shown in profile to the right. The laser excitation spectra used to perform 2DES experiments are shown in shaded gray and are the result of filamentation in argon gas and pulse shaping with a spatial light modulator.

protein complex, light harvesting complex II (LH2), in whole cells of the purple bacterium, *Rhodobacter sphaeroides*.

Figure 5.1 shows the absorption spectra of LH2 alongside its crystal structure. Several energy transfer pathways exist connecting the higher-lying excited states in LH2 to the low-lying B850 states: B800 $\rightarrow$ B850* $\rightarrow$ B850, B800 $\rightarrow$ B850, and B850* $\rightarrow$ B800 $\rightarrow$ B850. [27, 28] The time scales for energy transfer along these pathways have been modeled using Redfield theory and experimentally determined. [29–34] Energy transfer from B800 to B850* occurs with a lifetime of $\approx$500-800 fs and from B800 to B850 with a lifetime of $\approx$700-1000 fs. The back-transfer from B850* to B800 is slower (>250 fs) than the transfer from B850* to B850 ($\approx$60-200 fs). Comparable rates of transfer from B800 to B850* and from B800 to B850 suggest that comparable amounts of energy are transferred over both pathways. Thus, the B850* states play an important role in directing energy flow from B800 to B850 and thereby to LH1. [27] Coherent mechanisms may play a crucial role in the energy transfer from B850* to B850. Room temperature coherences between states near 800 nm and states near 850 nm have been observed with a lifetime of $\approx$50-100 fs and were originally attributed to electronic coherence between B800 and B850 as well as to electronic coherence between B850* and B850. [28, 35] Recent work on a mutant strain of *Rba. sphaeroides* lacking the B800 chromophore ring found similar coherences, suggesting that the coherence is not between B800 and B850, but between B850* and B850. [36] Further analysis in the same work using a coherence specific pulse sequence was able to quantify the mixing of

vibrational and electronic states in the coherence between B850 and B850* and found a mixing angle of ≈15° and classified the coherence as vibronic. [36]

5.2 Searching For Coherences

Rhodobacter sphaeroides was cultured aerobically and in the dark at 28°C. Cells were cultured with either H_2O or 30% D_2O. The cells grown in 30% D_2O were intended to help isolate electronic or vibronic coherences from purely vibrational coherences, but room temperature dephasing rates prevent attribution of the coherences by isotopic substitution, instead the data show the reproducibility of the dynamics across samples. [37] Cells for analysis were centrifuged at 6000 rpm (rotor JLA 8.1) and diluted in a small volume of their supernatant, maintaining D_2O concentrations, to achieve an OD800 of ≈0.07 in a 200 μm quartz flow cell (Starna Cells, Inc.). For isolated LH2 experiments, the complex was isolated from the H_2O cells according to the protocol outlined in Chapter refBiologicalprotocol. The sample was buffer-exchanged into 20 mM Tris, 0.06% LDAO at pH 7.5, and concentrated to an OD800 of ≈0.22 in the flow cell described above. The absorption spectra of the cells grown in H_2O and D_2O as well as the isolated LH2 are shown in Figure 5.4 in the supplementary material with Raleigh scatter subtracted.

Figure 5.2 shows the absolute value 2DES rephasing spectra for isolated LH2, cells grown in the D_2O media, and cells grown in the H_2O media at a waiting time of 50 fs. Within error, the three plots are consistent and all three show dynamics and features similar to previously published LH2 spectra. The rephasing spectra can also be phased in a manner described by Singh et al. using separately acquired pump-probe data, see Figure 5.5 in the supplementary material. [38] In the phased data, we see ≈100 fs decay of the 850 nm diagonal region. This decay has previously been attributed to the stochastic hopping of the exciton around the B850 ring as well as relaxation to lower energy states within the B850 band. [27, 28, 39, 40] The growth of a cross peak between the B800 and B850 nm states is on the order of ≈700 fs, and a corresponding decay of the B800 states is also observed

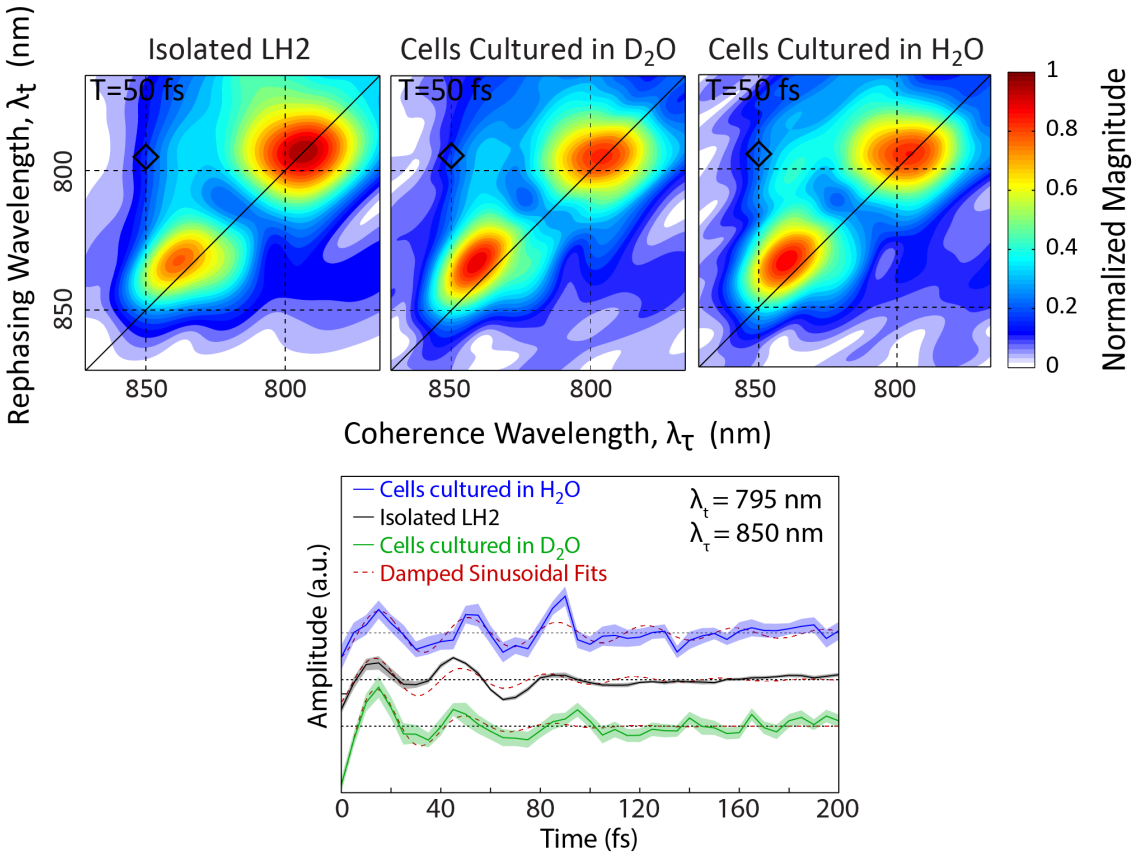

Figure 5.2: Absolute value 2DES spectra showing the magnitude of the rephasing signal at T = 50 fs are shown for isolated LH2 (left), cells grown in 30% D_2O media (middle), and cells grown in standard H_2O media (right). For each data set, the magnitude was separately normalized to the maximum of the entire waiting time scan. The black diamond indicates the location of the waiting time traces shown below. The shaded region in the waiting time traces is the standard error from 16 separate scans for each data set. The red lines indicate a fit to an exponentially damped sine wave

and is indicative of energy transfer from B800 to B850. In addition to these population transfers at early waiting times, coherent oscillations in the upper and lower cross-peaks in the region between the B800 and B850 bands are also observed. Due to slight uncertainties in the phasing and the possibility of improper phasing introducing modulations that can be mistaken as coherences, all analyses relating to the coherences are done with the absolute value data.

Subtracting a bi-exponential from the waiting time domain and Fourier transforming, the residual from 0 to 200 fs clarifies the coherent oscillations between B850* and B850 in

the absolute value data. The center of the B850* peak occurs at ≈795 nm, so a coherence between B850 and B850* should appear with a beat frequency of approximately 850 cm^{-1} (the energy difference between the center of the two states). Due to the short waiting time period considered, the frequency domain necessarily has widely spaced frequency points, with the two closest points being 830 and 1000 cm^{-1}. The bottom row of Figure 3 displays the separately normalized power spectra for each pixel at 830 cm^{-1}, the same analysis is shown in Figure 5.6 for a waiting time frequency of 1000 cm^{-1}. The full map of LH2 shows peaks located at both the upper and the lower cross peaks between B850 and B850*. The middle row of Figure 5.3 details the upper cross peak and highlights the similarity in location and intensity of oscillations between all three samples. The top row of Figure 5.3 depicts the phase of the oscillations over the same region as detailed in the middle row. All three samples show the same phase and phase roll across the diagonal of the peak. A phase roll is characteristic of both electronic and vibrational coherences. [41–43] Figure 5.2 shows waiting time traces from the upper cross peak for the isolated LH2, D_2O cells, and H_2O cells, again displaying similarities in phase and amplitude between samples. The 1σ standard error on the mean is displayed as the shaded region and is calculated from sixteen separate scans performed on each sample. The red lines indicate the fit of an exponentially damped sine wave to the residual of the bi-exponential fit. A regression was performed for each pixel within the region shown in the top and middle rows of Figure 5.3. The resulting lifetimes are provided in Figure 5.7 in the supplementary material and are found to be ≈40-60 fs, comparable to coherences previously observed in isolated LH2. This short lifetime is reflected in the waiting time frequency domain by a broad peak in the power spectra, which can be seen in Figure **??**. The distinct differences in amplitude and lifetime between the pure vibrational coherences and the vibronic coherence can be seen in Figures 5.9 and 5.10.

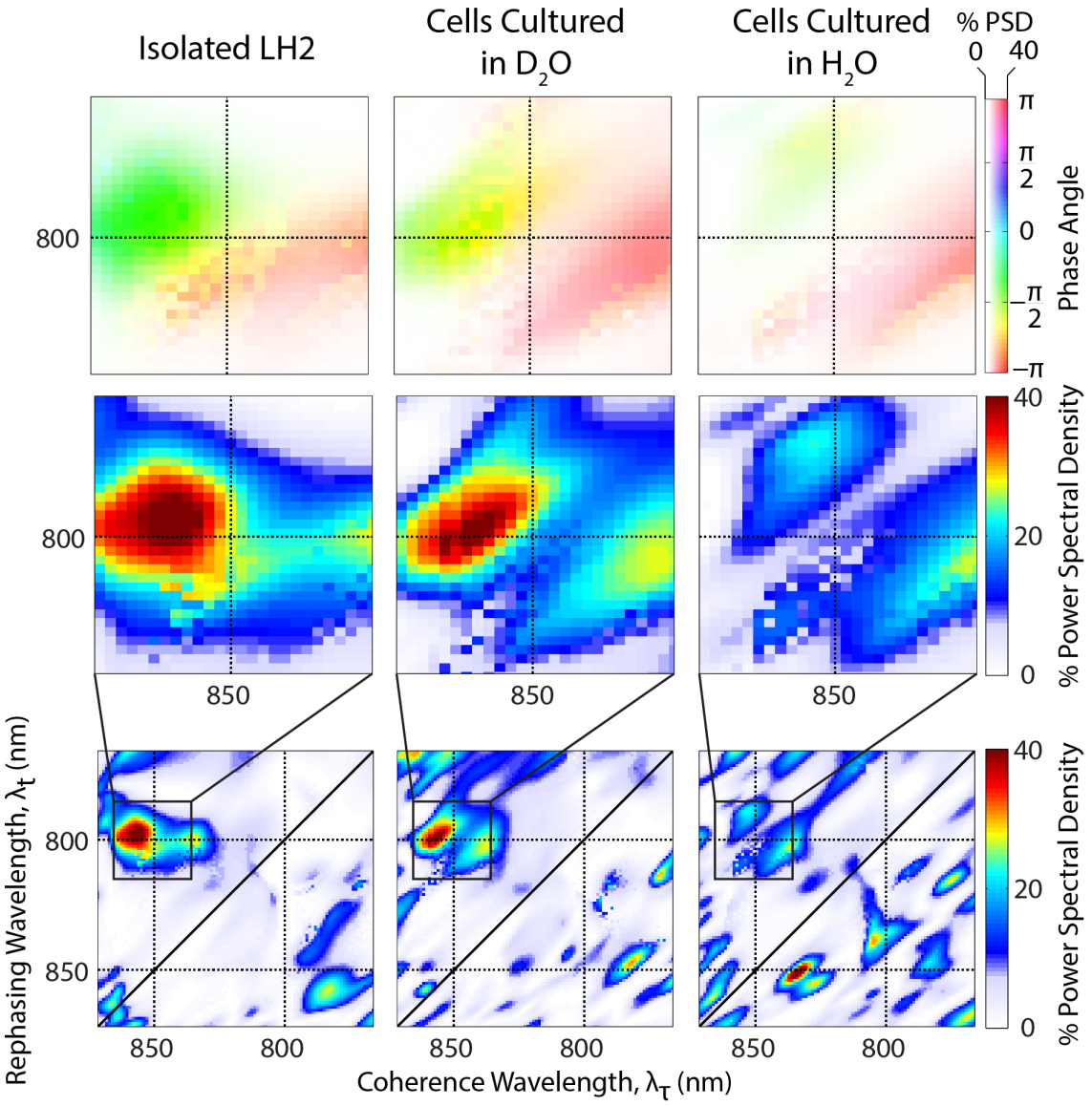

Figure 5.3: Bottom row: Power spectral density at 830 cm^{-1} represented as a percentage of the normalized, integrated power spectrum from the absolute value data. Middle row: Detail of the power spectrum at the 800-850 nm upper cross peak boxed in the bottom row. Top row: Phase of the 830 cm^{-1} oscillations over the same region, with the saturation determined by the power spectral density from the middle row.

5.3 Coherences Between B850 And B850* *In Vivo*

Vibronic coherence between B850 and B850*, while lasting less than 100 fs, has a similar lifetime to that of energy transfer between these states, ≈60-200 fs. The biological significance of this coherence is unclear, but due to the B850* states playing an intermediate role in the energy transfer pathways between the B800 and B850 states, [27] this coherence could play a significant role in improving the efficiency of solar light harvesting in *Rb. sphaeroides*. Observation of this coherence *in vivo* and its similarity to the coherence observed *in vitro* supports the assumption that coherences are robust to the environmental changes between the native photosynthetic membrane and detergent micelles. It is possible, however, that this coherence is uniquely similar *in vitro* and *in vivo because* the coherence is supported by different excited states on the same ring of chromophores, making it more robust to changes in environment. Future work must be done to determine whether other photosynthetic coherences exhibit this robustness and whether these coherences are dependent upon growth conditions. Further work will also examine whether coherences change in response to external stimuli such as intense light or the addition of oxygen, which are known to induce photoprotective mechanisms.

5.A Supporting Figures

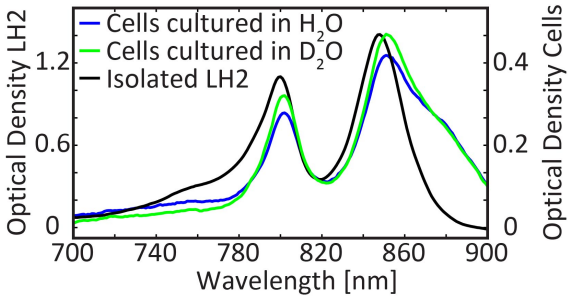

Figure 5.4: Linear absorption spectra taken in 1 mm path length cuvette of isolated LH2 (black) and *Rba. sphaeroides* grown in H_2O (blue) and 30% D_2O (green) growth media, showing peaks at 800 nm and 850 nm resulting from rings of bacteriochlorophyll *a* known as B800 and B850. The cellular samples are strongly affected by Raleigh scattering and so the optical density of the samples at 800 nm was lowered to attain an optimal signal-to-noise ratio. Raleigh scattering has been removed from the whole cells absorption spectra.

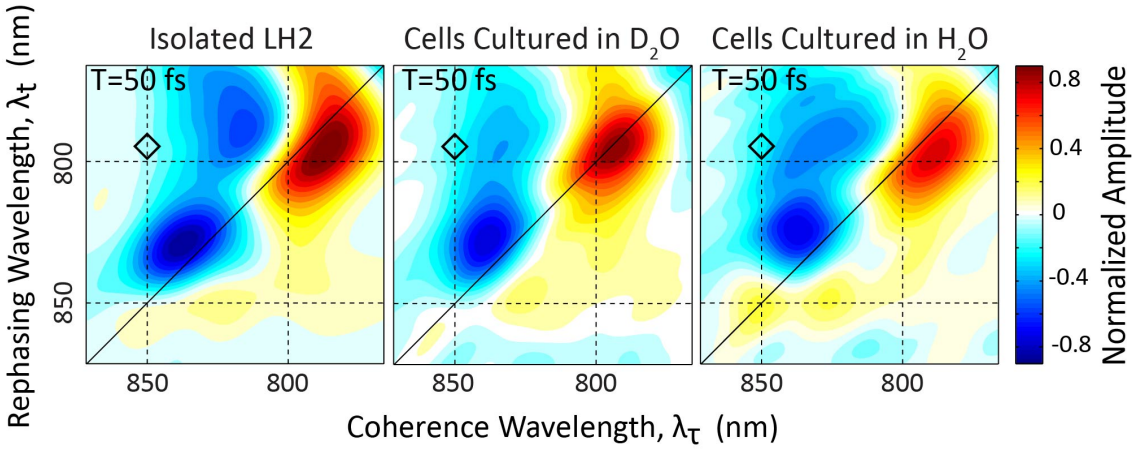

Figure 5.5: Phased 2D spectra at T=50 fs from isolated LH2 *(left)*, cells cultured in 30% D_2O *(middle)*, and cells cultured in H_2O *(right)*. Data was phased to separately acquired pump-probe spectra.

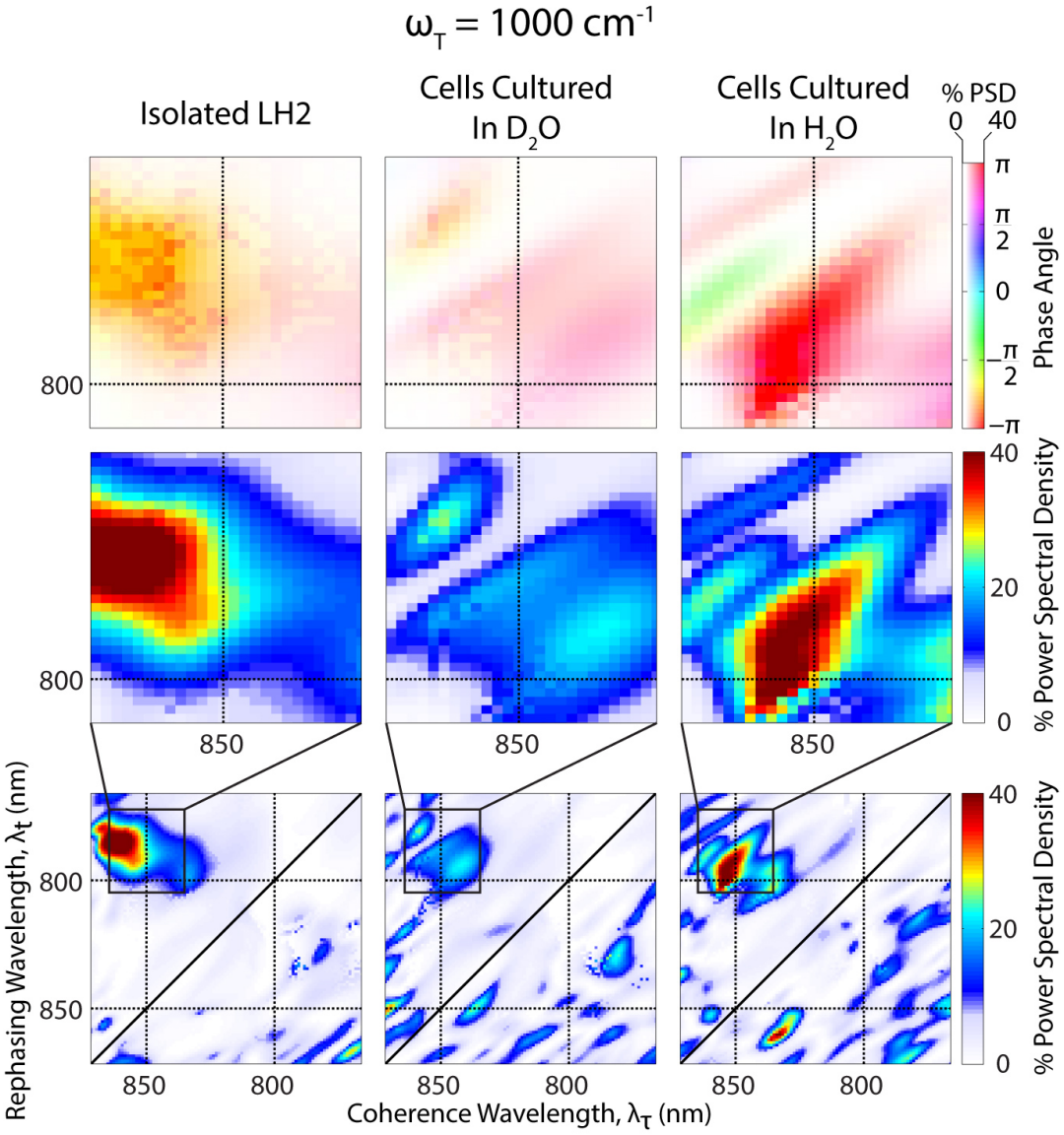

Figure 5.6: Bottom Row: Percentage of the total power spectrum at 1000 cm^{-1} from the absolute value data Middle Row: Detail of the power spectrum at the 800-850 nm upper cross-peak boxed in the bottom row. Top Row: Phase of the 1000 cm^{-1} oscillations over the same region, with the saturation determined by the percentage of the power spectrum from the middle row.

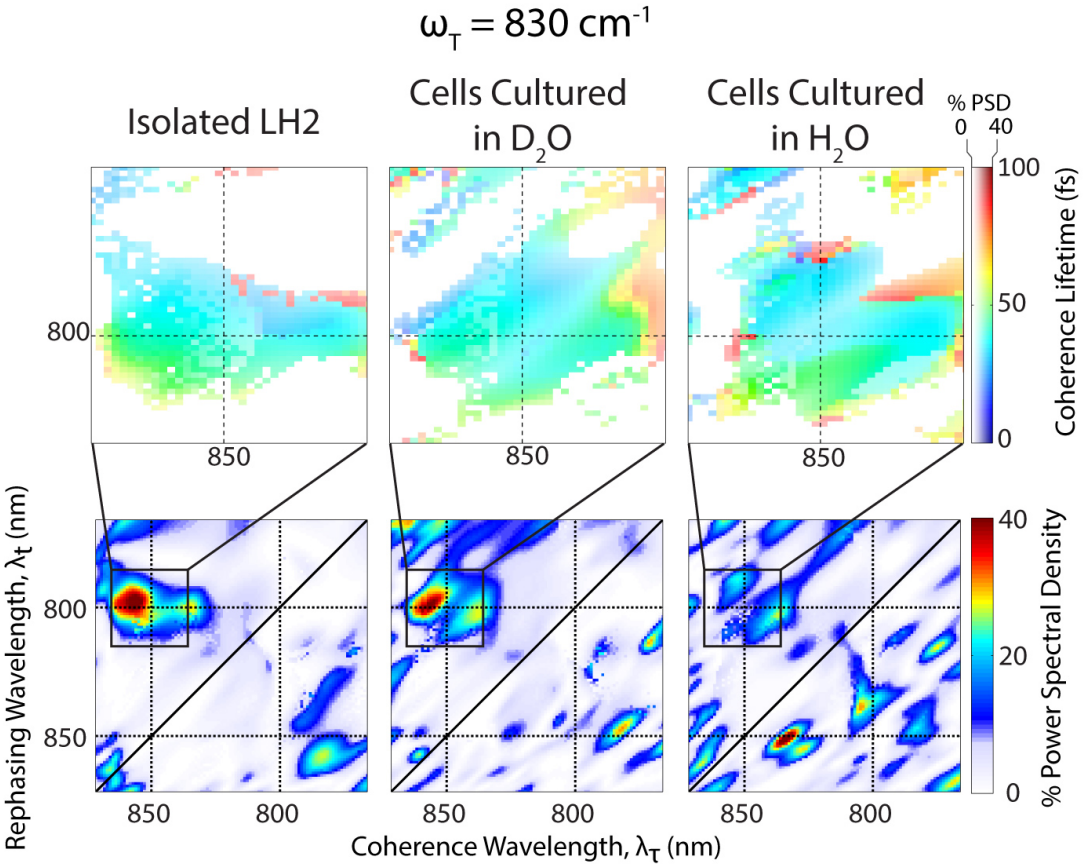

Figure 5.7: In analogy to Figure 5.3, lifetime maps of coherences at the 800-850 nm upper cross peak for isolated LH2 and *Rba. sphaeroides* grown in H_2O and 30% D_2O growth media. Lifetimes were calculated by fitting an exponentially decaying sinusoid to the residual of the bi-exponential fit to waiting time traces at each point, and are indicated by color. The saturation of each point is determined by the percentage of the total power spectrum at each point (see Figure 5.3).

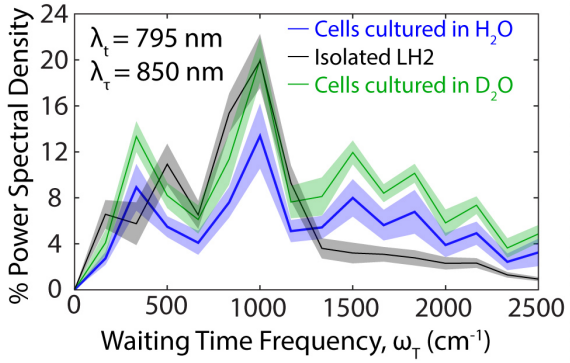

Figure 5.8: The complete power spectra of the waiting time traces shown in figure 4 normalized to the sum of the power spectra. The 1σ error on the mean was calculated from the average of 16 scans.

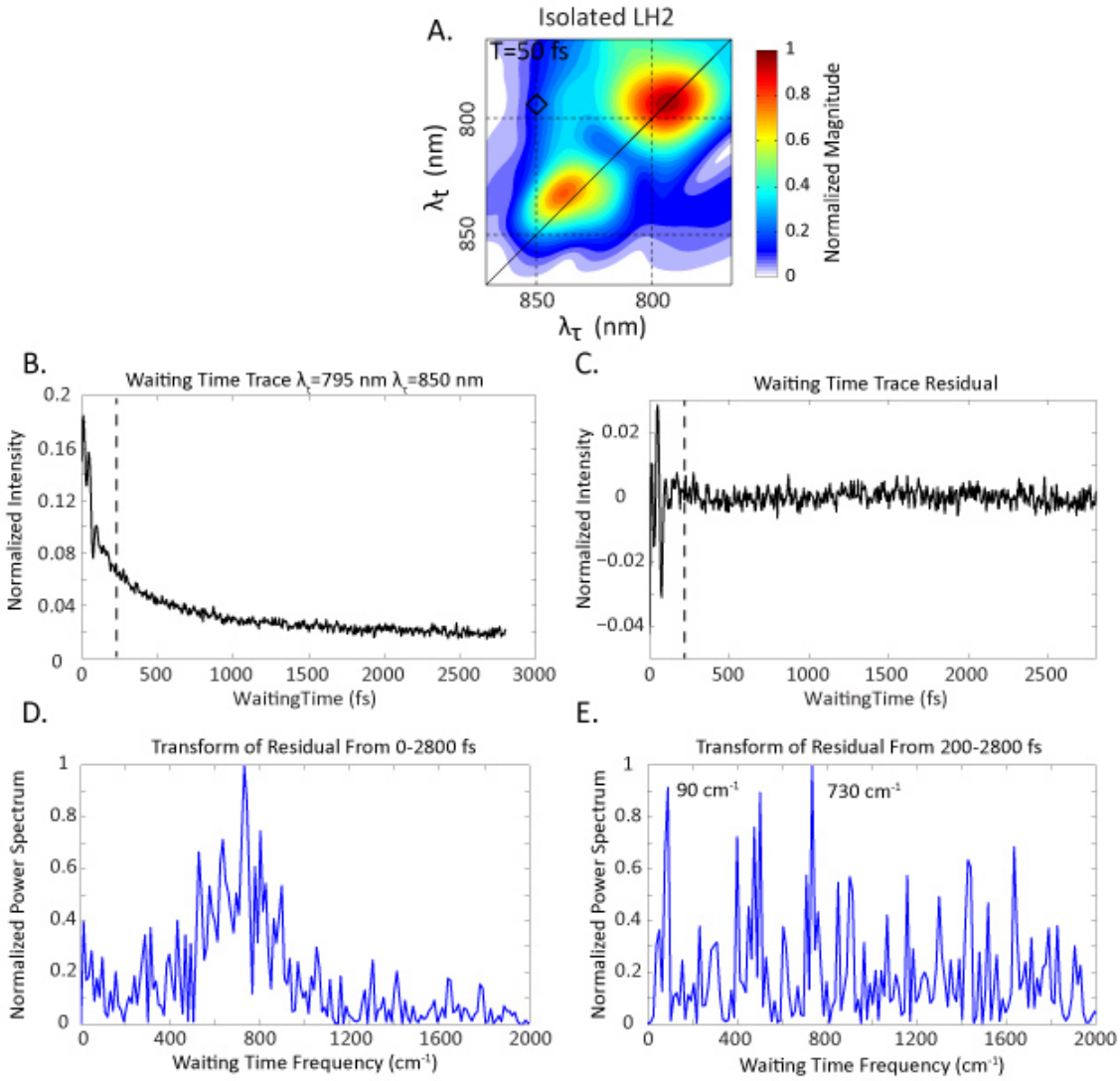

Figure 5.9: *A.* Black diamond indicates the location of waiting time trace analyzed (λ_t= 795 nm λ_τ=850 nm) in *B-E*. *B.* The raw waiting time from 0-2800 fs before the subtraction of a bi-exponential. *C.* Residual from the bi-exponential fit performed on panel *B*. *D.* The power spectrum of the residual from 0-2800 fs. The broad Lorentzian from ≈600-1000 cm^{-1} is attributed to the vibronic coherence at early waiting times. *E.* The power spectrum of the residual from 200-2800 fs. Despite the larger noise floor on the edge of the spectra the 2 largest features are at 90 cm^{-1}, and 730 cm^{-1}, which are all well known vibrational modes of bacteriochlorophyll *a*.

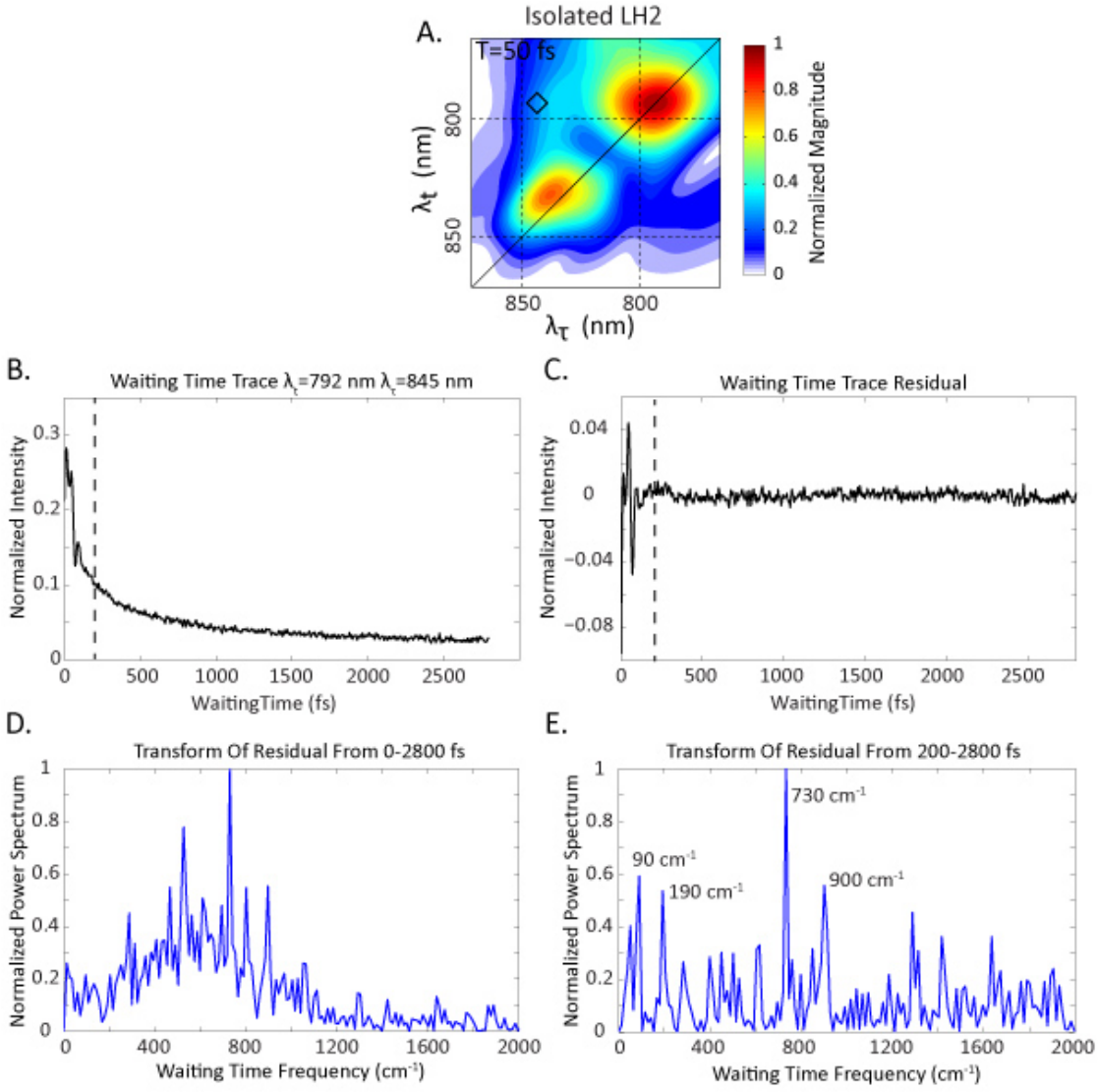

Figure 5.10: *A.* Black diamond indicates the location of waiting time trace analyzed (λ_t= 792 nm λ_τ=845 nm) in *B-E*. *B.* The raw waiting time from 0-2800 fs before the subtraction of a bi-exponential. *C.* Residual from the bi-exponential fit performed on panel *B*. *D.* The power spectrum of the residual from 0-2800 fs. The broad Lorentzian from ≈400-800 cm^{-1} is attributed to the vibronic coherence at early waiting times. *E.* The power spectrum of the residual from 200-2800 fs. The 4 largest features are at 90 cm^{-1}, 190 cm^{-1}, 730 cm^{-1}, and 900 cm^{-1}, which are all well known vibrational modes of bacteriochlorophyll *a*.

REFERENCES

[1] C. A. Wraight and R. K. Clayton. Absolute quantum efficiency of bacteriochlorophyll photooxidation in reaction centers of *Rhodopseudomonas spheroides*. *Biochimica Et Biophysica Acta*, 333(2):246–260, 1974.

[2] R. K. Chain and D. I. Arnon. Quantum efficiency of photosynthetic energy conversion. *Proceedings of the National Academy of Sciences*, 74(8):3377–3381, 1977.

[3] P. Rebentrost, M. Mohseni, I. Kassal, S. Lloyd, and A. Aspuru-Guzik. Environment-assisted quantum transport. *New Journal of Physics*, 11(3):033003, 2009.

[4] M. Mohseni, P. Rebentrost, S. Lloyd, and A. Aspuru-Guzik. Environment-assisted quantum walks in photosynthetic energy transfer. *Journal of Chemical Physics*, 129(17):174106, 2008.

[5] G. S. Engel, T. R. Calhoun, E. L. Read, T. K. Ahn, T. Mancal, Y. C. Cheng, R. E. Blankenship, and G. R. Fleming. Evidence for wavelike energy transfer through quantum coherence in photosynthetic systems. *Nature*, 446(7137):782–786, 2007.

[6] H. Lee, Y. C. Cheng, and G. R. Fleming. Coherence dynamics in photosynthesis: Protein protection of excitonic coherence. *Science*, 316(5830):1462–1465, 2007.

[7] G. S. Schlau-Cohen, A. Ishizaki, T. R. Calhoun, N. S. Ginsberg, M. Ballottari, R. Bassi, and G. R. Fleming. Elucidation of the timescales and origins of quantum electronic coherence in lhcii. *Nature Chemistry*, 4(5):389–395, 2012.

[8] G. S. Schlau-Cohen, E. De Re, R. J. Cogdell, and G. R. Fleming. Determination of excited-state energies and dynamics in the b band of the bacterial reaction center with 2d electronic spectroscopy. *Journal of Physical Chemistry Letters*, 3(17):2487–2492, 2012.

[9] E. Collini, C. Y. Wong, K. E. Wilk, P. M. Curmi, P. Brumer, and G. D. Scholes. Coherently wired light-harvesting in photosynthetic marine algae at ambient temperature. *Nature*, 463(7281):644–647, 2010.

[10] F. D. Fuller, J. Pan, A. Gelzinis, V. Butkus, S. S. Senlik, D. E. Wilcox, C. F. Yocum, L. Valkunas, D. Abramavicius, and J. P. Ogilvie. Vibronic coherence in oxygenic photosynthesis. *Nature Chemistry*, 6(8):706–711, 2014.

[11] E. Romero, R. Augulis, V. I. Novoderezhkin, M. Ferretti, J. Thieme, D. Zigmantas, and R. van Grondelle. Quantum coherence in photosynthesis for efficient solar-energy conversion. *Nature Physics*, 10(9):677–683, 2014.

[12] A. Ishizaki and G. R. Fleming. Theoretical examination of quantum coherence in a photosynthetic system at physiological temperature. *Proceedings of the National Academy of Sciences*, 106(41):17255–17260, 2009.

[13] G. Panitchayangkoon, D. Hayes, K. A. Fransted, J. R. Caram, E. Harel, J. Wen, and G. S. Blankenship, R. E. Engel. Long-lived quantum coherence in photosynthetic complexes at physiological temperature. *Proceedings of the National Academy of Sciences*, 107(29):12766–12770, 2010.

[14] V. Tiwari, W. K. Peters, and D. M. Jonas. Electronic resonance with anticorrelated pigment vibrations drives photosynthetic energy transfer outside the adiabatic framework. *Proceedings of the National Academy of Sciences*, 110(4):1203–1208, 2013.

[15] K. A. Fransted, J. R. Caram, D. Hayes, and G. S. Engel. Two-dimensional electronic spectroscopy of bacteriochlorophyll *a* in solution: Elucidating the coherence dynamics of the fenna-matthews-olson complex using its chromophore as a control. *Journal of Chemical Physics*, 137(12):125101, 2012.

[16] N. Christensson, F. Milota, J. Hauer, J. Sperling, O. Bixner, A. Nemeth, and H. F. Kauffmann. High frequency vibrational modulations in two-dimensional electronic spec-

tra and their resemblance to electronic coherence signatures. *Journal of Physical Chemistry B*, 115(18):5383–5391, 2011.

[17] J. M. Womick and A. M. Moran. Vibronic enhancement of exciton sizes and energy transport in photosynthetic complexes. *Journal of Physical Chemistry B*, 115(6):1347–1356, 2011.

[18] A. Chenu and G. D. Scholes. Coherence in energy transfer and photosynthesis. *Annual Review of Physical Chemistry*, 66:69–96, 2015.

[19] V. Tiwari, W. K. Peters, and D. M. Jonas. Energy transfer: Vibronic coherence unveiled. *Nature Chemistry*, 6(3):173–175, 2014.

[20] A. Chenu, N. Christensson, H. F. Kauffmann, and T. Mancal. Enhancement of vibronic and ground-state vibrational coherences in 2d spectra of photosynthetic complexes. *Scientific Reports*, 3:2029, 2013.

[21] W. Junge. Membrane-potentials in photosynthesis. *Annual Review of Plant Physiology and Plant Molecular Biology*, 28:503–536, 1977.

[22] K. M. Pelzer, G. B. Griffin, S. K. Gray, and G. S. Engel. Inhomogeneous dephasing masks coherence lifetimes in ensemble measurements. *Journal of Chemical Physics*, 136(16):164508, 2012.

[23] P. D. Dahlberg, A. F. Fidler, J. R. Caram, P. D. Long, and G. S. Engel. Energy transfer observed in live cells using two-dimensional electronic spectroscopy. *Journal Of Physical Chemistry Letters*, 4(21):3636–3640, 2013.

[24] J. Dostal, T. Mancal, R. Augulis, F. Vacha, J. Psencik, and D. Zigmantas. Two-dimensional electronic spectroscopy reveals ultrafast energy diffusion in chlorosomes. *Journal of American Chemical Socieity*, 134(28):11611–11617, 2012.

[25] R. Augulis and D. Zigmantas. Two-dimensional electronic spectroscopy with double modulation lock-in detection: enhancement of sensitivity and noise resistance. *Optics Express*, 19(14):13126–13133, 2011.

[26] D. G. Osborne and K. J. Kubarych. Rapid and accurate measurement of the frequency-frequency correlation function. *Journal of Physical Chemistry A*, 117(29):5891–5898, 2013.

[27] V. Novoderezhkin, M. Wendling, and R. van Grondelle. Intra- and interband transfers in the b800-b850 antenna of *Rhodospirillum molischianum*: Redfield theory modeling of polarized pump-probe kinetics. *Journal of Physical Chemistry B*, 107(41):11534–11548, 2003.

[28] A. F. Fidler, V. P. Singh, P. D. Long, P. D. Dahlberg, and G. S. Engel. Timescales of coherent dynamics in the light harvesting complex 2 (lh2) of *Rhodobacter sphaeroides*. *Journal of Physical Chemistry Letters*, 4(9):1404–1409, 2013.

[29] J. K. Trautman, A. P. Shreve, C. A. Violette, H. A. Frank, T. G. Owens, and A. C. Albrecht. Femtosecond dynamics of energy transfer in b800-850 light-harvesting complexes of *Rhodobacter sphaeroides*. *Proceedings of the National Academy of Sciences*, 87(1):215–219, 1990.

[30] H. van der Laan, Th Schmidt, R. W. Visschers, K. J. Visscher, R. van Grondelle, and S. Völker. Energy transfer in the b800850 antenna complex of purple bacteria *Rhodobacter sphaeroides*: A study by spectral hole-burning. *Chemical Physics Letters*, 170(2-3):231–238, 1990.

[31] R. Monshouwer, I. O. Dezarate, F. van Mourik, and R. van Grondelle. Low-intensity pump-probe spectroscopy on the b800 to b850 transfer in the light-harvesting 2 complex of *Rhodobacter sphaeroides*. *Chemical Physics Letters*, 246(3):341–346, 1995.

[32] S. Hess, E. Akesson, R. J. Cogdell, T. Pullerits, and V. Sundström. Energy transfer in spectrally inhomogeneous light-harvesting pigment-protein complexes of purple bacteria. *Biophysical Journal*, 69(6):2211–2225, 1995.

[33] T. H. Joo, Y. W. Jia, J. Y. Yu, D. M. Jonas, and G. R. Fleming. Dynamics in isolated bacterial light harvesting antenna (lh2) of *Rhodobacter sphaeroides* at room temperature. *Journal of Physical Chemistry*, 100(6):2399–2409, 1996.

[34] J. L. Herek, N. J. Fraser, T. Pullerits, P. Martinsson, T. Polívka, H. Scheer, R. J. Cogdell, and V. Sundström. B800→b850 energy transfer mechanism in bacterial lh2 complexes investigated by b800 pigment exchange. *Biophysical Journal*, 78(5):2590–2596, 2000.

[35] E. Harel, S. M. Rupich, R. D. Schaller, D. V. Talapin, and G. S. Engel. Quantum coherence spectroscopy reveals complex dynamics in bacterial light-harvesting complex 2 (lh2). *Proceedings of the National Academy of Sciences*, 109(3):706–711, 2012.

[36] V. P. Singh, M. Westberg, C. Wang, P. D. Dahlberg, T. Gellen, A. T. Gardiner, R. J. Cogdell, and G. S. Engel. Towards quantification of vibronic coupling in photosynthetic antenna complexes. *Journal of Chemical Physics*, 142(21):212446, 2015.

[37] D. Hayes, J. Wen, G. Panitchayangkoon, R. E. Blankenship, and G. S. Engel. Robustness of electronic coherence in the fenna-matthews-olson complex to vibronic and structural modifications. *Faraday Discussions*, 150(0):459–469, 2011.

[38] V. P. Singh, A. F. Fidler, B. S. Rolczynski, and G. S. Engel. Independent phasing of rephasing and non-rephasing 2d electronic spectra. *Journal of Chemical Physics*, 139(8):084201, 2013.

[39] A. F. Fidler, V. P. Singh, P. D. Long, P. D. Dahlberg, and G. S. Engel. Dynamic localization of electronic excitation in photosynthetic complexes revealed with chiral two-dimensional spectroscopy. *Nature Communications*, 5:3286, 2014.

[40] R. Jimenez, F. van Mourik, J. Y. Yu, and G. R. Fleming. Three-pulse photon echo measurements on lh1 and lh2 complexes of *Rhodobacter sphaeroides*: A nonlinear spectroscopic probe of energy transfer. *Journal of Physical Chemistry B*, 101(37):7350–7359, 1997.

[41] V. Butkus, D. Zigmantas, L. Valkunas, and D. Abramavicius. Vibrational vs. electronic coherences in 2d spectrum of molecular systems. *Chemical Physics Letters*, 545:40–43, 2012.

[42] G. Panitchayangkoon, D. V. Voronine, D. Abramavicius, J. R. Caram, N. H. C. Lewis, S. Mukamel, and G. S. Engel. Direct evidence of quantum transport in photosynthetic light-harvesting complexes. *Proceedings of the National Academy of Sciences*, 108(52):20908–20912, 2011.

[43] J. Seibt and T. Pullerits. Combined treatment of relaxation and fluctuation dynamics in the calculation of two-dimensional electronic spectra. *Journal of Chemical Physics*, 141(11):114106, 2014.

CHAPTER 6

PRESENCE OF HIGHER LYING EXCITED STATES IN LH1

6.1 Electronic Structure Of LH1

*Photosynthetic organisms [1] have developed a nearly universal strategy in light harvesting, by which they spatially separate the absorption of solar energy and the use of that energy to generate separated charges.1 Rapid energy transfer from the site of absorption to the site of charge separation is crucial for efficient solar harvesting. In photosynthetic organisms, the absorption and charge separation sites can be separated by nearly one hundred nanometers, yet transfer occurs on the order of tens of picoseconds and with near unity quantum efficiency in low light [2, 3] To accomplish this feat, they employ specialized pigment-proteins known as antenna complexes to absorb solar energy. Antenna complexes are packed with strongly coupled chromophores. This strong coupling leads to delocalized states with strong transition dipoles and a complex electronic structure that is essential for energy transfer. In this manuscript, we employ two-dimensional electronic spectroscopy (2DES) to observe the electronic structure and dynamics of light harvesting complex 1 (LH1) from *Rhodobacter sphaeroides* (*Rba. sphaeroides*) embedded in its native photosynthetic membrane.

Rba. sphaeroides is a purple bacterium known for its near unity quantum efficiency [3] and highly symmetric antenna complexes. *Rba. sphaeroides* has two types of antenna complexes: a peripheral complex, light harvesting complex 2 (LH2) and a core complex, light harvesting complex 1, that surrounds the reaction center (RC). An 8-$\mathring{A}$ resolution structure of an RC-LH1-PufX dimer was obtained from a combination of X-ray crystallography and cryo-electron microscopy. [4, 5] This structure reveals an S-shaped array of chromophores that intertwines around two RCs. The bacteriochlorophyll (BChl) within the LH1 complex absorb maximally at 875 nm, and are often designated as B875; they share many characteristics with the B850 ring of BChl in LH2. The RC-LH1-PufX complex exists in Rba. sphaeroides as both a

∗. This work is adapted from reference [**?**]

monomer and a dimer, but the dimer is the dominant structure in vivo. Each monomer in the dimer contains 28 BChl *a* molecules bound in alternating α- and β-polypeptides (Figure 8.1). [4] The electronic coupling between BChl *a* in LH1 is well approximated by dipolar coupling except in the case of nearest neighbors where the Mg-Mg distance is on the order of 10 $\mathring{A}$. [4] The coupling strength of nearest neighbors is estimated to be a few hundred wavenumbers. [6, 7] This strong coupling leads to the delocalization of excitations across BChl *a* and the existence of higher-lying excited states. A special pair of BChl *a* embedded in each RC absorbs at 870 nm and accepts excitations from LH1. [8, 9] The LH1 complex used in this manuscript was obtained from a mutant of Rba. sphaeroides that lacked LH2, PufX, and the RC. In the absence of PufX and the RC, the predominant structure of the membrane-embedded LH1 is likely a closed, but empty ring. [10, 11] High-resolution AFM topographs of membrane-embedded LH1-only complexes showed that they are 9.9 0.7 nm in diameter, smaller than the 11.2 0.6 nm measured for monomeric RC-LH1 core complexes with 16 $\alpha_1\beta_1$BChl$_2$ LH1 subunits. [12] Accordingly, the LH1-only complex was assigned to be a ring of 15 $\alpha_1\beta_1$BChl$_2$ subunits. [11]

A closed ring, unlike an open ring, has an additional circular symmetry that leads to a series of pairwise degenerate electronic states. The manifold of states in a closed ring of LH1 adopts a labeling scheme to reflect these degeneracies. The lowest and highest energy states are the only non-degenerate states and, in the case of an LH1, are composed of 15 $\alpha_1\beta_1$BChl$_2$ subunits; these states are labeled k = 0 and k = 15. All other states are pairwise degenerate and are labeled k = $\pm$1...$\pm$14. In a perfectly symmetric monomeric ring, the transition dipole for most excited states becomes vanishingly small, so the only states with finite transition dipole strength are k = $\pm$1 and k = $\pm$14, with k = $\pm$1 being the dominant transition dipole. However, in nature, this perfect circular symmetry is never realized due to disorder. In the dimeric RC-LH1-PufX complex, the S shape breaks the circular symmetry and therefore the degeneracies. Observation of the higher-lying excited states and their lifetime in the photosynthetic membrane can inform on the nearest-neighbor

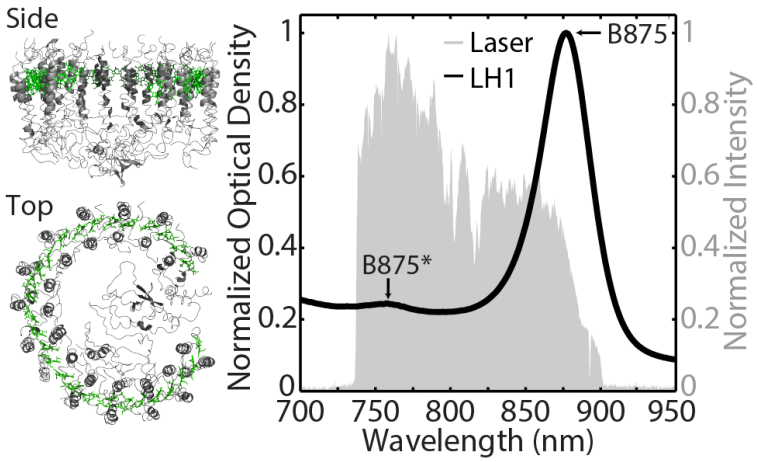

Figure 6.1: Left: The 8 $\mathring{A}$-resolution structure of a monomer of LH1 complex in *Rba. sphaeroides* reconstructed from the RC-LH1 dimeric crystal structure found in PDB ID: 4V9G. [4] The protein backbone (shown in gray) holds 28 BChl a (shown in green) tightly in space. Right: The absorption spectrum of LH1-only membranes is shown in black. The two visible features near 765 nm and 875 nm correspond to B875* and B875, respectively. The normalized laser excitation spectrum used for the 2DES experiments is shown in shaded gray.

coupling strengths, site energies and coupling to the bath, thus providing great insight into the electronic structure of LH1 in vivo.

Previous ultrafast spectroscopy studies have been performed on detergent isolated preparations of LH1. Fluorescence anisotropy data suggest the energy transfer between BChl a molecules occurs on 110 fs and 400 fs timescales. [13] Three-photon echo peak shift, pump-probe, and transient grating experiments resolved four dominant vibrational modes and two decay lifetimes. [14, 15] Pump-dump-probe and pump-probe experiments have characterized the exciton equilibration between the low-energy states as taking place on a 100 fs timescale. [16, 17] To date, none of these ultrafast studies have analyzed simultaneously the higher-lying excited states and their coupling to the strongly allowed k = ± 1 states. In this paper, we present a 2DES waiting time series of monomeric LH1-only complexes embedded in the photosynthetic membrane from *Rba. sphaeroides*. We find evidence of higher-lying excited states and resolve waiting time dynamics. We use this information to refine the site energies and nearest-neighbor couplings within the B875 band of chromophores and find good agreement between calculated and experimentally observed energy transfer rates.

6.2 Preparation Of LH1 Membranes

A mutant containing only LH1 complexes, designated L3 ($\Delta puc1BA$ $\Delta pufLMX$), was created by genomic deletion of *puc1BA* and *pufLMX* genes using the methodology described in Mothersole et al. [18] The cells were cultured semi-aerobically in the dark at 30 C. LH1-only membranes were obtained by disrupting the cells using a French press at 14,000 PSI. A slow spin was performed (12,000 RPM JA 30.STI for 20 minutes) to remove large cellular debris. The supernatant was diluted to an optical density of 0.3 at 875 nm in a 200-μm path length quartz cell (Starna Cells Inc.), which was used for analysis.

6.3 Effective Hamiltonian For LH1

Model Hamiltonians were constructed to reproduce the experimental results and revise physical parameters such as nearest neighbor coupling, site energies, and spectral density. Our sample contains a mixture of structures containing 14, 15, and 16 $\alpha_1\beta_1\text{BChl}_2$ subunits in both open and closed ring configurations. However, prior AFM studies indicate that the most prevalent structure of LH1 in the absence of PufX and the RC is a closed ring of 15 $\alpha_1\beta_1\text{BChl}_2$ subunits. [10, 11] Therefore, we constructed three separate effective Hamiltonians to account for the ill-defined structure of monomeric LH1 in the absence of PufX and the RC. The first Hamiltonian, $H^{(15)}_{closed}$, describes a closed ring of 15 subunits. Because no crystal structures exist with this geometry, a model was constructed with 30 equally spaced BChl *a* in the XY plane arranged in a ring with a radius of 5 nm. The Q_y dipole orientations were alternated between pointing at 203 and 21 in the XY plane. The orientation of the dipoles was taken from the average over the first 20 chromophores in the dimeric crystal structure starting from one end of the S-shaped band.4 The site energies were made to alternate between 12150 cm^{-1} (823 nm) and 12450 cm^{-1} (803 nm) and the nearest neighbor coupling was approximated as 435 cm^{-1}. These values were comparable to previous studies and reproduced features in the absorption spectra.6 The coupling for all other chromophores was calculated assuming purely dipolar interaction. A dipole strength of 8.3 Debye was adopted for all BChl *a* following the calculations in Şener et al. [6] The second Hamiltonian, $H^{(14)}_{open}$, was calculated in the same manner except the distances and orientations of chromophores were taken directly from one half of the LH1 in the dimeric RC-LH1-PufX crystal structure shown in Figure 6.1 which consists of a nearly-closed ring of 14 $\alpha_1\beta_1\text{BChl}_2$ LH1 subunits. [9] The third Hamiltonian, $H^{(16)}_{closed}$, was constructed in the same manner using the monomeric RC-LH1 structure from a similar organism, *Thermochromatium tepidum*. [19] This 3.0 Å-resolution structure has a closed ring of 16 $\alpha_1\beta_1\text{BChl}_2$ subunits that is slightly elliptical. The ellipticity breaks some of the degeneracies that arise from a closed ring.

The eigenstate energies and dipole strengths for $H^{(14)}_{open}$, $H^{(15)}_{closed}$, and $H^{(16)}_{closed}$ are listed

in Table 6.1, and stick spectra for all the Hamiltonians can be seen in Figure 6.2 along with the linear absorption spectrum of LH1-only membranes after the removal of Mie scatter. A comparison of the stick spectra to a 77 Kelvin absorption spectrum is made in SI Figures 6.7 and 6.8. All three Hamiltonians give rise to a strongly allowed band of excitonic states at low energy around 875 nm. This feature is the well-known B875 absorption band of LH1. In the cases of $H^{(15)}_{closed}$, and $H^{(16)}_{closed}$, the transition dipole strength is carried almost exclusively by the $k_{\pm 1}$ states that have a transition energy of 11443/11401 cm^{-1} (874/877 nm). $H^{(14)}_{open}$ provides a similar electronic structure, with the majority of the oscillator strength being carried by the three lowest energy states, E_{1-3}, with transition energies of 11396-11445 cm^{-1} (877-874 nm). All three Hamiltonians also produce weak higher-lying excited states with transition energies at approximately 13195 cm^{-1} (760 nm). These higher-lying excited states, in analogy to the higher-lying B850* states in LH2, will be referred to as B875*. The absorption spectrum is mirrored in the excitation fluorescence spectrum (Figure 6.9), indicating electronic coupling between the B875* states and the B875 states. Without further analysis, it would be difficult to separate this absorption feature from free BChl a in the sample, which absorbs at 770 nm and overlaps B875*, or from vibrationally excited B875 states. Both free BChl a as well as vibrationally excited states would likely relax to the B875 states before fluorescing. Therefore, the assignment of this feature is not conclusive based on linear absorption or fluorescence spectra alone and we therefore employ to 2DES and Redfield theory for an unambiguous assignment.

6.4 Observation Of Higher Lying State

The real portion of the phased rephasing 2DES spectra of LH1-only membranes at early waiting times, shown in Figure 6.3, reveal more features than the linear absorption spectrum. The strongest feature in the phased 2DES spectra appears as the near-diagonal peak at λ_τ = 870 nm, λ_t = 880 nm. The offset from the diagonal is likely due to overlapping excited state absorption and stimulated emission. The absolute-valued spectra for the same waiting

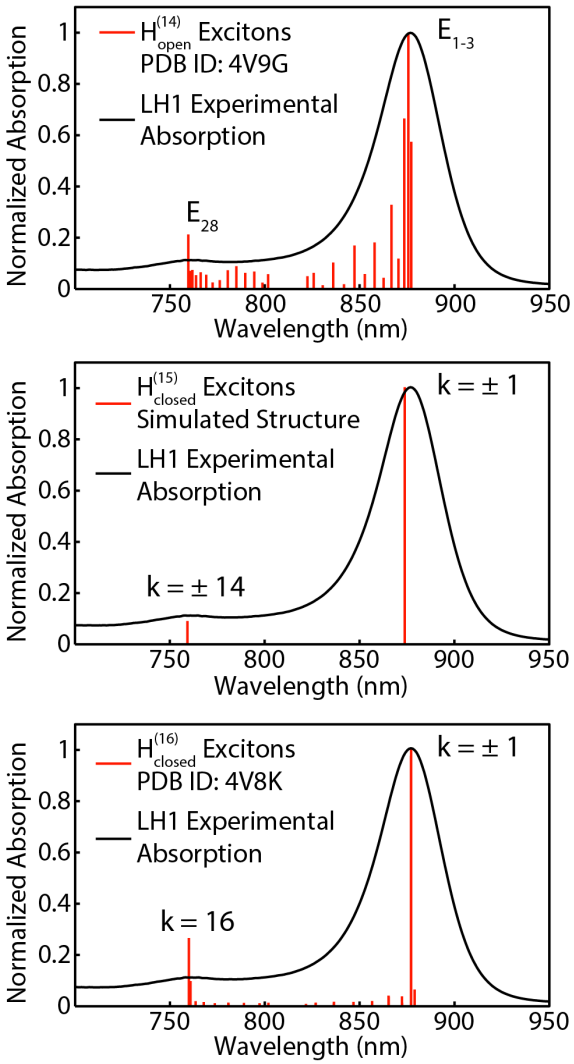

Figure 6.2: Stick spectra from $H^{(14)}_{open}$, $H^{(15)}_{closed}$, and $H^{(16)}_{closed}$ are overlaid with the absorption spectra of LH1-only membranes after the removal of Mie scatter. The stick spectra are in good agreement with the absorption spectra, recapitulating the strong B875 states and the weak B875* states.

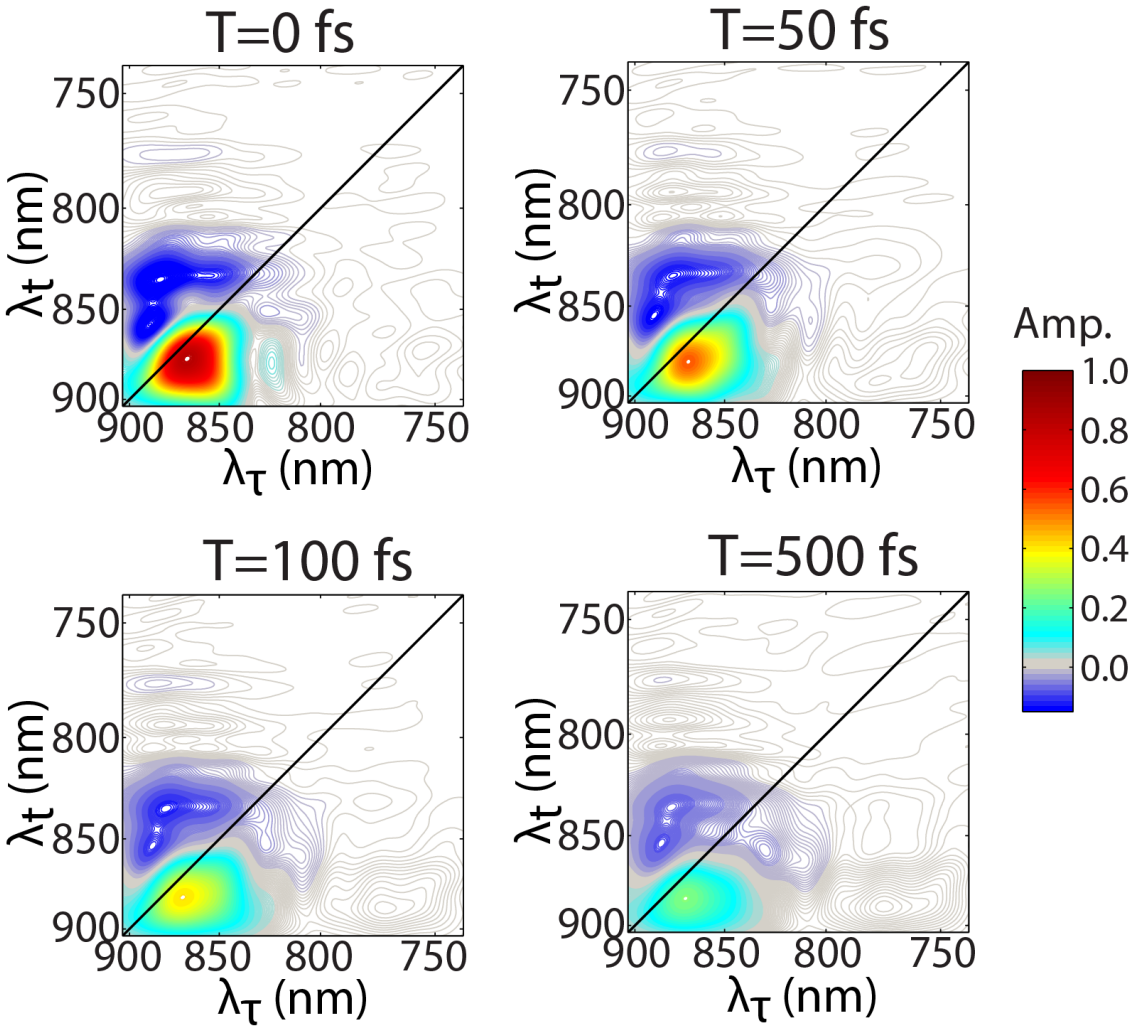

Figure 6.3: Representative phased rephasing 2DES spectra of LH1-only membranes at waiting times of T = 0 fs, T = 50 fs, T = 100 fs and T= 500 fs. All spectra are normalized to the signal maximum across all waiting times.

times are shown in Figure 6.10 and show a peak centered at λ_τ = 875 nm, λ_t = 875 nm. A regression of the phased data to a bi-exponential function yields two time constants of $\tau_1 = 55 \pm 2$ fs and $\tau_2 = 1130 \pm 26$ fs (Figure 6.11). Similar dynamics have been reported previously in LH1 and in the B850 ring from LH2 and have been attributed to vibrational relaxation, protein reorganization and spectral diffusion. [14]

A diagonal peak near $\lambda_\tau = \lambda_t$ = 770 nm corresponding to B875* is not visible due to its low intensity relative to the B875 diagonal peak. In third-order experiments, the signal intensity scales with the fourth power of transition dipoles, whereas a signal in first-

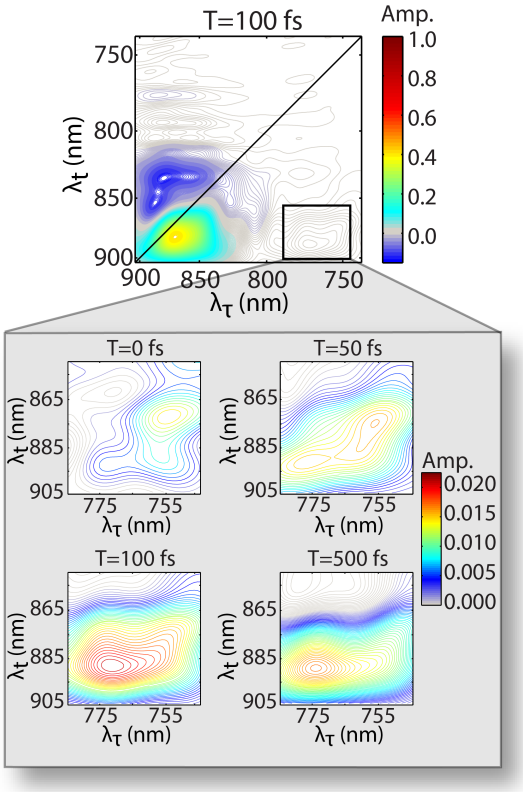

Figure 6.4: Phased rephasing 2DES spectra of the cross peak between B875* and B875 (region enclosed by the red rectangle in the 2DES spectrum above) in LH1-only membranes showing stimulated emission around λ_τ = 770 nm and λ_t = 880 nm at waiting times of T = 0 fs, T = 50 fs, T = 100 fs and T= 500 fs, respectively. All spectra are normalized to the signal maximum across all waiting times.

order experiments, such as that in a linear absorption spectrum, scales with the square of transition dipoles. Based on the linear absorption spectrum, we expect the relative strength of the B875* diagonal peak to be $(0.05)^2$, or 0.25%, of the intensity at the B875 diagonal peak, which is too weak to be observed. The signal intensity of a cross peak in a 2DES spectrum is the result of two interactions with each of the corresponding diagonal features. Based on the linear absorption spectrum, the intensity at λ_τ = 770 nm and λ_t = 880 nm would be 5% of the B875 diagonal feature if energy transferred from B875* to B875. The cross peak observed between λ_τ = 770 nm and λ_t = 880 nm has a maximum of 0.023 in the normalized spectra (Figure 6.4 and Figure 6.12).

The position and amplitude of the cross peak indicate that the states observed in the linear absorption spectrum around 770 nm are transferring excitations to B875. Nevertheless, the existence of coupling and transfer could be due to vibrationally excited B875 states or free BChl a that are loosely coupled to the B875 states, rather than transfer from higher-

lying B875* states. These possibilities can be excluded by analysis of the waiting time dynamics. The cross peak between B875* and B875 grows in rapidly at early waiting times. A representative waiting time trace at $\lambda_\tau = 770$ nm and $\lambda_t = 880$ nm is shown in Figure 6.5. We observe that the waiting time trace reaches its maximum within 100 fs. When a bi-exponential function is fit to the data, the trace gives a fast rise of 31 $\pm$ 3 fs and a slow decay of 1280 $\pm$ 100 fs (see the SI for more details on the fitting procedure). Analysis of the complete cross peak region can be seen in Figure 6.5b. The rapid timescale for the growth of this cross peak excludes any possibility of energy transfer from free BChl a to the B875 states, because any energy transfer between free BChl a and LH1 would occur on a picosecond timescale due to weak coupling.

Fourier analysis in the waiting time domain is further utilized to elucidate the origin of the cross peaks. In 2DES, vibrational states give clear oscillations in the waiting time domain that result from vibrational coherences. [20–22] A vibrational coherence is a superposition between two vibrational states within the same electronic excited state. In phased 2DES spectra, we observe excited state absorption features in the upper off-diagonal region of the map (Figure 6.3). From the waiting time trace, we see clear oscillations from this region that persist for more than 2 ps (Figure 6.6a), which is on the appropriate timescale for vibrational coherences at room temperature. Fourier transforming the residual from exponential fitting yields four distinct vibrational modes at 96, 288, 558, and 728 cm-1 (Figure 6.6b). These vibrational modes are also observed in the Raman spectrum of LH1 and free BChl a.15, [23–25] When the cross peak between B875* and B875 is analyzed, no clear oscillations indicative of vibrational coherences can be resolved (Figure 6.6 c and d). Thus, we attribute the cross peak on the lower off-diagonal region to be energy transfer from higher-lying B875* states to lower-lying B875 states.

Redfield theory was further used to validate the rapid energy transfer rates observed from B875* to B875. The sub-100 fs transfer rate is similar to results obtained in LH2 from B850* to B850. [26] The rapid energy transfer is largely due to the co-localization of

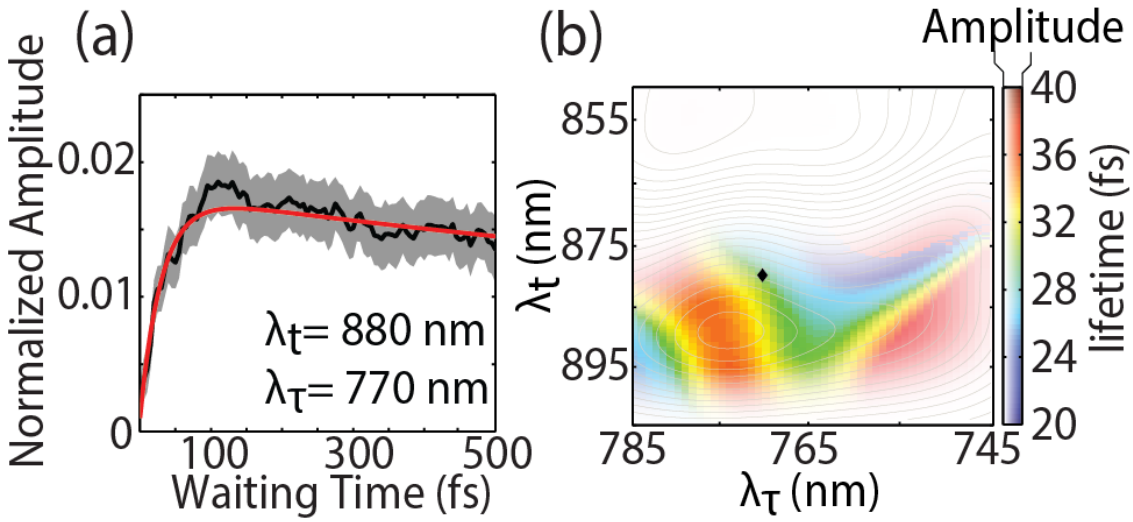

Figure 6.5: Representative waiting time trace and lifetime map at the B875*-B875 cross peak of LH1-only membranes show rapid energy transfer within 40 fs. (a) The black curve is the average waiting time trace of LH1-only membranes at $\lambda_\tau = 770$ nm and $\lambda_t = 880$ nm (indicated by black diamond in the spectrum to the right) over of 10 scans acquired in rapid succession over the course of 2 hours. The width of the gray shading is $\pm$ the standard error on the mean defined as $\sigma/\sqrt{10}$ where σ is the standard deviation of the 10 replicates. The gray shading indicates the error on the mean of 10 scans completed in rapid succession over the course of 2 hours. The red trace is a regression of the data to a model bi-exponential function. (b) Lifetime map for the rapid component of the bi-exponential around $\lambda_\tau = 770$ nm and $\lambda_t = 880$ nm. The saturation level of the map is weighted by both the signal strengths at T = 500 fs for each pixel. The contour curves represent the phased 2DES spectrum at waiting time of 100 fs.

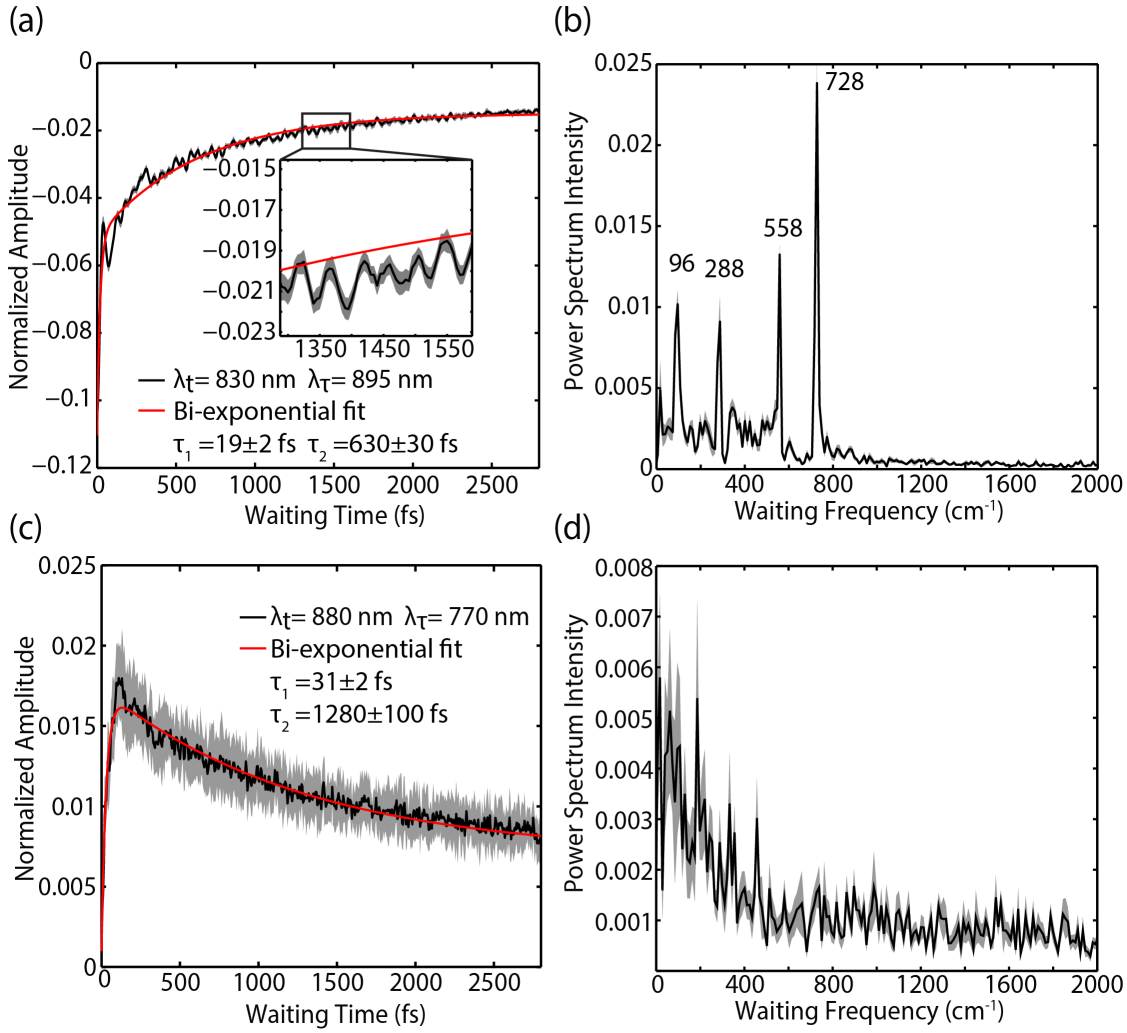

Figure 6.6: Waiting time traces from two locations in the 2DES spectra and their conjugate waiting time frequency traces show no clear vibrations at the cross peak between B875* and B875. All black traces in the figures represent an average of 10 scans. The width of the gray shading is ± the standard error on the mean defined as $\sigma/\sqrt{10}$ where σ is the standard deviation of the 10 replicates.Gray shading indicates the error on the mean. *(a)* Waiting time trace of LH1-only membranes at $\lambda_\tau = 895$ nm and $\lambda_t = 830$ nm showing oscillations due to vibrational coherences at this location. *(b)* Average power spectrum of the residuals from fitting the same waiting time trace in *(a)* for each of the 10 scans (resolution is 11 cm^{-1}). These peaks are known vibrational modes of BChl *a*. [23] *(c)* Waiting time trace from the B875*-B875 lower cross peak at $\lambda_\tau = 770$ nm and $\lambda_t = 880$ nm. *(d)* Average power spectrum of the residuals from fitting the same waiting time trace in *(c)* for each of the 10 scans.

the excitations on the same ring of chromophores. Figure 6.13 shows the transition dipole weight for the B875 and B875* states for the three Hamiltonians. In addition to spatially overlapping states, the rapid rate of energy transfer is also due to high-energy bath modes, some of which can be seen in the vibrational coherences in Figures 6.6 and 6.14. In order to properly weight these high-energy bath modes, we used a log-normal spectral density given by

$$J(\omega) = \frac{S}{\sigma\omega\sqrt{2\pi}} e^{-\ln(\frac{\omega}{\omega_c})/2\sigma^2} \tag{6.1}$$

with a high cutoff frequency, ω_c, of 1000 cm$-$1. [27] The Huang-Rhys factor, S, was 0.5 and the standard deviation, σ, was 0.8 cm^{-1}. Using this spectral density, the population transfer time was calculated following the procedure outlined by M. Reppert. [28] The lifetime for $H^{(15)}_{closed}$, calculated as the transfer time from $k_{\pm 14}$ to k_0 and $k_{\pm 1}$, was found to be 51 fs. Similarly, the lifetime for $H^{(16)}_{closed}$, calculated as the transfer time from k_{16} to k_0 and $k_{\pm 1}$, was found to be 54 fs. Lastly, the lifetime for $H^{(14)}_{open}$, calculated as the transfer time from E_{28} to E_{1-3}, was found to be 42 fs. All values are within a factor of two of the observed energy transfer lifetimes of 30-40 fs.

6.5 Biological Significance

The rapid growth of the cross peak and lack of vibrational coherences in the waiting time frequency domain firmly assigns the B875* states as electronic in origin. Their rapid transfer to B875 mirrors the dynamics found in the B850* and B850 states of LH2 and is in agreement with the effective Hamiltonians and Redfield theory calculations of population transfer rates. The role of B875* remains uncertain. The energy of B875* and its proximity to the RC and LH2 raises the possibility of it being an intermediate state as energy is transferred from the peripheral antenna to the RC, though this is unlikely. Due to the short lifetime of B875*, direct transfer to the RC would not compete with relaxation to the B875 ring despite the strong spectral overlap of the H and B peaks of the RC with the B875* states. Also, the

distance between B800 and B875 makes energy transfer from B800 to B875* an unlikely pathway. While other mechanisms such as super-transfer or moderation of energy transfer based the state of the reaction center are conceivable, the presence of the B875* states is likely an informative byproduct of the strong coupling between chromophores in the B875 ring, which is essential for biological function.

6.A LH1 Model Eigenvalue Tables And Supporting Figures

Eigenvalues For $H^{(14)}_{open}$ cm^{-1} (nm)	Transition Dipole Strength $H^{(14)}_{open}$ (Debye)
E_1 = 11396 (877)	**17.5**
E_2 = 11416 (876)	30.5
E_3 = 11445 (874)	20.3
E_4 = 11485 (870)	3.6
E_5 = 11534 (867)	10.0
E_6 = 11590 (863)	1.3
E_7 = 11654 (868)	5.5
E_8 = 11725 (853)	1.7
E_9 = 11801 (847)	5.2
E_{10} = 11878 (842)	0.5
E_{11} = 11959 (836)	3.1
E_{12} = 12038 (831)	0.4
E_{13} = 12109 (826)	1.9
E_{14} = 12157 (823)	1.5
E_{15} = 12472 (802)	1.7
E_{16} = 12519 (799)	0.7
E_{17} = 12588 (794)	2.0
E_{18} = 12663 (790)	1.9
E_{19} = 12739 (785)	2.7
E_{20} = 12813 (780)	2.2
E_{21} = 12882 (776)	1.0
E_{22} = 12946 (772)	0.7
E_{23} = 13003 (769)	1.7
E_{24} = 13053 (766)	2.0
E_{25} = 13094 (764)	1.6
E_{26} = 13127 (762)	2.2
E_{27} = 13151 (760)	2.1
E_{28} = 13164 (760)	**6.5**

Eigenvalues For $H^{(15)}_{closed}$ cm^{-1} (nm)	Transition Dipole Strength $H^{(15)}_{closed}$ (Debye)
k_0 = 11377 (875)	0
$k_{\pm1}$ = 11443 (874)	**32.0**
$k_{\pm2}$ = 11495 (870)	0
$k_{\pm3}$ = 11580 (864)	0
$k_{\pm4}$ = 11696 (855)	0
$k_{\pm5}$ = 11835 (845)	0
$k_{\pm6}$ = 11987 (834)	0
$k_{\pm7}$ = 12120 (825)	0
$k_{\pm8}$ = 12470 (802)	0
$k_{\pm9}$ = 12604 (793)	0
$k_{\pm10}$ = 12758 (784)	0
$k_{\pm11}$ = 12901 (775)	0
$k_{\pm12}$= 13022 (768)	0
$k_{\pm13}$ = 13112 (763)	0
$k_{\pm14}$ = 13168 (759)	**2.9**
k_{15} = 13188 (758)	0

Eigenvalues For $H^{(16)}_{closed}$ cm^{-1} (nm)	Transition Dipole Strength $H^{(16)}_{closed}$ (Debye)
k_0 = 11377 (879)	2.1
$k_{\pm1}$ = 11401 (877)	**32.8**
$k_{\pm2}$ = 11464 (872)	0.8
$k_{\pm3}$ = 11558 (865)	1.3
$k_{\pm4}$ = 11675 (856)	0.6
$k_{\pm5}$ = 11811 (847)	0.5
$k_{\pm6}$ = 11957 (836)	0.5
$k_{\pm7}$ = 12097 (827)	0.4
k_{-8} = 12172 (822)	0.3
k_{+8} = 12473 (802)	0.5
$k_{\pm9}$ = 12546 (797)	0.3
$k_{\pm10}$ = 12677 (789)	0.4
$k_{\pm11}$ = 12811 (780)	0.4
$k_{\pm12}$ = 12930 (772)	0.3
$k_{\pm13}$ = 13029 (768)	0.4
$k_{\pm14}$ = 13102 (763)	0.5
$k_{\pm15}$ = 13148 (761)	3.1
k_{16} = 13163 (760)	8.7

Table 6.1: Eigenvalues and their transition dipole strengths for the three effective Hamiltonians. $H^{(14)}_{open}$ was produced by taking an LH1 monomer from the RC-LH1-PufX dimer crystal structure, which has 14 $\alpha_1\beta_1$BChl$_2$ subunits. $H^{(15)}_{closed}$ was produced from an ideal closed ring structure with 15 $\alpha_1\beta_1$BChl$_2$ subunits. $H^{(16)}_{closed}$ was produced from the monomeric crystal structure of LH1-RC from *Thermochromatium tepidum*, which has 16 $\alpha_1\beta_1$BChl$_2$ subunits. The states primarily responsible for B875 and B875* are shown in bold. The dipole strengths of individual Bchl *a* were assumed to be 8.3 Debye.

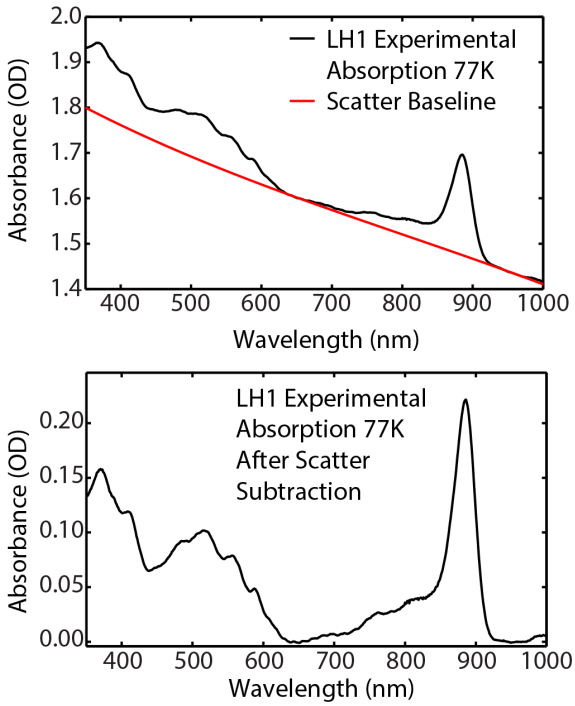

Figure 6.7: *(top)* The absorption spectrum of LH1-only membranes at 77 K is shown in black. The red trace shows a cubic polynomial fit used to subtract the contributions for scattering. *(bottom)* Absorption spectrum of LH1-only membranes at 77 K after the scatter subtraction operation.

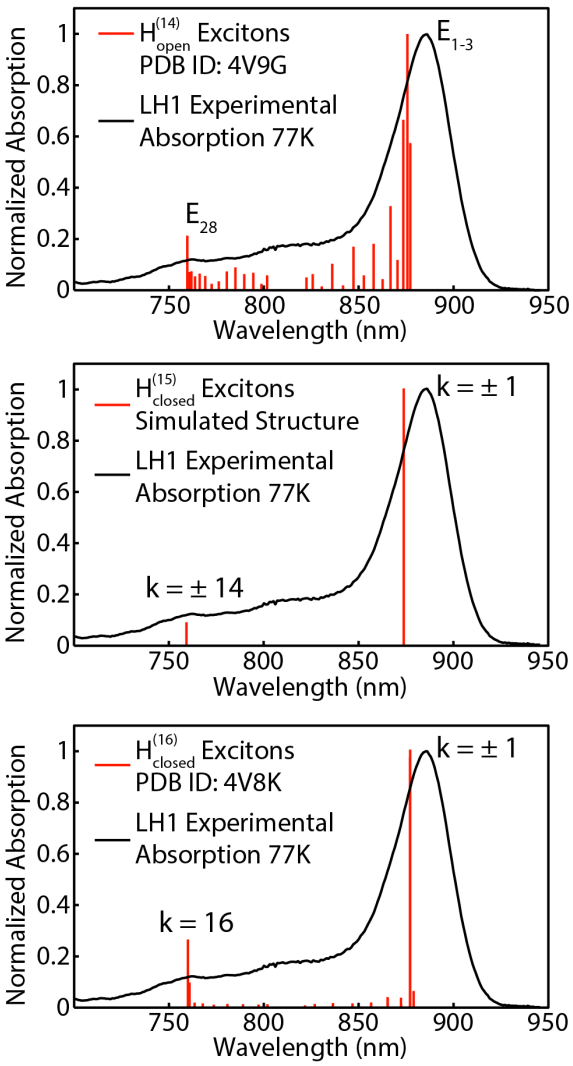

Figure 6.8: Stick spectra from $H^{(14)}_{open}$, $H^{(15)}_{closed}$, and $H^{(16)}_{closed}$ are overlaid with the absorption spectra of LH1-only membranes at 77 K after the removal of scatter. The stick spectra are in better agreement with the absorption spectra taken at room temperature, but significant structure at higher energies than the strong B875 feature can be seen in the 77 K structure.

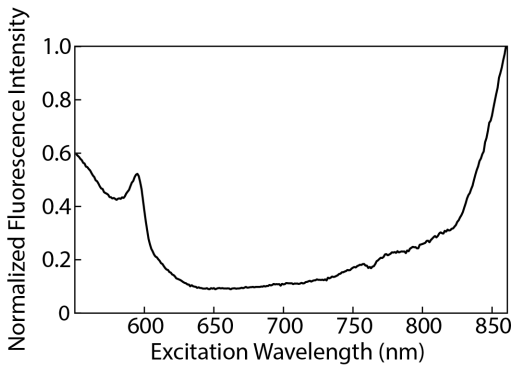

Figure 6.9: Fluorescence excitation spectrum of LH1-only membranes. Fluorescence intensity was monitored at 890 nm. The clear fluorescence signal from excitation at 750-800 nm shows energy transfer from B875* to B875.

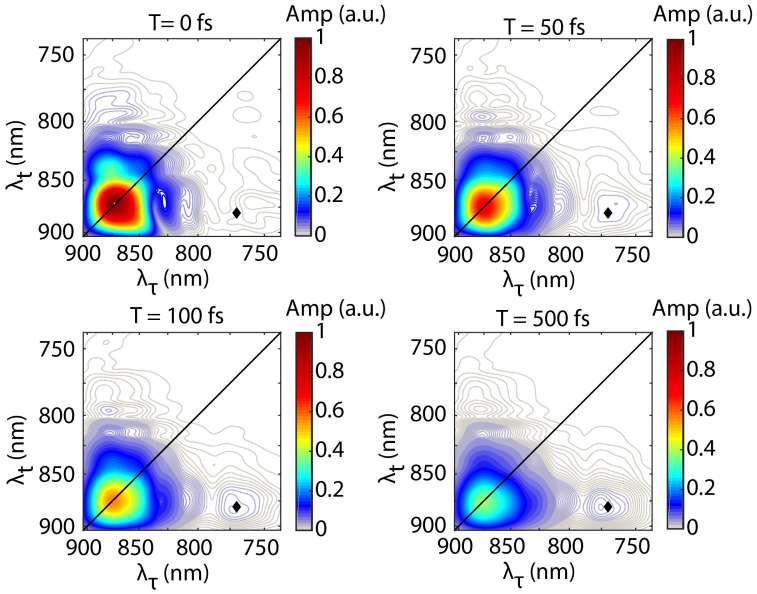

Figure 6.10: Absolute-valued rephasing 2DES spectra of LH1-only membranes. The strong signal on the diagonal corresponds to the B875 states. The cross peak centered on the black diamond is indicative of B875* to B875 energy transfer.

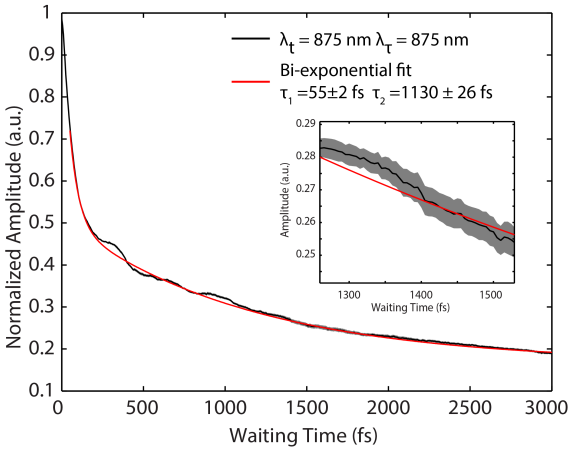

Figure 6.11: The average waiting time trace from the main diagonal of LH1-only membranes at $\lambda_\tau = \lambda_t = 875$ nm in absolute-valued signal intensity (shown in black). The black trace is the average of 10 replicates completed in rapid succession over the course of 2 hours. Dynamics are recovered by fitting to a bi-exponential and are similar to previous results. The width of the gray shading is $\pm$ the standard error on the mean defined as $\sigma/\sqrt{10}$ where σ is the standard deviation of the 10 replicates

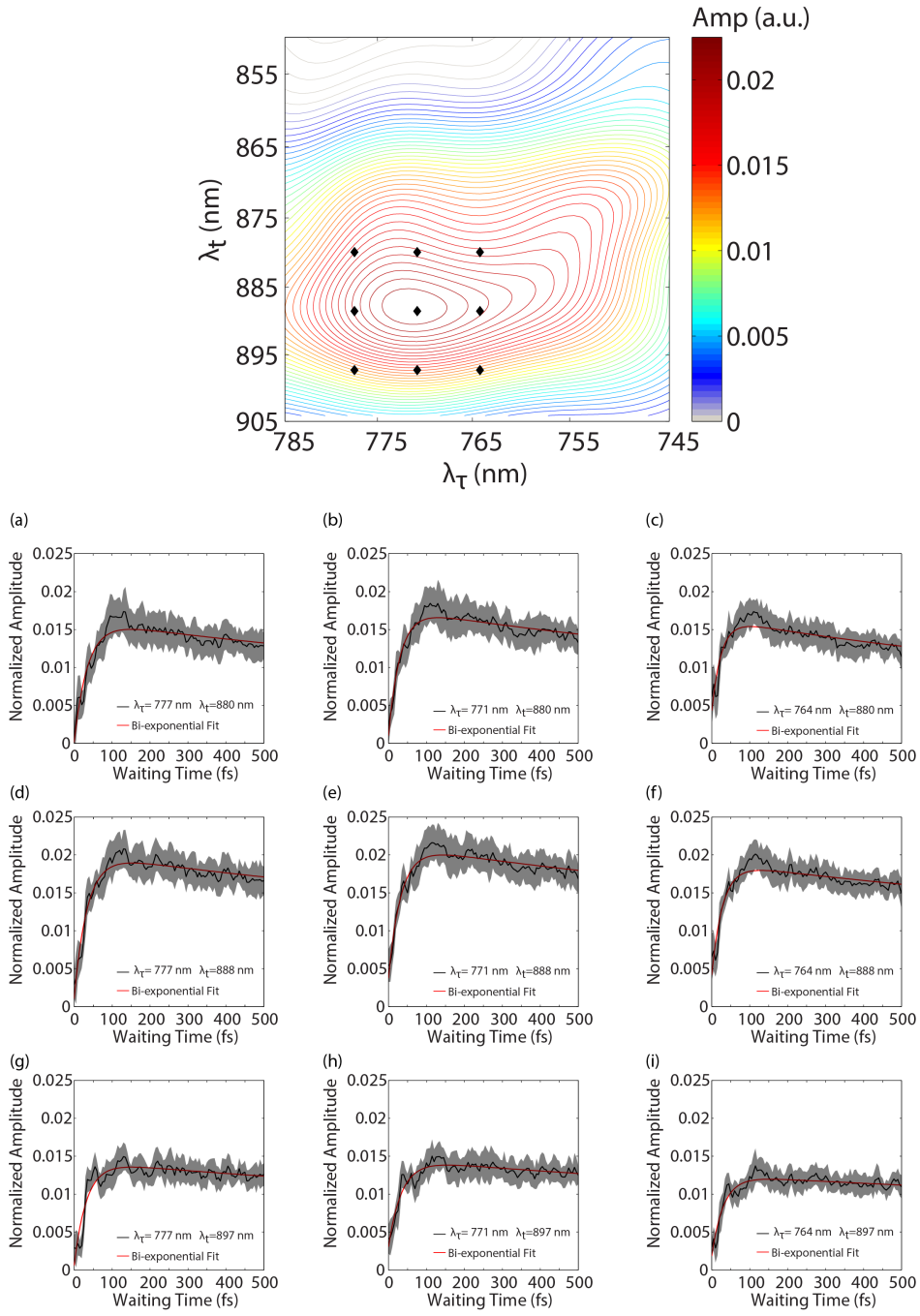

Figure 6.12: Waiting time traces from throughout the B875*-B875 cross peak shown in the zoomed-in phased 2DES spectrum (real part) at the top. Plots are reproduced in the same order as the black diamonds on the 2DES spectrum. The width of the gray shading is ± the standard error on the mean defined as $\sigma/\sqrt{10}$ where σ is the standard deviation of the 10 replicates. Red traces show a regression of the data to a model bi-exponential function.

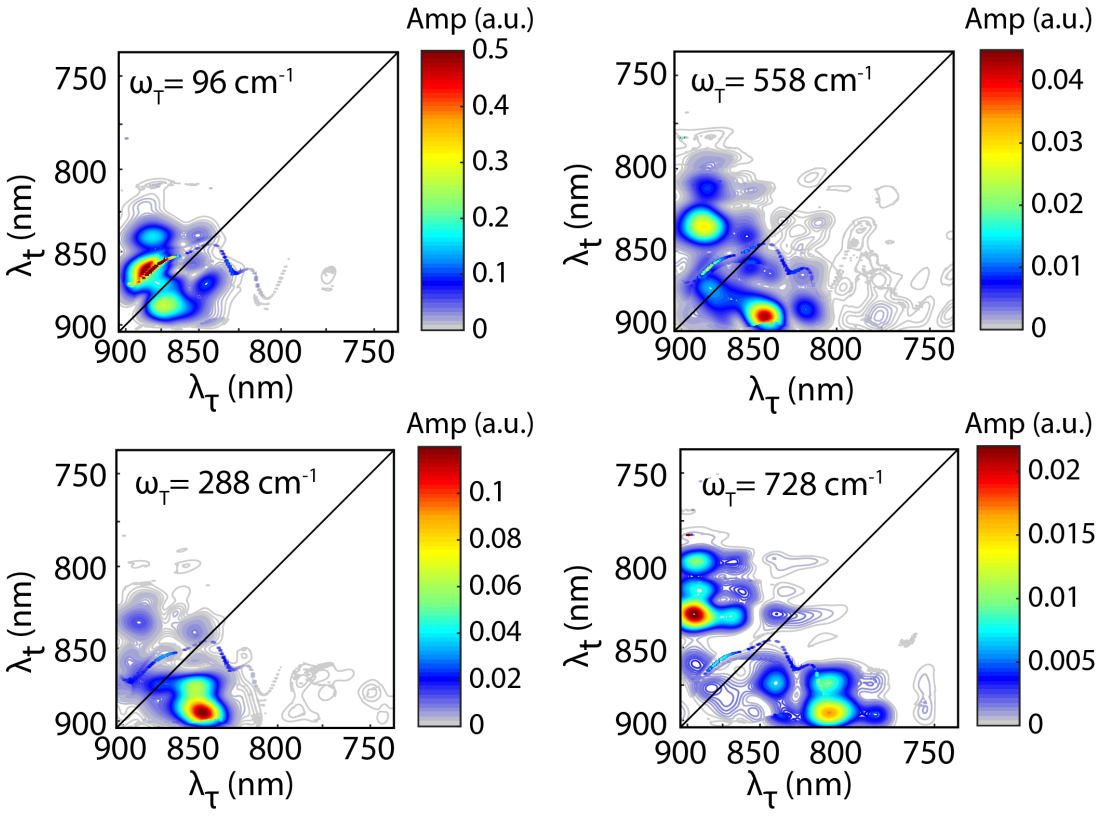

Figure 6.13: The chromophore transition dipole strengths for B875 and B875* are displayed for each Hamiltonian. The diameter of the dots scale linearly with the dipole strength. There is a large overlap between B875 and B875*, which leads to the rapid rates of observed energy transfer.

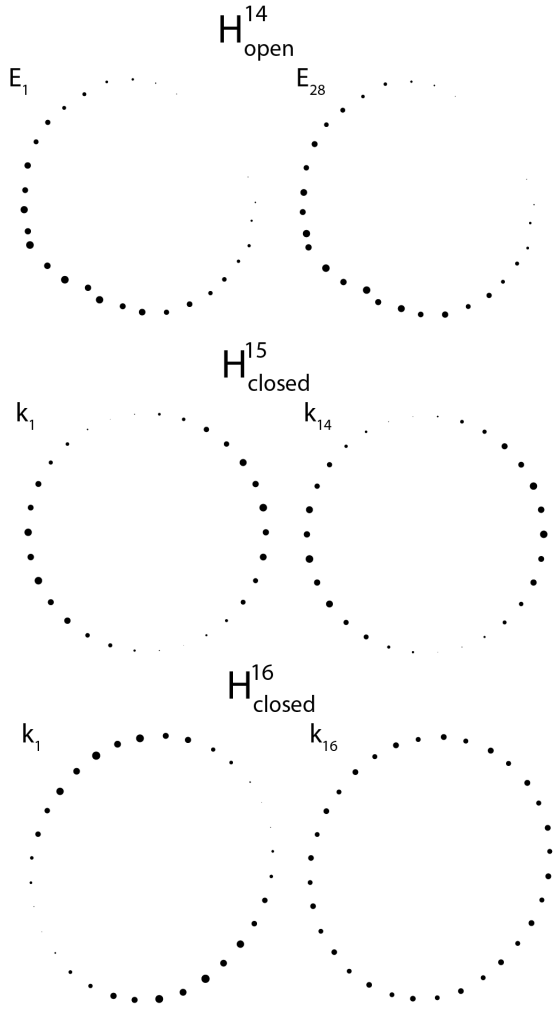

Figure 6.14: Waiting time frequency amplitude maps. These maps were obtained by fitting a bi-exponential function to each (λ_τ, λ_t) waiting time trace in the average 2DES cube of data and taking the power spectrum of the residuals. The resulting power spectra were normalized to the maximum of the frequency-frequency-frequency cube and select waiting time frequencies are displayed above. Each is a well-known vibrational mode of BChl *a*. Near nodes in the 2D spectra where signal is small, our fitting algorithm fails to converge leading to artifacts in the Fourier spectrum of the residuals along the nodes.

REFERENCES

[1] R. E. Blankenship. *Molecular mechanisms of photosynthesis*. Blackwell Science, Malden, Massachusetts, 2002.

[2] H. van Amerongen, L. Valkunas, and R. van Grondelle. *Photosynthetic excitons*. World Scientific, River Edge, N.J., 2000.

[3] C. A. Wraight and R. K. Clayton. Absolute quantum efficiency of bacteriochlorophyll photooxidation in reaction centers of *Rhodopseudomonas spheroides*. *Biochimica Et Biophysica Acta*, 333(2):246–260, 1974.

[4] P. Qian, M. Z. Papiz, P. J. Jackson, A. A. Brindley, I. W. Ng, J. D. Olsen, M. J. Dickman, P. A. Bullough, and C. N. Hunter. Three-dimensional structure of the *Rhodobacter sphaeroides* rc-lh1-pufx complex: Dimerization and quinone channels promoted by pufx. *Biochemistry*, 52(43):7575–7585, 2013.

[5] P. Qian, P. A. Bullough, and C. N. Hunter. Three-dimensional reconstruction of a membrane-bending complex - the rc-lh1-pufx core dimer of *Rhodobacter sphaeroides*. *Journal of Biological Chemistry*, 283(20):14002–14011, 2008.

[6] M. Şener, J. Hsin, L. G. Trabuco, E. Villa, P. Qian, C. N. Hunter, and K. Schulten. Structural model and excitonic properties of the dimeric rclh1pufx complex from *Rhodobacter sphaeroides*. *Chemical Physics*, 357(1-3):188–197, 2009.

[7] A. Damjanovic, T. Ritz, and K. Schulten. Excitation energy trapping by the reaction center of *Rhodobacter sphaeroides*. *International Journal of Quantum Chemistry*, 77(1):139–151, 2000.

[8] K. J. Visscher, H. Bergstrom, V. Sundström, C. N. Hunter, and R. van Grondelle. Temperature-dependence of energy-transfer from the long wavelength antenna bchl-896 to the reaction center in *Rhodospirillum rubrum*, *Rhodobacter sphaeroides* (wt and m21

mutant) from 77 to 177k, studied by picosecond absorption-spectroscopy. *Photosynthesis Research*, 22(3):211–217, 1989.

[9] L. M. P. Beekman, F. van Mourik, M. R. Jones, H. M. Visser, C. N. Hunter, and R. van Grondelle. Trapping kinetics in mutants of the photosynthetic purple bacterium *Rhodobacter sphaeroides* - influence of the charge separation rate and consequences for the rate-limiting step in the light-harvesting process. *Biochemistry*, 33(11):3143–3147, 1994.

[10] S. Bahatyrova, R. N. Frese, K. O. van der Werf, C. Otto, C. N. Hunter, and J. D. Olsen. Flexibility and size heterogeneity of the lh1 light harvesting complex revealed by atomic force microscopy - functional significance for bacterial photosynthesis. *Journal of Biological Chemistry*, 279(20):21327–21333, 2004.

[11] J. D. Olsen, P. G. Adams, P. J. Jackson, M. J. Dickman, P. Qian, and C. N. Hunter. Aberrant assembly complexes of the reaction center light-harvesting 1 pufx (rc-lh1-pufx) core complex of *Rhodobacter sphaeroides* imaged by atomic force microscopy. *Journal of Biological Chemistry*, 289(43):29927–29936, 2014.

[12] S. J. Jamieson, P. Y. Wang, P. Qian, J. Y. Kirkland, M. J. Conroy, C. N. Hunter, and P. A. Bullough. Projection structure of the photosynthetic reaction centre-antenna complex of *Rhodospirillum rubrum* at 8.5 angstrom resolution. *EMBO Journal*, 21(15):3927–3935, 2002.

[13] S. E. Bradforth, R. Jimenez, F. van Mourik, R. van Grondelle, and G. R. Fleming. Excitation transfer in the core light-harvesting complex (lh1) of *Rhodobacter sphaeroides* - an ultrafast fluorescence depolarization and annihilation study. *Journal of Physical Chemistry*, 99(43):16179–161912, 1995.

[14] R. Jimenez, F. van Mourik, J. Y. Yu, and G. R. Fleming. Three-pulse photon echo measurements on lh1 and lh2 complexes of *Rhodobacter sphaeroides*: A nonlinear spec-

troscopic probe of energy transfer. *Journal of Physical Chemistry B*, 101(37):7350–7359, 1997.

[15] M. Chachisvilis, T. Pullerits, M. R. Jones, C. N. Hunter, and V. Sundström. Vibrational dynamics in the light-harvesting complexes of the photosynthetic bacterium *Rhodobacter sphaeroides*. *Chemical Physics Letters*, 224(3-4):345–351, 1994.

[16] T. A. C. Stuart, M. Vengris, V. I. Novoderezhkin, R. J. Cogdell, C. N. Hunter, and R. van Grondelle. Direct visualization of exciton reequilibration in the lh1 and lh2 complexes of *Rhodobacter sphaeroides* by multipulse spectroscopy. *Biophysical Journal*, 100(9):2226–2233, 2011.

[17] T. Pullerits, M. Chachisvilis, M. R. Jones, C. N. Hunter, and V. Sundström. Exciton dynamics in the light-harvesting complexes of *Rhodobacter sphaeroides*. *Chemical Physics Letters*, 224(3-4):355–365, 1994.

[18] D. J. Mothersole, P. J. Jackson, C. Vasilev, J. D. Tucker, A. A. Brindley, M. J. Dickman, and C. N. Hunter. Pucc and lhaa direct efficient assembly of the light-harvesting complexes in *Rhodobacter sphaeroides*. *Molecular Microbiology*, 99(2):307–327, 2016.

[19] S. Niwa, L. J. Yu, K. Takeda, Y. Hirano, T. Kawakami, Wang, Z. Y. Otomo, and K. Miki. Structure of the lh1-rc complex from *Thermochromatium tepidum* at 3.0 angstrom. *Nature*, 508(7495):228–232, 2014.

[20] K. A. Fransted and G. S. Engel. Probing vibrational dynamics of pm650 with two-dimensional electronic spectroscopy. *Chemical Physics*, 403:59–67, 2012.

[21] K. A. Fransted, J. R. Caram, D. Hayes, and G. S. Engel. Two-dimensional electronic spectroscopy of bacteriochlorophyll *a* in solution: Elucidating the coherence dynamics of the fenna-matthews-olson complex using its chromophore as a control. *Journal of Chemical Physics*, 137(12):125101, 2012.

[22] V. Butkus, D. Zigmantas, L. Valkunas, and D. Abramavicius. Vibrational vs. electronic coherences in 2d spectrum of molecular systems. *Chemical Physics Letters*, 545:40–43, 2012.

[23] R. J. Donohoe, H. A. Frank, and D. F. Bocian. Resonance raman-spectra and normal mode descriptions of a bacteriochlorophyll-*a* model complex. *Photochemistry and Photobiology*, 48(4):531–537, 1988.

[24] N. J. Cherepy, A. P. Shreve, L. J. Moore, S. G. Boxer, and R. A. Mathies. Temperature dependence of the q_y resonance raman spectra of bacteriochlorophylls, the primary electron donor, and bacteriopheophytins in the bacterial photosynthetic reaction center. *Biochemistry*, 36(28):8559–8566, 1997.

[25] A. P. Shreve, N. J. Cherepy, S. Franzen, S. G. Boxer, and R. A. Mathies. Rapid-flow resonance raman-spectroscopy of bacterial photosynthetic reaction centers. *Proceedings of the National Academy of Sciences*, 88(24):11207–11211, 1991.

[26] V. Novoderezhkin, M. Wendling, and R. van Grondelle. Intra- and interband transfers in the b800-b850 antenna of *Rhodospirillum molischianum*: Redfield theory modeling of polarized pump-probe kinetics. *Journal of Physical Chemistry B*, 107(41):11534–11548, 2003.

[27] A. Kell, X. Feng, M. Reppert, and R. Jankowiak. On the shape of the phonon spectral density in photosynthetic complexes. *Abstracts of Papers of the American Chemical Society*, 247, 2013.

[28] M. Reppert. Modeling of resonant hole-burning spectra in excitonically coupled systems: The effects of energy-transfer broadening. *Journal of Physical Chemistry Letters*, 2(21):2716–2721, 2011.

CHAPTER 7

ENERGY TRANSFER IN *RHODOBACTER SPHAEROIDES*

Until now, the only non-invasive spectroscopy that could be performed in living systems was fluorescence spectroscopy, but fluorescence spectroscopy is only directly sensitive to bright states i.e. those with strong, optically allowed transitions. [1] But most of the light absorbed in photosynthesis does not decay via fluorescence. In low-light conditions, when photoprotective mechanisms are not activated, 80-95% of excitations are trapped by reaction centers. [2] Conversely, in high-light conditions, the majority of excitations decay via non-photochemical quenching pathways that often involve dark states. [3–5] Additionally, fluorescence spectroscopies can correlate excitation and emission energies, but information regarding the energetic path that the excited state took from absorption to emission must be inferred from a more complete knowledge of the biological system. [6, 7] Unlike fluorescence spectroscopy, nonlinear spectroscopies, like pump-probe and two-dimensional electronic spectroscopy (2DES), are directly sensitive to dark states and bright states, routinely have sub picosecond temporal resolution, and in the case of 2DES give exquisite information on the energetic path excited states take. [8–10] In this work, we present 2DES data acquired in living Rba. Sphaeroides at room temperature. We recover timescales for energy transfer through the entire network of antenna complexes; LH2→LH2 transfer, LH2→LH1 transfer, LH1→LH1 transfer, and LH1→ RC transfer. From these timescales we are able construct a model that reproduces the path of the excitations observed in 2DES and constrain the number of LH2, LH1 and RC that are coupled in a functional photosynthetic unit.

Measuring energy transfer dynamics in well-connected systems of identical subunits, like those found in photosynthetic membranes, presents two key experimental challenges. First, much of the energy transfer is occurring between isoenergetic complexes that are indistinguishable from one another and second, even at relatively low excitation concentrations exciton-exciton annihilation can dominate observed dynamics. [11, 12] We can use the annihilation dynamics to determine energy transfer times between the isoenergetic complexes. [13]

Figure 7.1 shows the absorptive 2DES spectrum of the LH2-only cells at a waiting time of 1 ps at our highest excitation fluence of 17.6 μJ/cm^2.* The waiting time traces are taken from the maximum of the ground state bleach and stimulated emission feature. The traces are normalized to 1 ps and show clear power-dependent dynamics. From the molar extinction coefficient of LH2 and the excitation spectrum one can calculate that the lowest excitation fluences of 3.6 and 2.2 μJ/cm^2 correspond to exciting 1 in every 30 to 50 LH2 respectively. The changing dynamics between these fluences is indicative of exciton-exciton annihilation and suggest a large number of connected LH2, in agreement with previous studies. [12, 14] The same power-dependent study is reproduced for the LH1-only cells and the wild type cells in figures 7.6 and 7.7. Both show annihilation only at the highest fluence. In the LH1-only cells 17.6 μJ/cm^2 corresponds to exciting 1 in every 8 LH1. The lack of annihilation at 5.6 μJ/cm^2, when only 1 in every 25 LH1, suggests the number of energetically coupled LH1s in LH1-only cells is significantly smaller than the number of coupled LH2s in LH2-only cells.

7.1 Annihilation As A Probe

The process of annihilation can be used to recover energy transfer times between isoenergetic complexes, which are normally unobtainable in 2DES studies because they yield no cross peaks or decays. Following the analysis of Barzda et al. on aggregates of an isolated antenna from plants [11, 13] the annihilation rate, γ_0, is related to the transfer time, τ_{hop}, by

$$\gamma_0^{-1} = 0.5 \times N \times f_d(N) \times \tau_{hop} \tag{7.1}$$

N is the number of connected LH2, and $f_d(N)$ is the structure factor indicative of the packing arrangement. At large values of N, $f_d(N)$ depends weakly on N and is determined by the assumed arrangement of chromophores and typically holds a value between 0.5 and 1. Based on previous AFM studies, [15] we assume an arrangement between a square lattice, f_d =

∗. see Figure 7.5 for a time series from the various data sets

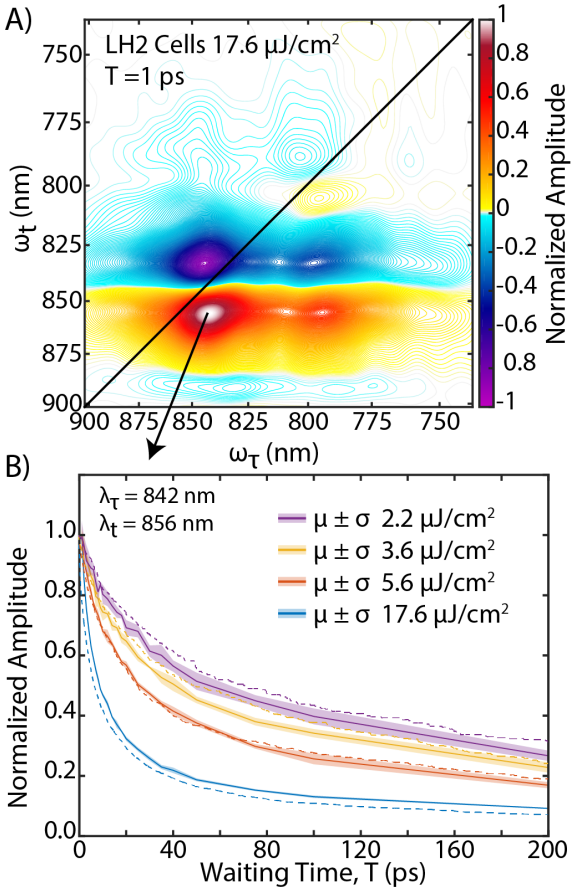

Figure 7.1: *top* Absorptive 2DES spectrum of LH2-only cells taken with 17.6 μJ/cm^2 at T = 1 ps. *bottom* Waiting time traces acquired at different powers from the spectral location indicated. The traces are the average of 3 scans and the shaded background is the mean $\pm$ the standard error. The change in dynamics with power is indicative of exciton-exciton annihilation. The dashed traces are the population of excited LH2 from a random walk model with a lifetime for energy transfer between LH2s of 2.7 ps, a domain size of 64 LH2, and an internal lifetime of 250 ps.

0.8, and a hexagonal lattice, $f_d = 0.6$, and take $f_d(N)$ to be a constant value of 0.7. The 2DES signal can then be related to the annihilation rate via

$$\frac{1}{n(T) - 1/n(0)} = \frac{\gamma_0}{d_s} \times T^{d_s/2} \tag{7.2}$$

Where $n(T)$ is the population of excitations at waiting time T, and d_s is the fractal dimension, typically around 1.8, which accounts for diffusion being restricted in the membrane to the lattice of antenna complexes. [16] In 2DES, the first two ultrafast pulses create the population of excited states, $n(T)$, and the recovered signal strength is linearly related to this population. Equation 7.2 is simply a linear relationship when the log of both sides is taken

$$log(\frac{1}{n(T)} - \frac{1}{n(0)}) = d_{s/2} \times log(T) + log(\frac{\gamma_0}{d_s}) \tag{7.3}$$

Using equations 7.1 and 7.3 we can recover the annihilation rate, γ_0. In this fashion, we extract the transfer time among LH2 complexes from the LH2-only mutant and among LH1 complexes from the LH1-only mutant. Figure 7.2 illustrates the experimental procedure for recovering the energy transfer time between LH2s. Figure 7.2A shows the 2DES spectra of LH2-only cells at a waiting time of 1 ps acquired with an excitation power of 5.6 μJ/cm^2. Waiting time traces from this data set, like the one taken from the maximum of the ground state bleach and stimulated emission feature, can be fit according to equation 7.3 to give an estimate of the annihilation rate, see figure 7.2B. Using equation 7.1 we can recover the lifetime of energy transfer between LH2 complexes. This analysis is performed for each point in the 2D spectrum within the dashed box of figure 7.2A and the recovered lifetimes are presented in figure 7.2C. The lifetime is homogenous and the same for the ESA feature above the diagonal as well as the SE and GSB feature below the diagonal. Figure 7.2D is a histogram of the recovered lifetimes, giving an estimate of 2.7 $\pm$ 1.0 ps. The same analysis is performed in figure 7.9 on the LH1-only cells acquired with 17.6 μJ/cm^2 yielding a lifetime of 4.7 $\pm$1.3 ps for energy transfer from LH1 to LH1.

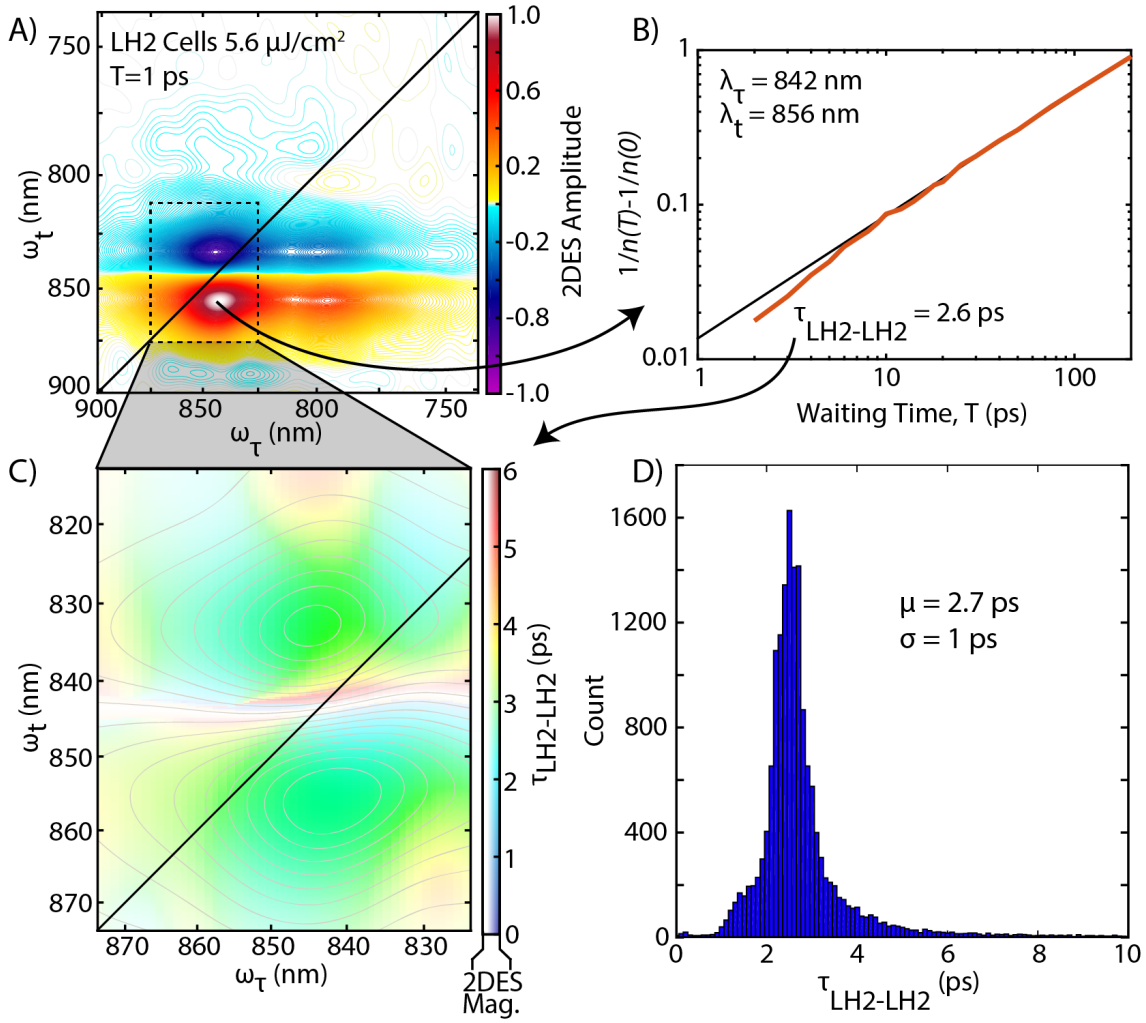

Figure 7.2: *A)* Absorptive 2DES spectrum of LH2-only cells at T = 1ps collected at 5.6 μJ/cm^2. The dashed box is analyzed further for the lifetime of energy transfer between LH2 complexes. *B)* Waiting time dynamics from the maximum ground state bleach and stimulated emission feature presented following equation 7.3, where the 2DES intensity is $n(T)$. The intercept of the linear relationship is used to retrieve the annihilation rate, γ_0, which is used to recover the hopping time, τ_{hop}, given in equation 7.1. *C)* Color map of the recovered τ_{hop}. The contours and saturation of the color is given by the intensity of the 2DES signal at 1 ps. *D)* Histogram of the lifetimes recovered in *C)* giving a mean of 2.7 ps for the lifetime of energy transfer between LH2s.

7.2 Wild Type Dynamics

Despite the well-connected networks of LH2 observed in the mutant cells, annihilation was only observed at the highest excitation power in the wild type cells and appeared in both LH2 and LH1. This lack of annihilation at lower powers indicates rapid transfer to LH1 and trapping via the RC. The next highest power, 5.6 μJ/cm^2, had dynamics consistent with data collected at 3.6 and 2.2 μJ/cm^2 and thus showed no annihilation. The data at 5.6 μJ/cm^2 were used to determine timescales for energy transfer from LH2 to LH1 and LH1 to the RC. Figure 7.3*A* shows waiting time traces from the peak intensity of ground state bleach and stimulated emission of LH2 and LH1 in the wild type cell data. These traces were fit to a biexponential function of the form

$$y = a_1 e^{(-t/\tau_1)} + a_2 e^{(-t/\tau_2)} + a_3 \tag{7.4}$$

The dynamics of LH2 and LH1 in the wild type cells are not simple. In addition to energy transfer dynamics from LH2 to LH1, both complexes have vibrational and intraband exciton relaxations. LH2 has an additional energy transfer process from B800 to B850 taking place on a 700 fs timescale and there is significant spectral overlap of LH2 and LH1 in the 2DES spectra, see figure 7.5. Figure 7.3*B* shows the value of τ_1 after fitting the entire 2DES spectrum to equation 7.4. The lifetime centered on the ground state bleach and stimulated emission feature at $\lambda_\tau = 842$ nm, $\lambda_t = 856$ nm as well as the excited state absorption feature directly above that correspond to the decay of signal from LH2. The neighboring lifetimes of ≈1-3 ps were smaller in amplitude and are consistent with vibrational relaxation observed in LH1. We can follow the flow of energy from LH2 into LH1 by observing the growth of a cross peak centered at $\lambda_\tau = 842$ nm, $\lambda_t = 880$ nm, figure 7.5 wild type time series. The growth of this cross peak and its spectral location is indicative of energy that was initially absorbed in the B850 band of LH2 transferring to the B875 band of LH1 resulting in the ground state bleach and stimulated emission at $\lambda_\tau = 842$ nm, $\lambda_t = 880$ nm. We therefore

assign the energy transfer time from LH2 to LH1 to be 4.8 ± 0.5 ps as shown in figure 7.3*D*. Figure 7.3*C* shows the second lifetime from equation 7.4. This lifetime, following the same analysis above, of 49 ± 6 ps corresponds to the trapping time via the RC, figure 7.3*E*. This transfer time competes with the intrinsic lifetime of LH1 in the absence of the RC, which can be determined from the low power 2DES of LH1-only cells. The lifetime of LH1 when fit to equation 7.4 without the offset parameter, a_3, was determined to be 264 ± 15 ps, Figure 7.10 and the red histogram in figure 7.3*E*.

7.3 Membrane Modeling

Table 7.1 shows a summary of the recovered energy transfer times between complexes. From this information as well as the lifetime of LH1, we can construct model membrane fragments and compare the population of excited states to the experimental data. The model membranes for LH1 and LH2 only cells were constructed assuming hexagonal close packed complexes with varying domain sizes and internal lifetimes. The membranes were randomly populated according to the excitation fluences used in experiments. The excitations then underwent a random walk on the membranes using the recovered lifetimes for energy transfer. Annihilation was simulated when one complex received two or more excitations at a time by reducing the number of excitations to one. Figures 7.1 and 7.6 shows the best fit to experimental results after sampling LH2 and LH1 lifetimes and domain sizes. The best fit for both occurred with an excited state lifetime of 250 ps, consistent with the lifetime recovered in LH1 only cells at low power. LH2-only cells were found to have a domain size of 64 complexes and LH1 was found to have a domain size of 20 complexes. Figure 7.11 shows results from the LH2 and LH1 models with different domain sizes, but a fixed excited state lifetime of 250 ps. The same modeling can be done for the WT cells. A domain size of 10 LH1 complexes was chosen to be consistent with separate AFM studies. [7, 15] The relative ratio of LH2 and LH1 was set to be 1.8:1 based on the linear absorption spectrum, see figure 7.8, and the back transfer rate from LH1 to LH2 was set to be 100 ps as this

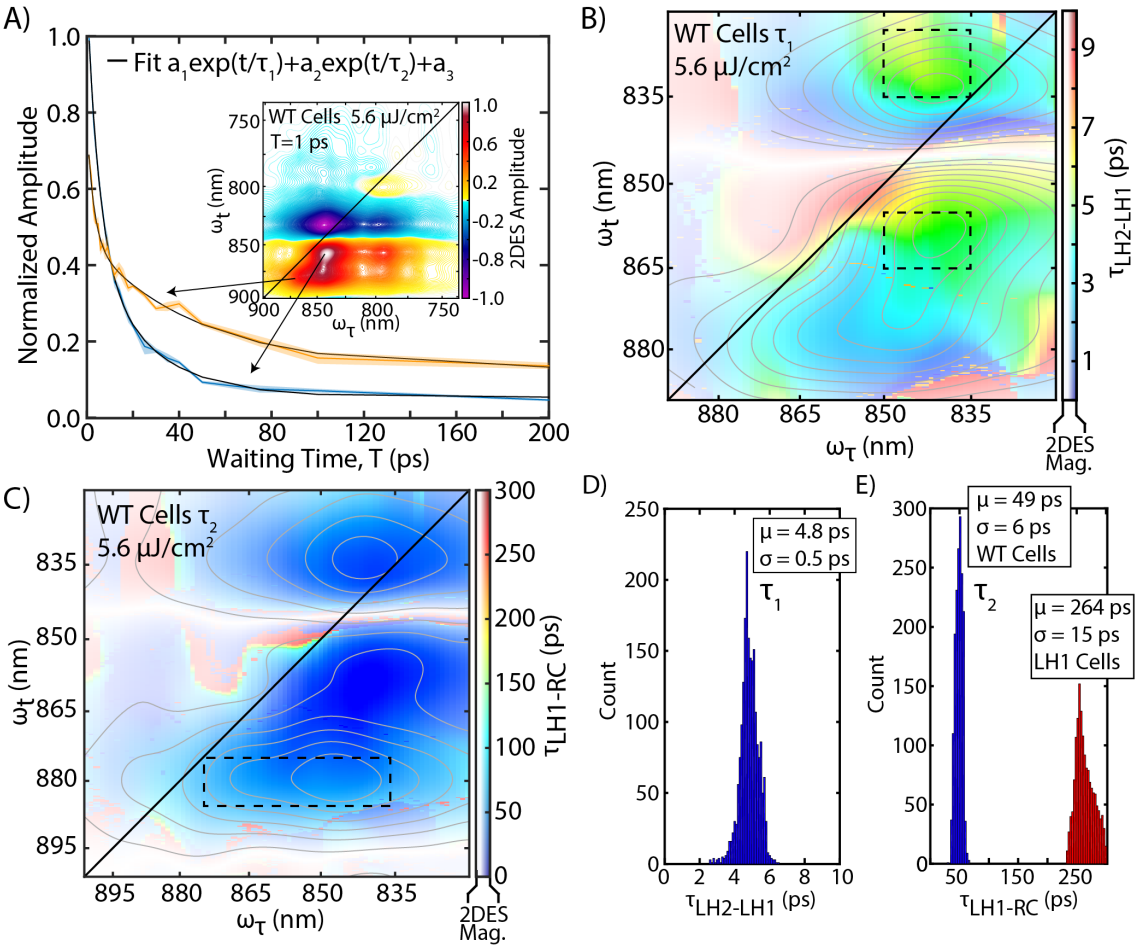

Figure 7.3: *A)* Waiting time traces taken from the peak locations of ground state bleach and stimulated emission of LH2 (blue) and LH1(orange) in the wild type *Rba. sphaeroides*. The 2DES spectra were normalized to 1 ps and fit to a biexponential function. *B)* Color map of the first lifetime from the biexponential fit. This lifetime in the region of LH2 corresponds to the energy transfer from LH2 to LH1. The saturation of the color as well as the gray contours is given by the intensity of the 2DES spectrum at T= 1 ps. *C)* Same as *B)* except for the second lifetime in the biexponential fit and the saturation and contours are coming from T= 50 ps map and the lifetime corresponds to LH1-RC energy transfer. *D)* Histogram of the lifetimes within the dashed boxes of *B)*. These lifetimes corresponds to LH2→ LH1 transfer times. *E)* Histogram of the lifetimes within the dashed box of *C)*. These lifetimes corresponds to LH1→ RC transfer.

Complex-Complex τ_{hop} (ps)	
LH2→ LH2	2.7 ± 1.0
LH2→ LH1	4.8 ± 0.5
LH1→ LH1	4.7 ± 1.3
LH1→ RC	49 ± 6

Table 7.1: Energy transfer times between complexes recovered from annihilation studies in mutant *Rba. sphaeroides* and biexponential fits to low power scans in wild type *Rba. sphaeroides*.

matched fluorescence spectrum. The LH1 domains were surrounded by 18 LH2s to yield the model membrane shown in figure 7.4. This model initially yielded poor agreement with the experimental results. Only after closing 80% of the reaction centers did simulation and experiment become more consistent, see figure 7.7. The closing of the majority of reaction centers is consistent with the need for an offset parameter in the biexponential fitting of the wild type bacteria and is indicative of multiple laser excitations in the same sample volume at these sample flow rates. When all the RCs are open and a single excitation is placed in a random LH2 the model yielded an efficiency of trapping via an RC of 83.9%. 14.5% of the excitations were dissipated via fluorescence from LH1 and 2.6% were dissipated via fluorescence from LH2. Figure 7.4 shows 3 of the 1000 simulated trajectories. Energy transferred rapidly from LH2 to LH1, on average only taking 5.6 transfers between LH2. The exciton spent the majority of the time before trapping or fluorescing exploring the LH1 domain, taking an average of 29 hops between LH1. Despite the 100 ps lifetime for back transfer, on average there was one transfer from LH1 to LH2 per trajectory,

Here we have demonstrated the ability to monitor energy transfer in a living system and recover membrane architecture in near real time. These improvements open new possibilities for probing photosynthetic systems. Organisms are inherently dynamic and adapt to their environment, but often times their dynamics and responses to external conditions depend on them being alive. Photosynthetic organisms are no exception. For instance, photoprotective mechanisms, such as non-photochemical quenching and state transitions, alter ultrafast energy transfer pathways and membrane architecture in living systems in response to oxidative

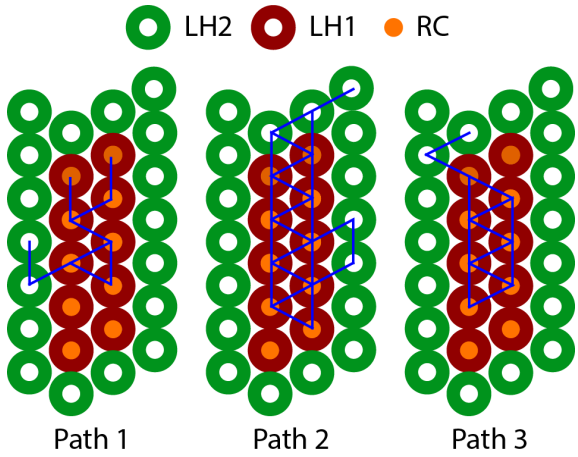

Figure 7.4: Model of the functional photosynthetic unit and three representative simulated trajectories for the initial conditions of a single excitation in LH2 with all RCs open.

stress, high light, and dehydration. Many questions remain on exactly how the dynamics, coupling, and architecture change under different stresses. The advances presented here are the next step towards a deeper understanding of ultrafast energy transfer in photosynthetic systems, its regulation, and its architecture.

7.A Supporting Figures

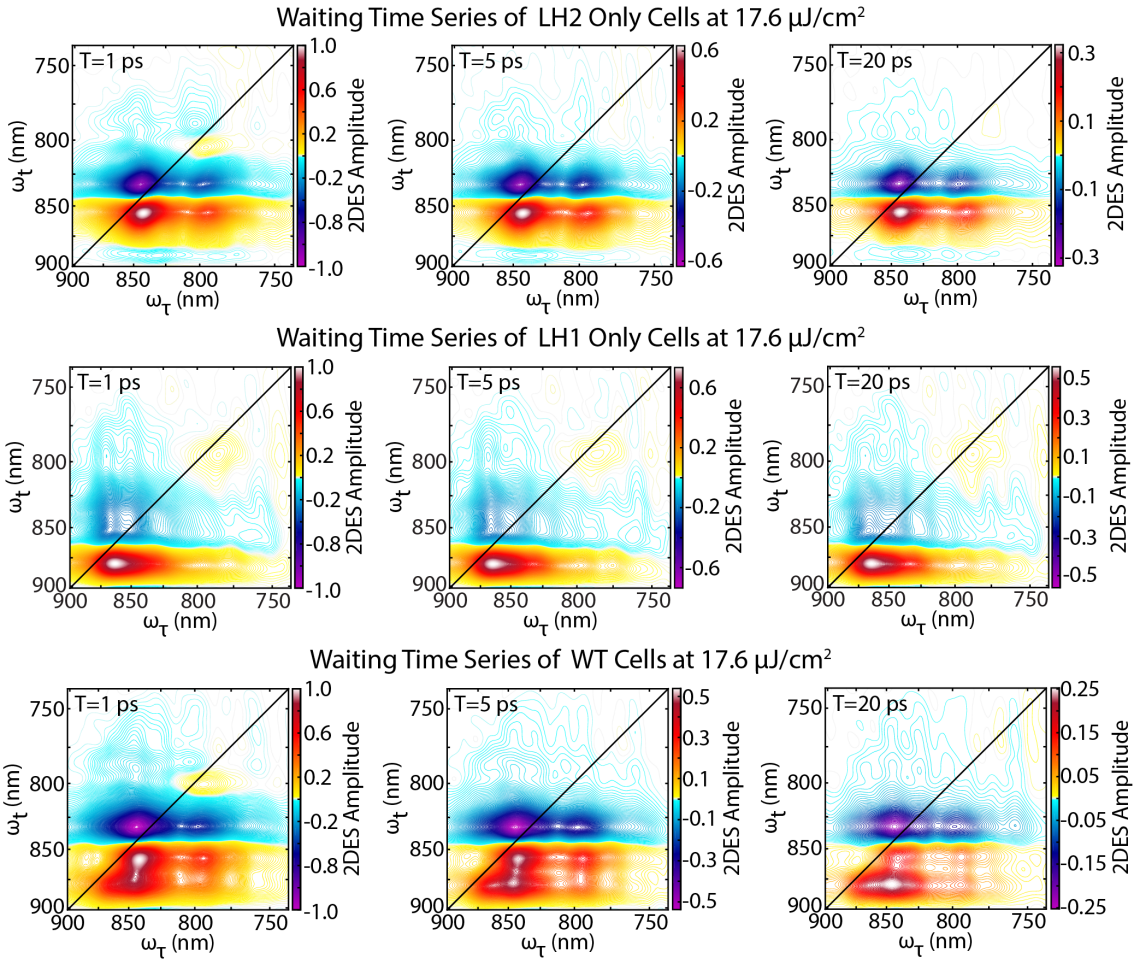

Figure 7.5: *(top)* Absorptive spectra waiting time series from LH2-only cells *middle* LH1-only cells *bottom* wild type cells (bottom) taken at 17.6 μJ/cm^2. The spectra show significant overlap between LH2 and LH1 as well as clear energy transfer cross peaks between LH2 and LH1 in the wild type cells at T= 5 ps and T= 20 ps.

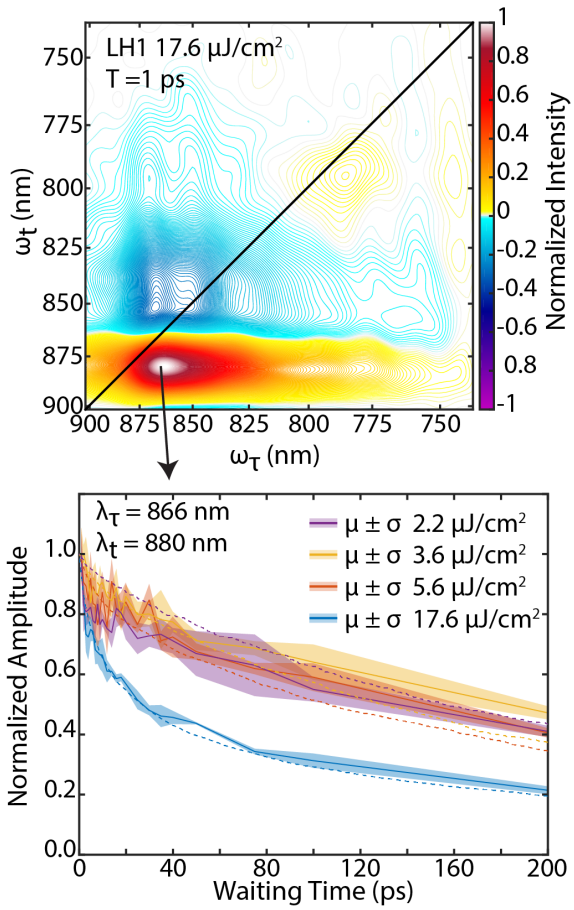

Figure 7.6: *top* Absorptive 2DES spectrum of LH1-only cells taken with 17.6 μJ/cm^2 at T= 1 ps. *bottom* Waiting time traces taken from the spectral location indicated by the black diamond above from spectra acquired at different powers. The traces are the average of 3 scans and the shaded background is the $\pm$ the standard deviation. The change in dynamics with power is indicative of exciton-exciton annihilation. The dashed lines show agreement to a model membrane with LH1 domain sizes of 20 complexes, a transfer time of 4.7 ps, and an excited state lifetime of 250 ps.

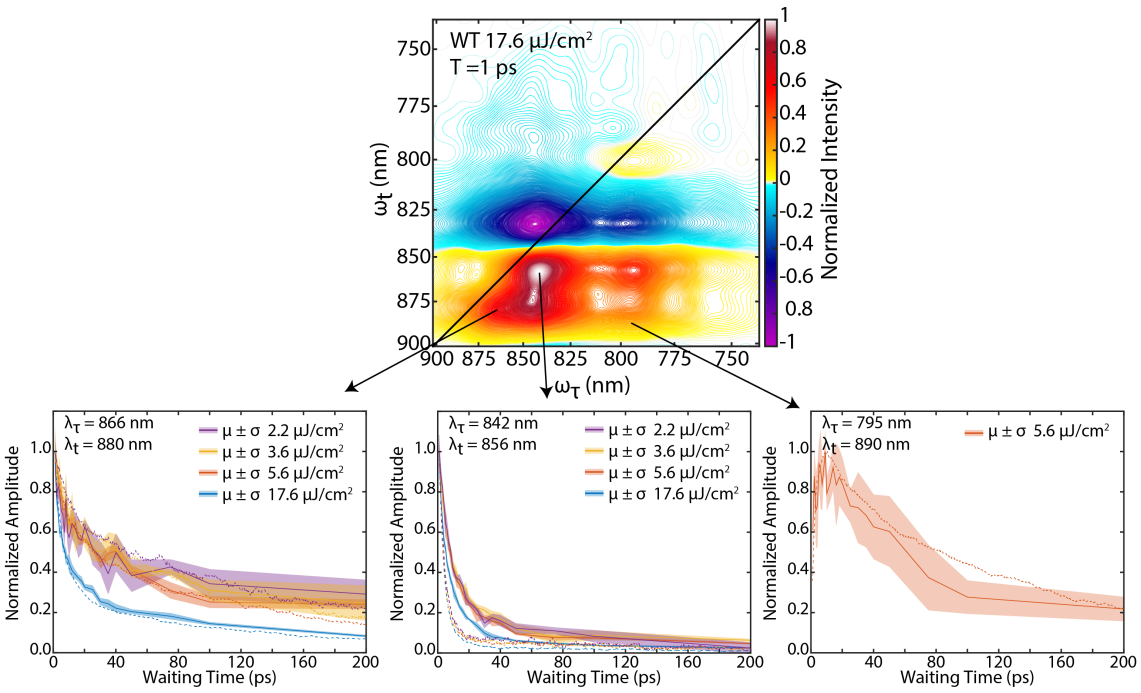

Figure 7.7: *top* Absorptive 2DES spectrum of wild type cells taken with 17.6 μJ/cm^2 at T= 1 ps. bottom Waiting time traces taken from the spectral locations indicated by the arrows from spectra acquired at different powers. The traces are the average of 3 scans and the shaded background is the $\pm$ the standard deviation. The change in dynamics with power is indicative of exciton-exciton annihilation. The dashed lines show agreement to a model membrane with 18 LH2 complexes embedded with LH1-RC domains of 10 complexes and 80% of the RCs closed.

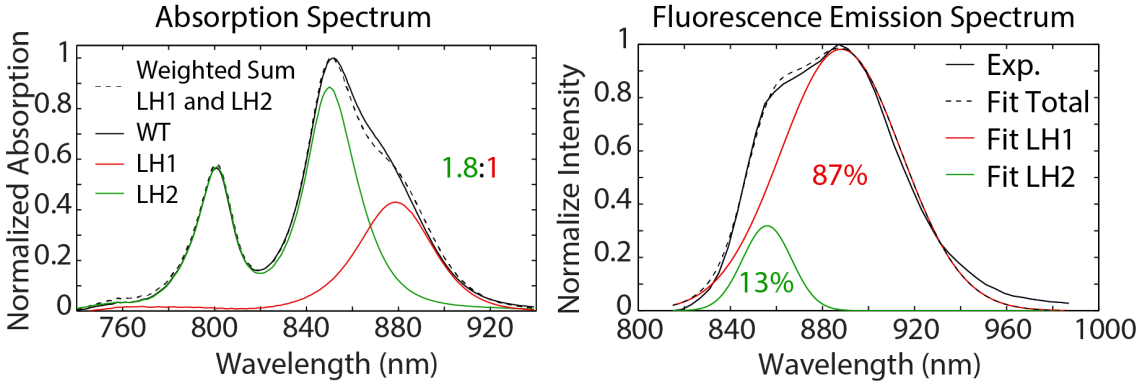

Figure 7.8: *Left)* Absorption spectrum of WT, LH1-only, and LH2-only cells with the scatter removed by fitting a quadratic function to long wavelengths. The dashed line is the result of a weighted sum fit to the WT absorption spectrum revealing a ratio of 1.8 LH2 to LH1. *Right)* Fluorescence emission spectrum from WT cells excited at 800 nm. The relative ratio between fluorescence intensity o LH2 and LH1 was determined by fitting two Gaussian functions to the spectrum and revealed about 13% of fluorescence was from LH2. This ratio was used to constrain the back transfer rate from LH1 to LH2 to be on the order of 100 ps.

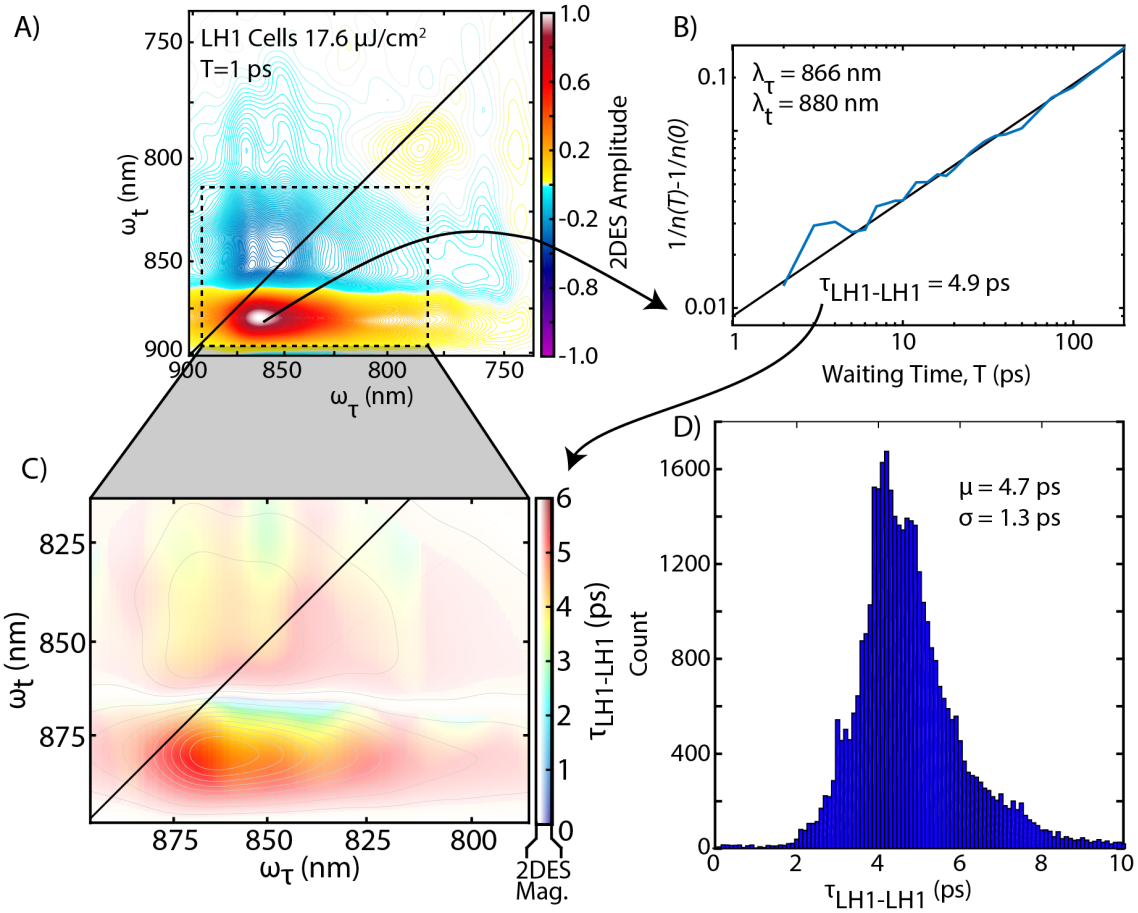

Figure 7.9: *A)* Absorptive 2DES spectrum of LH1-only cells at T = 1ps collected at 17.6 μJ/cm^2. The dashed box is analyzed further for the lifetime of energy transfer between LH1 complexes. *B)* Waiting time dynamics from the maximum ground state bleach and stimulated emission feature presented following equation 7.3, where the 2DES intensity is $n(T)$. The intercept of the linear relationship is used to retrieve the annihilation rate, γ_0, which is used to recover the hopping time, τ_{hop}, given in equation 7.1. *C)* Color map of the recovered τ_{hop}. The contours and saturation of the color is given by the intensity of the 2DES signal at 1 ps. *D)* Histogram of the lifetimes recovered in *C)* giving a mean of 4.7 ps for the lifetime of energy transfer between LH1s.

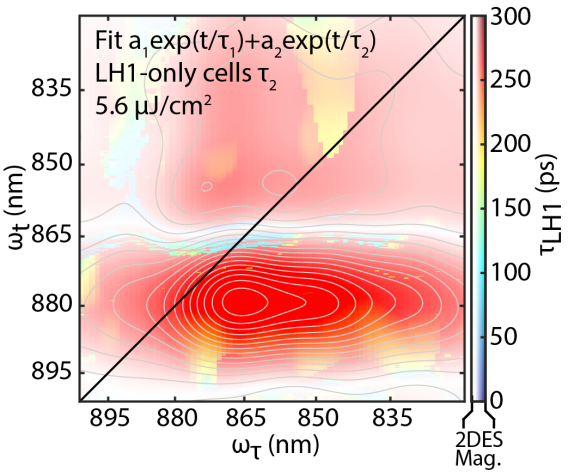

Figure 7.10: Color map of the second lifetime from the bi-exponential fit. This lifetime in the LH1-only cells corresponds to the lifetime of the excited state in LH1 in the absence of the RC trap. The saturation of the color as well as the gray contours is given by the intensity of the 2DES spectrum of LH1-only cells at T= 50 ps as are the gray contours.

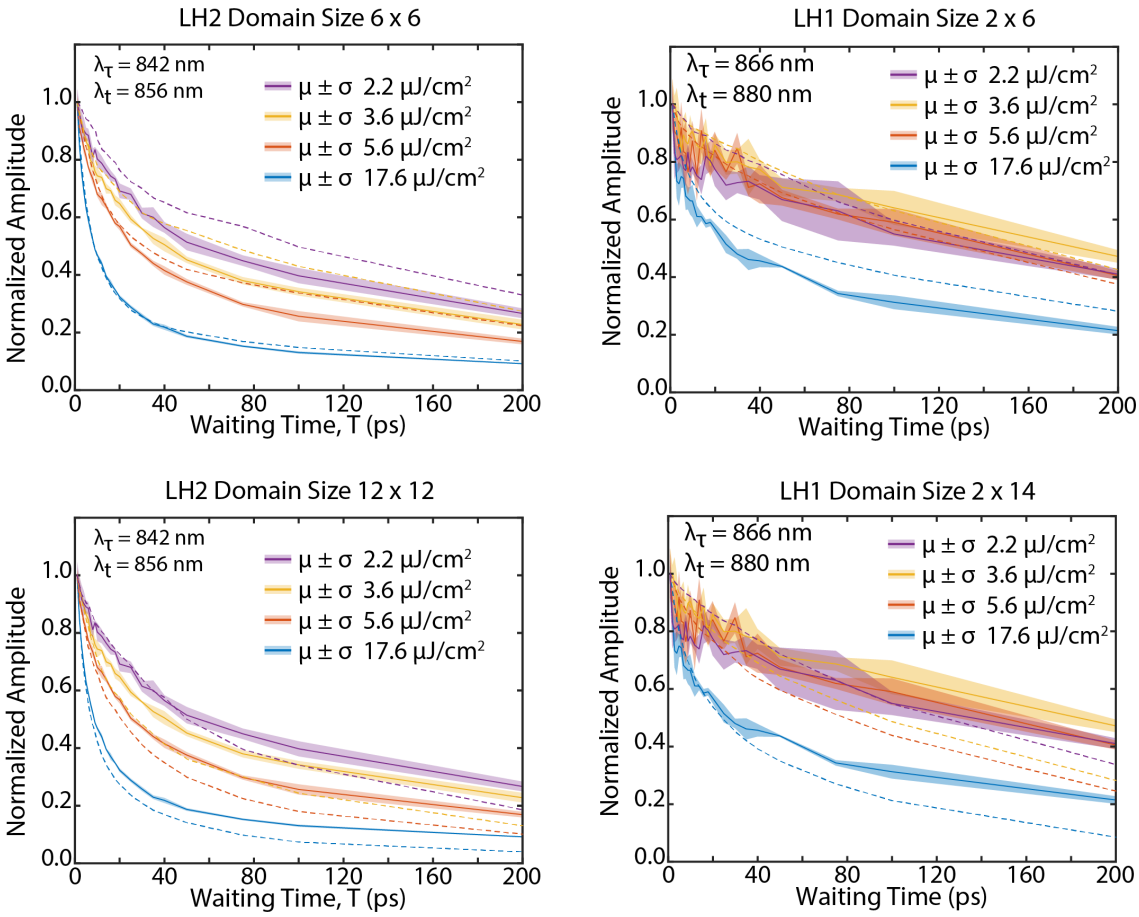

Figure 7.11: Comparison experimental data to kinetics recovered from model membranes with varying domain sizes in LH2 and LH1 only cells. The clear deviation from the model is indicative of the tight constraint on domain sizes in both LH2 and LH1 only cells.

REFERENCES

[1] J. R. Lakowicz. *Principles of fluorescence spectroscopy.* Springer, New York, New York, 2006.

[2] R. E. Blankenship. *Molecular mechanisms of photosynthesis.* Blackwell Science, Malden, Massachusetts, 2002.

[3] P. Muller, X. P. Li, and K. K. Niyogi. Non-photochemical quenching. a response to excess light energy. *Plant Physiology*, 125(4):1558–1566, 2001.

[4] R. Goss and B. Lepetit. Biodiversity of npq. *Journal of Plant Physiology*, 172:13–32, 2015.

[5] R. Berera, I. H. M. van Stokkum, M. Gwizdala, A. Wilson, D. Kirilovsky, and R. van Grondelle. The photophysics of the orange carotenoid protein, a light-powered molecular switch. *Journal of Physical Chemistry B*, 116(8):2568–2574, 2012.

[6] D. E. Chandler, J. Strumpfer, M. Sener, S. Scheuring, and K. Schulten. Light harvesting by lamellar chromatophores in *Rhodospirillum photometricum*. *Biophysical Journal*, 106(11):2503–2510, 2014.

[7] M. Şener, J. Strümpfer, J. A. Timney, A. Freiberg, C. N. Hunter, and K. Schulten. Photosynthetic vesicle architecture and constraints on efficient energyharvesting. *Biophysical Journal*, 99(1):67–75, 2010.

[8] R. Berera, R. van Grondelle, and J. T. M. Kennis. Ultrafast transient absorption spectroscopy: principles and application to photosynthetic systems. *Photosynthesis Research*, 101(1-3):105–118, 2009.

[9] T. Brixner, J. Stenger, H. M. Vaswani, M. Cho, R. E. Blankenship, and G. R. Fleming. Two-dimensional spectroscopy of electronic couplings in photosynthesis. *Nature*, 434(7033):625–628, 2005.

[10] J. Dostál, J. Pšenčík, and D. Zigmantas. In situ mapping of the energy flow through the entire photosynthetic apparatus. *Nature Chemistry*, 2016.

[11] H. van Amerongen, L. Valkunas, and R. van Grondelle. *Photosynthetic excitons*. World Scientific, River Edge, N.J., 2000.

[12] M. Vos, R. J. van Dorssen, J. Amesz, R. van Grondelle, and C. N. Hunter. The organization of the photosynthetic apparatus of *Rhodobacter sphaeroides* - studies of antenna mutants using singlet singlet quenching. *Biochimica et Biophysica Acta (BBA) - Bioenergetics*, 933(1):132–140, 1988.

[13] V. Barzda, V. Gulbinas, R. Kananavicius, V. Cervinskas, H. van Amerongen, R. van Grondelle, and L. Valkunas. Singlet-singlet annihilation kinetics in aggregates and trimers of lhcii. *Biophysical Journal*, 80(5):2409–2421, 2000.

[14] S. E. Bradforth, R. Jimenez, F. van Mourik, R. van Grondelle, and G. R. Fleming. Excitation transfer in the core light-harvesting complex (lh1) of *Rhodobacter sphaeroides* - an ultrafast fluorescence depolarization and annihilation study. *Journal of Physical Chemistry*, 99(43):16179–161912, 1995.

[15] S. Bahatyrova, R. N. Frese, C. A. Siebert, J. D. Olsen, K. O. Van Der Werf, R. Van Grondelle, R. A. Niederman, P. A. Bullough, C. Otto, and C. N. Hunter. The native architecture of a photosynthetic membrane. *Nature*, 430(7003):1058–1062, 2004.

[16] A. Bunde and S. Havlin. *Fractals and disordered systems*. Springer, New York, New York, 1996.

CHAPTER 8

FUTURE DIRECTIONS

8.1 Improvements To GRAPES

The development of GRAPES in this thesis and its application to *Rba. sphaeroides* has proven the technique's capabilities and opens the door to new opportunities in the study of energy transfer in photosynthesis. [1–3] The utility of GRAPES is to observe real time changes in the energy transfer pathways that occur during photoprotection. Though photoprotective mechanisms have been observed in *Rba. sphaeroides* they are substantially weaker than the effects observed in green algae, plants, and cyanobacteria. [4, 5] Several attempts were made to observe these mechanisms in *Rba. sphaeroides*, but all yielded inconclusive results. In this Chapter I will discuss improvements that can be made to the instrument to expand its capabilities and simplify its use. I will also elaborate on the use of GRAPES to study photoprotection in algae, plants, and cyanobacteria.

8.1.1 Bandwidth

The bandwidth of the GRAPES instrument has doubled every few years and with each expansion we have been able to see new and interesting dynamics. [1, 3, 6, 7] Currently the bandwidth is sufficiently broad for working with purple bacteria in the Bchl *a* Q_y band, but as we move from purple bacteria and into cyanobacteria, algae, and plants the bandwidth must be expanded. Currently we generate our bandwidth via filamentation in argon gas. The pressure of this gas has changed over the years, but is typically between 2 and 20 psi above atmospheric. The filamentation is achieved by focusing in the argon. [8] However superior bandwidth has been achieved using multiple filamentation processes. [9] I have explored two filamentation steps using the optical design in Figure 8.1. This optical design yields a bandwidth that is sufficiently large for the study of cyanobacteria, algae, and plants. Figure

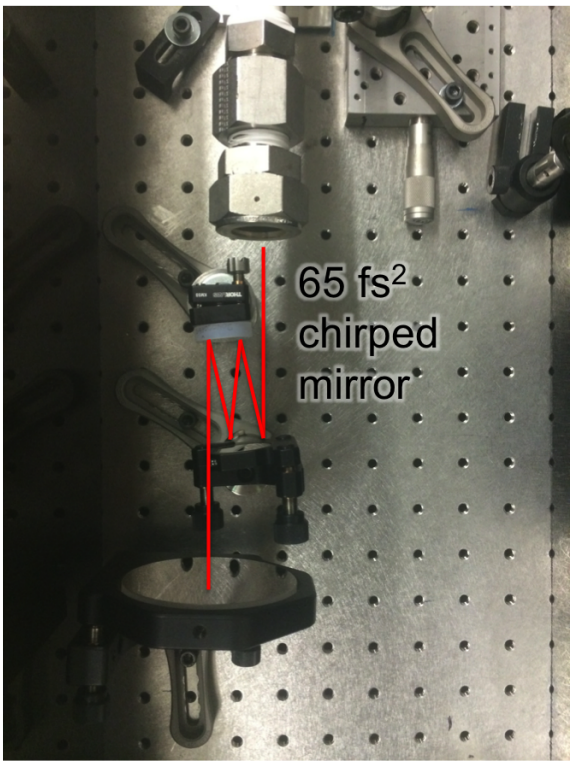

Figure 8.1: Double filamentation process in argon gas. A pair of chirped mirrors are used to recompress the pulse before sending it back through the argon gas.

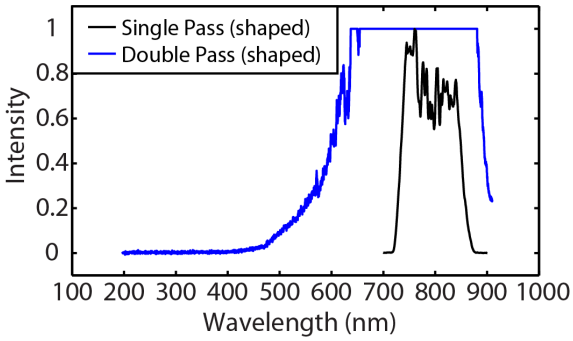

Figure 8.2: Spectrum generated by one (black) and two (blue) filamentation steps in argon gas at 4 psi.

8.2 shows a comparison between a single and a double pass of argon gas after shaping the spectra to 10 % of the maximum intensity.

The optical setup in figure 8.1 produces a small beam profile after the argon gas. This intense beam will quickly ablate the chirped mirrors surface. I recommend using 130 fs^2 chirped mirrors and placing the chirped mirrors farther back. Using 130 fs^2 chirped mirrors will require half the number of bounces and will make it easier to propagate a large diameter beam that will not damage the chirped mirrors. After the second filamentation process an additional 260 fs^2 of chirp should be compensated for to account for the window on the other end of the argon tube.

8.1.2 Real Time Processing

Labview is a "language" that was made for the purpose of instrument control and acquisition. Every instrument in this thesis is controlled almost exclusively through homemade Labview software. This does not mean that Labview is limited to TTL triggers and shutters. It has long been my hope that we would write real time 2D processing software in Labview that would allow us to monitor 2DES signals during acquisition. Similar software has already been construced by Graham Norris and Lane Gunderman for control of the ultrafast pump-probe instrument described in Section 2.3.1 and the code is given in the digital supplement. The analysis for 2DES is not all that different from the analysis required in pump-probe. In very broad strokes it is simply some Fourier transforms, Window functions, and permutations. The software for the ultrafast pump-probe performed these transforms on matrices that were 2048x16384, substantially larger than the images acquired by GRAPES of 1280x504. The current problem with real time processing is the fast camera, Phantom Miro, does not stream off data at the acquisition rate, rather it streams which ever frame was last acquired when queried for a frame and it reduces the bit depth to 8 bit. Because we have seen a significant improvement in the signal to noise as we have reduced the rate of signal acquisition we should likely switch to a slower camera, one with frame rates ranging from 0.1 to 100 Hz. The camera would need a fast global shutter, usually these are electronic, that effectively stops acquisition during the readout of the sensor and will avoid a rolling shutter effect that would lead to different coherence times acquiring a different numbers of laser shots. The Zyla 5.5 CMOS is an effective alternative to the Phantom Miro. Frames can be read over USB at 40 Hz and the camera has a global shutter that can close the sensor in 0.1 μs, significantly faster than we need. The triggering for the camera is complex and requires precise timing. I also recommend getting a programable delay generator, such as the SRS 535 used in Section 2.2 to gate the camera and synchronize the camera with the chopper and laser.

8.1.3 77 K GRAPES

Collecting 2DES spectra on cryogenic samples produces narrower lineshapes and resolves electronic structure that may be obscured by thermal disorder. A significant problem when freezing samples to cryogenic temperatures is that they often produce highly scattering ice crystals, much like the frosted appearance of ice cubes made in a home freezer. In order to mitigate this problem the sample is often first diluted in glycerol. When these samples are frozen they produce surface (often called a glass) that is not frosted, but instead, has large cracks. It was believed that these large cracks would prevent the acquisition of 2DES data on cryogenic samples using GRAPES because the coherence time, which is encoded in a vertical line on the sample, would not be uniform due to the cracks.

A test was performed using isolated LH2 from heterotrophically grown cells. The sample was concentrated to an OD of ≈0.8 at 850 nm in a 200 μm cuvette before being diluted 3:1 with glycerol. Figure 8.3 shows the absolute value rephasing spectrum and is the first 2DES data on cryogenic samples acquired with GRAPES. The cryogenic sample did form numerous cracks, however they did not limit the signal acquisition. It is clear from figure 8.3 that the features are significantly narrowed from those observed in Chapters 4 and 5 as expected, but the test did present some future challenges to making GRAPES work well with cryogenic temperatures. At low temperatures the quantum coherences present during the coherence time last much longer than at room temperature due to a decrease in the thermal disorder that causes dephasing. At room temperature these coherences only last ≈ 50 fs at cryogenic temperatures they can last several hundred fs. [10] Because GRAPES encodes the coherence time delay spatially using gaussian beams the beams spatial profile inherently produces an instrument response that ehances some coherence times relative to others. The spatial profile of beam 3 at the focus and the instrument response function that the profile produces can be seen in figure 8.4. The FWHM of the instrument response function in coherence time is only 220 fs. There are two potential solutions to increase the span of coherence times acquired with GRAPES. The angle between beams one and two

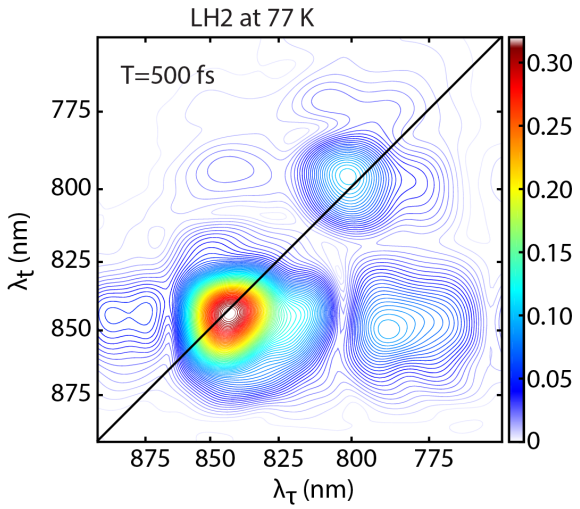

Figure 8.3: Absolute value rephasing spectrum of LH2 at T=500 fs taken at 77 K

can be increased, or the beams can be expanded. The first solution will result in a decrease in signal to noise for the equivalent excitation power because there will be fewer coherence time steps over the same time range. The latter solution will result in a tighter focus in the horizontal and an enhanced signal to noise for the equivalent excitation power. The smallest mirror in the GRAPES apparatus has a spatial extent of 1 cm. Because the FWHM of the beams is currently only 1.9 mm the beams could be expanded by a factor of 3. This would result in a clipping of only 4% of the beam intensity, but would allow sampling of 660 fs of coherence time. This range of coherence times should be sufficient for cryogenic samples without sacrificing signal to noise.

8.2 Routes To The Observation Of Photoprotection

Algae, plants, and cyanobacteria all have photo protective mechanisms that are labelled as non-photochemical quenching (NPQ). When no photo protective mechanisms are being employed by an organism all the light that it aborbs (to a good approximation) is either fluoresced or trapped and quenched in the RC. NPQ adds additional pathways to dissipate energy and therefore changes the fluorescence yield. NPQ is often studied by monitoring changes to fluorescence, but this has significant limitations. Fluorescence does not provide information on the path that energy took from the absorber to the emitter and if fluorescence

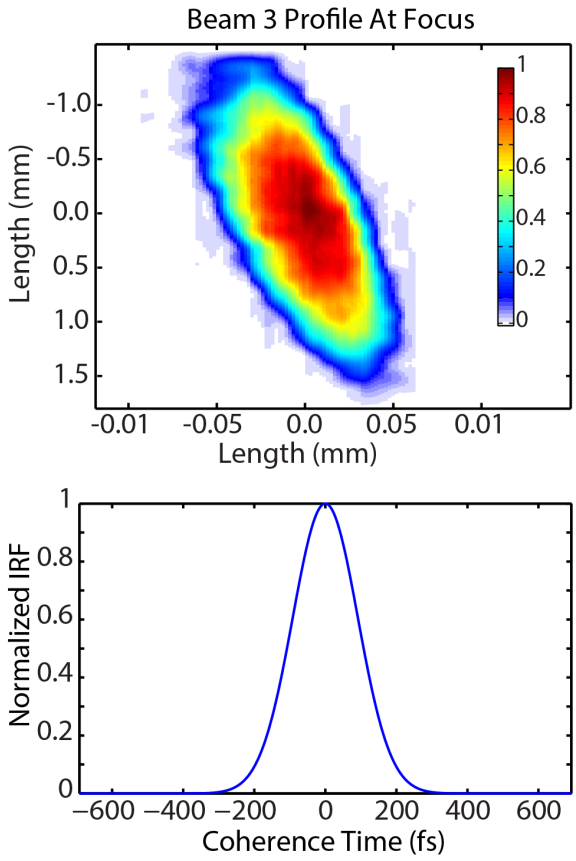

Figure 8.4: *(Top)* Beam 3 intensity profile at the sample position as measured by a webcam that was at a slight angle (note the axes are not equal). The beam is focused to a line that is $\approx$ 50 μm FWHM from horizontally and 1.9 mm FWHM vertically. *(Bottom)* The limited spatial extent of the beams distorts the signal by producing a non-uniform instrument response function in τ. The FWHM of the instrument response function is 220 fs.

disappears, it does not inform where the excitation went instead. GRAPES can give all the path information in a living system and is sensitive to dark states that do not exhibit fluorescence, such as those found in carotenoids. [11]

NPQ encompasses numerous different processes with different triggers that all have the same result of diminished chlorophyll fluorescence. Quenching in NPQ is divided into three different types, q_E, q_I, and q_T. [5] q_E is the process that directly quenches chlorophyll excited states, q_I is the inhibitory quenching related to gene regulation and photo damage, q_T are state transitions that alter the architecture of the photosynthetic membrane. [12, 13] Each of these types of quenching changes the energy transfer pathways taken by excitations, but the only observables currently, are related to the fluorescence, both its intensity, spectrum, and dynamics.

As we begin to explore photoprotection there are two choices that we need to make. What organism should we study? and what aspect of NPQ should we study in that organism?

Here I discuss several model NPQ systems that have open questions on their molecular mechanisms.

8.2.1 Cyanobacteria And The Orange Carotenoid Protein

In Cyanobacteria light harvesting is done by phycobilisomes. At the core of the phycobilisome is a trimer of allophycocyanin (APC660) that transfers energy to the PSII reaction center. The process of q_E is dominated by a protein called the "orange carotenoid protein" (OCP) and its regulated coupling to the APC660 trimer. The absorption spectrum of a cyanobacterium *Synechococcus leopoliensis* UTEX 625 is shown in figure 8.5. Under 450 nm excitation or intense white light the carotenoid embedded in OCP undergoes a conformational change that puts OCP in its active (quenching) state. [14, 15] When active, OCP is believed to couple to APC660 and absorb energy from a billin in the APC660 trimer and dissipate that energy as heat. This can be seen in a time series of the fluorescence spectra in figure 8.5. The timescales for these changes are well suited for GRAPES, occurring on roughly a minute time scale, and could be induced by illuminating the sample volume using an LED that emits at 450 nm (Thorlabs M450LP1). If the bandwidth described in Section 8.1.1 is achieved, many interesting pathways should be observable. In low-light, energy transfer from OCP to APC660 and the phycobilisome maybe visible as a cross peak between 500 nm and 650 nm. There should also be clear energy transfer peaks between the phycobilisome and the RC. Under high-light conditions there should be a decrease in the cross peak between OCP and the phycobilisome. As energy shifts to transferring into OCP from APC660 there should be a growth of an ESA feature arising from the carotenoid in OCP. There should also be a decrease in the cross peak between the phycobilisome and the RC with time as state transitions modify the membrane architecture to decouple the phycobilisome antenna from the RC.

Experiments monitoring changes in energy transfer pathways can be conducted in two different ways. A series of waiting time spectra could be acquired allowing for the observation

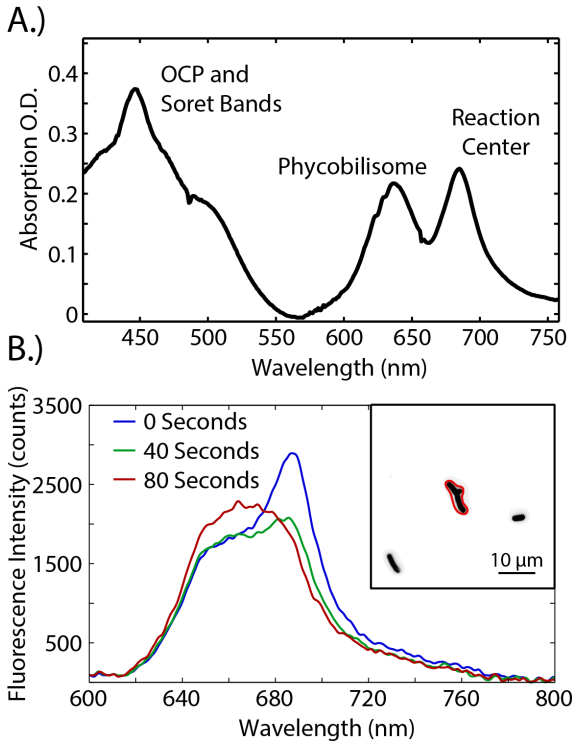

Figure 8.5: *(Top)* Absorption spectrum of *Synechococcus leopoliensis* UTEX 625. The features on the blue side of the spectrum correspond to absorption by OCP and the Soret bands of chlorophyll, the feature at 640 nm is largely due to the phycobilisome, and the feature at 680 nm is due to chlorophyll in the RCs. *(Bottom)* The fluorescence spectra of a small group of *Synechococcus leopoliensis* cells shown in the inset acquired using a hyper spectral fluorescence microscope. The series of spectra show NPQ changing the fluorescence over time. There is a decrease in the chlorophyll fluorescence as energy transfer to the RCs is turned off via OCP. As time continues there is an increase in the fluorescence of the phycobilisome possibly indicating some longer term NPQ mechanism such as q_T.

of changes in dynamics. This will be especially useful when observing carotenoid-chlorophyll transfer, which takes place on a sub 100 fs timescale and has the added complication that relaxation between the carotenoid S_2 and S_1 states occurs on a similar timescale. [11, 16] This method of data acquisition is what has been presented throughout the thesis, but data could also be acquired at a single waiting time and changes in the energetic coupling could be observed as a function of real time. Typically, data is acquired at a frame rate of 50 Hz and during data processing 25 frames are combined to remove scatter. This means that a unique 2DES spectra's acquired at a rate of ≈ 0.5 Hz. As the sample is perturbed, possibly with 450 nm excitation, the energetic coupling could be observed and its rates of change could be documented. This will likely give a similar timescale as the dynamics for fluorescence changes, but will be a direct measure of the energetic coupling in the system.

Amazingly, much of the NPQ induced by OCP can be reconstituted *in vitro*, [14] but the goal is to observe these dynamics in living systems. The observation of dynamics *in vivo* requires the growth and maintenance of cyanobacteria in the lab. Currently, the first cultures of *Synechococcus leopoliensis* UTEX 625 are being grown in the lab under the direction of

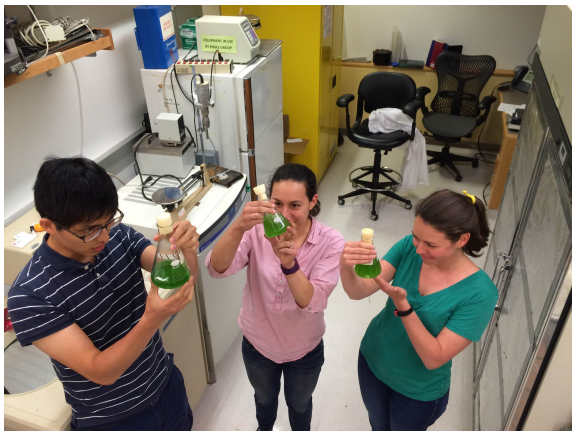

Figure 8.6: From left to right Po-Chieh Ting, Sara Hess, and Sara Massey holding cultures of *Synechococcus leopoliensis* UTEX 625 being grown photoautotrophically

Sara Sohail, see Figure 8.6.

Not all changes to the energy transfer pathways *in vivo* can be labelled as photoprotective. There are other interesting dynamic processes occurring *in vivo* that can produce changes. An interesting processes that modulates light harvesting is the circadian rhythm. There is a significant amount of expertise on campus in the lab of Mike Rust already exploring this in cyanobacteria and this might also provide a route to exploring real time changes in the energy transfer pathways. [17]

8.2.2 q_E and q_T In Green Algae

Green Algae and plants are eukaryotes that evolved following endocytosis events of cyanobacteria. They are substantially more complex than cyanobacteria, with intricate internal structures, multiple membranes with photosynthetic machinery, and they are much larger. Their size leads to enhanced problems associated with scattered light and in the case of plants will necessitate the use of sectioning techniques similar to those employed in electron microscopy. Both green algae and plants exhibit similar NPQ mechanisms and much of the observations in one would be translatable to the other. [5] Because the research is largely translatable, I suggest starting with green algae because much of the infrastructure worked out for *Rba. sphaeroides* and cyanobacteria will function with algae i.e. they can be flowed and the optical density and scatter can be adjusted by the cell density of the sample .

The model organism for green algae is *Chlamydomonas reinhardtii*. NPQ has been studied extensively in *C. reinhardtii* and the dominate process is known as the violaxanthin, antheraxanthin, zeaxanthin (VAZ) cycle or the Xanthophyll cycle. [5] Violaxanthin, antheraxanthin, and zeaxanthin are all carotenoids and their structures can be seen in figure 8.7. During the VAZ cycle excess light leads to the conversion of violaxanthin into zeaxanthin in LHCII through an enzyme V de-epoxidase. During high light V de-epoxidase removes the two epoxide groups from violaxanthin to produce zeaxanthin. This alteration extends the conjugation length and redshifts the absorption spectrum of zeaxanthin relative to violaxanthin. It is believed that this redshift lowers the carotenoid S_1 energy level below that of the Q_y energy level of the chlorophyll and transitions the carotenoid from an energy donor to an energy trap, thus producing q_E quenching, though this mechanism is still debated. [5] The GRAPES instrument is able to discern the mechanism of q_E by observing the ESA of the carotenoid S_1 state as well as the ground state bleach of the S_2 state if there is sufficient bandwidth.

The proton gradient across the thylakoid membrane is the most important activator of NPQ in plants and Algae. It triggers the enzyme V de-epoxidase to convert violaxanthin into zeaxanthin. Thus, one way to study this effect is to stress the algae with high-light conditions similar to the conditions proposed to study cyanobacteria. The intense light will induce a large membrane potential and drive the VAZ cycle. Another method to study this q_E mechanism is with the use of uncouplers. Uncouplers are chemicals that eliminate the membrane potential by making the membrane slightly porus to ions. Valinomycin is a common uncoupler and has been purchased for this experiment.

In addition to the VAZ cycle and q_E processes q_T processes are occurring in plants and algae. The most well known q_T processes is the aggregation of the LHCII antennas, which has been shown to both decouple the antennas from the reaction centers and decrease chlorophyll fluorescence. The protein PsbS has been shown to be essential for this aggregation process, but its role is not entirely clear. It is currently debated if PsbS is a quenching site

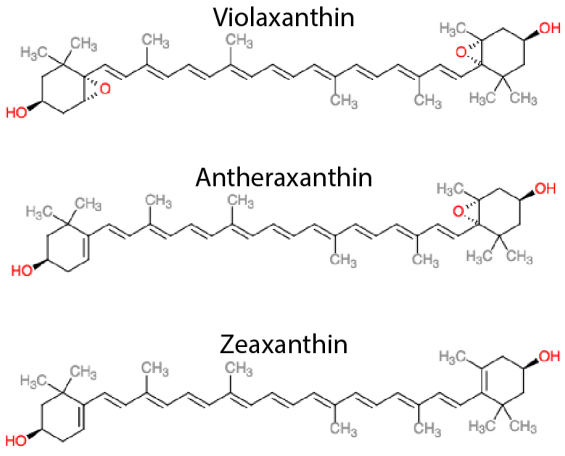

Figure 8.7: Structures of violaxanthin, antheraxanthin, and zeaxanthin from [11]. The structures differ in the removal of the two epoxide groups in violaxanthin to produce zeaxanthin. The removal of the epoxide groups extends the conjugation and redshifts the absorption spectrum.

(though it is not even clear what pigments are contained in PsbS [18]) or if PsbS is playing an indirect role in facilitating the aggregation. [19] In either case GRAPES could provide tremendous insight. In a manner similar to that of Chapter 7, GRAPES could be used to observe the coupling between antenna complexes and use annihilation to observe changes in their hopping times, possibly indicating aggregation without having to perform cryoelectron microscopy. GRAPES could also provide insight into what is quenching in LHCII aggregates, again through the observation of dark states via ESA and GSB.

REFERENCES

[1] P. D. Dahlberg, A. F. Fidler, J. R. Caram, P. D. Long, and G. S. Engel. Energy transfer observed in live cells using two-dimensional electronic spectroscopy. *Journal Of Physical Chemistry Letters*, 4(21):3636–3640, 2013.

[2] P. D. Dahlberg, G. J. Norris, C. Wang, S. Viswanathan, V. P. Singh, and G. S. Engel. Communication: Coherences observed in vivo in photosynthetic bacteria using two-dimensional electronic spectroscopy. *Journal of Chemical Physics*, 143(10):101101, 2015.

[3] P. D. Dahlberg, P. Ting, S. C. Massey, E. C. Martin, C. N. Hunter, and G. S. Engel. Electronic structure and dynamics of higher-lying excited states in light harvesting complex 1 from *Rhodobacter sphaeroides*. *The Journal of Physical Chemistry A*, 2016.

[4] V. Šlouf, P. Chábera, J. D. Olsen, E. C. Martin, P. Qian, C. N. Hunter, and T. Polívka. Photoprotection in a purple phototrophic bacterium mediated by oxygen-dependent alteration of carotenoid excited-state properties. *Proceedings of the National Academy of Sciences*, 109(22):8570–8575, 2012.

[5] R. Goss and B. Lepetit. Biodiversity of NPQ. *Journal of Plant Physiology*, 172:13–32, 2015.

[6] E. Harel, A. F. Fidler, and G. S. Engel. Real-time mapping of electronic structure with single-shot two-dimensional electronic spectroscopy. *Proceedings of the National Academy of Sciences*, 107(38):16444–16447, 2010.

[7] E. Harel, P. D. Long, and G. S. Engel. Single-shot ultrabroadband two-dimensional electronic spectroscopy of the light-harvesting complex lh2. *Optics Letters*, 36(9):1665–1667, 2011.

[8] N. Akozbek, M. Scalora, C. M. Bowden, and S. L. Chin. White-light continuum generation and filamentation during the propagation of ultra-short laser pulses in air. *Optics Communications*, 191(3-6):353–362, 2001.

[9] B. Spokoyny and E. Harel. Mapping the vibronic structure of a molecule by few-cycle continuum two-dimensional spectroscopy in a single pulse. *Journal of Physical Chemistry Letters*, 5(16):2808–2814, 2014.

[10] A. F. Fidler, J. R. Caram, D. Hayes, and G. S. Engel. Towards a coherent picture of excitonic coherence in the fennamatthewsolson complex. *Journal of Physics B: Atomic, Molecular and Optical Physics*, 45(15):154013, 2012.

[11] T. Polívka and V. Sundström. Ultrafast dynamics of carotenoid excited states - from solution to natural and artificial systems. *Chemical Reviews*, 104(4):2021–2071, 2004.

[12] P. Muller, X. P. Li, and K. K. Niyogi. Non-photochemical quenching. a response to excess light energy. *Plant Physiology*, 125(4):1558–1566, 2001.

[13] K. K. Niyogi and T. B. Truong. Evolution of flexible non-photochemical quenching mechanisms that regulate light harvesting in oxygenic photosynthesis. *Current Opinion in Plant Biology*, 16(3):307–314, 2013.

[14] D. Kirilovsky. The photoactive orange carotenoid protein and photoprotection in cyanobacteria. *Recent Advances in Phototrophic Prokaryotes*, 675:139–159, 2010.

[15] A. Wilson, J. N. Kinney, P. H. Zwart, C. Punginelli, S. D'Haene, F. Perreau, M. G. Klein, D. Kirilovsky, and C. A. Kerfeld. Structural determinants underlying photoprotection in the photoactive orange carotenoid protein of cyanobacteria. *Journal of Biological Chemistry*, 285(24):18364–18375, 2010.

[16] H. Cong, D. M. Niedzwiedzki, G. N. Gibson, A. M. LaFountain, R. M. Kelsh, A. T. Gardiner, R. J. Cogdell, and H. A. Frank. Ultrafast time-resolved carotenoid to-bacteriochlorophyll energy transfer in lh2 complexes from photosynthetic bacteria. *Journal of Physical Chemistry B*, 112(34):10689–10703, 2008.

[17] G. K. Pattanayak, C. Phong, and M. J. Rust. Rhythms in energy storage control the ability of the cyanobacterial circadian clock to reset. *Current Opinions In Biology*, 24(16):1934–1938, 2014.

[18] G. Bonente, B. D. Howes, S. Caffarri, G. Smulevich, and R. Bassi. Interactions between the photosystem ii subunit psbs and xanthophylls studied *in vivo* and *in vitro*. *Journal of Biological Chemistry*, 283(13):8434–8445, 2008.

[19] S. Kereiche, A. Z. Kiss, R. Kouril, E. J. Boekema, and P. Horton. The psbs protein controls the macro-organisation of photosystem ii complexes in the grana membranes of higher plant chloroplasts. *FEBS letters*, 584(4):759–764, 2010.

CHAPTER 9

CONCLUSION

For decades researchers have explored the structure and dynamics of photosynthetic systems. These studies have revealed incredible machinery that is tightly regulated and optimized for safely harvesting solar energy. In many ways the field has a clear picture of the photosynthetic machinery. Structural biology has provided structures for many of the key PPCs and ultrafast spectroscopies have been able to discern energy transfer dynamics within these complexes. But all this information represents a snapshot of the light harvesting machinery. Biology is much more complex than that. Biology is alive and organisms are constantly changing and optimizing themselves for the external conditions. What the field of photosynthetic lacks is not a picture of the light harvesting, but rather a movie of the light harvesting. Until the development of GRAPES, fluorescence spectroscopy has been the only technique that can non-invasively measure energy transfer dynamics. Fluorescence spectroscopy has provided tremendous insight into the light harvesting process, but also has significant limitations. It is only directly sensitive to bright states that produce an emitted signal, and its temporal resolution is limited to the ps time scale.

The limitation of fluorescence to only be sensitive to bright states inherently hides much of photosynthesis from fluorescence spectroscopies. For instance, in low-light conditions, when there are not photoprotective mechanisms activated, the reaction center quenches $\approx$ 80-95 % of absorbed sunlight allowing at most only 5-20 % of the light to decay via fluorescence. Conversely, during high-light, NPQ quenches the majority of excitations and again fluorescence spectroscopy is observing only a small percentage of the absorbed light. The temporal resolution limitations associated with fluorescence spectroscopy also obscure many of the dynamical processes. Carotenoid-chlorophyll transfer, exciton relaxation, dynamics within a single antenna complex, quantum coherence, and conical intersections in carotenoids all occur on a sub picosecond timescale, most on a sub 100 fs timescale. Given these limitations, it is remarkable what fluorescence spectroscopy has provided the photosynthetic community.

This thesis demonstrates a new, non-invasive technique, to measure ultrafast energy transfer dynamics in photosynthesis. The improved GRAPES instrument has the ability to directly observe both bright and dark states, it can be performed *in vivo*, it has sub 100 fs temporal resolution, and it can observe changes in ultrafast dynamics that occur on the 1 second timescale. These capabilities have been proven through the first 2DES observation of energy transfer *in vivo* discussed in Chapter 4. From this experiment we learned how to remove the intense scatter associated with measurements made in living cells and found that intra-complex transfer times are not significantly changed by the lipid environment surrounding LH2 helping to justify decades of ultrafast work on isolated complexes. We then made the first observation of quantum coherences *in vivo* discussed in Chapter 5. These experiments demonstrated that the phenomena of long-lived superposition states, observed in isolated complexes, persists in intact cells. The biological relevance of these coherences is still a hotly debated topic in the field and this measurement was a necessary next step in either confirming or denying the relevance of quantum coherence in photosynthesis. Lastly we used the technique to perform a complete mapping of the dynamics and membrane architecture of the light harvesting machinery in *Rba. sphaeroides* discussed in Chapter 7. This measurement in conjunction with theoretical modeling represents a new method to probe membrane structure and organization and ultrafast dynamics in living systems.

These initial experiments have provided new insight into the design principles that have evolved over the billions of years photosynthesis on earth. We still have a lot to learn from nature on how to harvest solar energy and how to regulate and optimize the process for varying external conditions. The ability to capture energy transfer dynamics and electronic structure in near real time in living systems opens up tremendous new possibilities for science using the GRAPES instrument and brings the field closer to a complete "movie" of how nature evolved to harvest solar energy.